DLR-IB-RM-OP-2022-17

Modeling, Observing and Controlling a Cable-Suspended Aerial Manipulator as a Constrained System

Masterarbeit

Michael Rothammer

Deutsches Zentrum
für Luft- und Raumfahrt

DEPARTMENT OF INFORMATICS

TECHNISCHE UNIVERSITÄT MÜNCHEN

Master's Thesis in Robotics, Cognition, Intelligence

Modeling, Observing and Controlling a Cable-Suspended Aerial Manipulator As a Constrained System

Michael Rothammer

DEPARTMENT OF INFORMATICS

TECHNISCHE UNIVERSITÄT MÜNCHEN

Master's Thesis in Robotics, Cognition, Intelligence

Modeling, Observing and Controlling a Cable-Suspended Aerial Manipulator As a Constrained System

Modellierung, Zustandsbeobachtung und Regelung eines an Kabeln aufgehängten luftbasierten Manipulators als eines mit Zwangsbedingungen beaufschlagten Systems

Author:	Michael Rothammer
Supervisor:	Prof. Dr.-Ing. Alin Albu-Schäffer
Advisors:	Andre Fialho Coelho, M. Sc.
	Dr. Harsimran Singh
	Dr.-Ing. Thomas Hulin
Submission Date:	23.12.2021

I confirm that this master's thesis is my own work and I have documented all sources and material used.

Munich, 23.12.2021 Michael Rothammer

Abstract

The cable-suspended aerial manipulator is a robot consisting of a platform that is fully actuated with a system of 8 propellers, to which a 7-degrees of freedom manipulator is attached. It can be used for manipulation tasks at locations that are in great height or otherwise difficult to access from the ground.

The system can be modeled in different ways, four of which are sketched in this thesis, before their equivalence is demonstrated. In particular, modeling it as a collection of rigid bodies subject to Pfaffian constraints is further developed.

Different models of the cable-suspended aerial manipulator providing a variety in complexity and accuracy is presented. Subsequently, experimental data is used to validate two selected models and show their respective benefits and drawbacks. Furthermore, the data is used to identify some parameters defining the system's behavior.

The full state of the system can not be measured using proprioceptive sensors. Therefore, an observer is extended to be applicable to the system. It runs on exterioceptive sensors' pose and velocity measurements and provides estimate of the full absolute pose. In addition to the observer, a position controller is proposed.

The observer and the controller are extensively analyzed using simulations. Finally, the observers is applied to experimental data to show their applicability to the cable-suspended aerial manipulator.

Kurzfassung

Der behandelte, an einem Kabel aufgehängte Roboter besteht aus einer mittels eines Systems aus 8 Propellern voll aktuierten Plattform, an der ein Manipulator mit 7 Freiheitsgraden befestigt ist. Er eignet sich für Manipulationsaufgaben in großen Höhen oder an anderweitig schwer zugänglichen Orten.

Das System kann auf verschiedene Weisen modelliert werden, von denen vier in dieser Arbeit angesprochen werden, deren Equivalenz im Anschluss gezeigt wird. Insbesondere die Modellierung als eine Gruppe von Starrkörpern, die Zwangsbedingungen unterliegen, wird genauer untersucht.

Unterschiedliche Modelle des kabelaufgehängten Roboters, die in Komplexität, aber auch Genauigkeit variieren, werden dargestellt. Anschließend werden experimentelle Daten genutzt, um zwei ausgewählte Modelle zu validieren und deren Vor- und Nachteile zu zeigen. Weiterhin werden die Daten genutzt, um einige Parameter des Systems zu bestimmen.

Der gesamte Zustand des Systems kann nicht vollständig mithilfe propriozeptiver Sensorik ermittelt werden. Deshalb wird ein Zustandsbeobachter so angepasst, dass er auf das System angewandt werden kann. Er verwendet Lagen- und Geschwindigkeitsmessungen von exteriozeptiven Sensoren und schätzt die absolute Lage des Systems. Zusätzlich wird eine Positionsregelung vorgestellt, die in Kombination mit dem Beobachter anwendbar ist.

Der Beobachter und die Regelung werden auf Basis von Simulationen ausführlich analysiert. Schließlich wird der Beobachter auf experimentelle Daten angewandt, um zu zeigen, dass er für die Anwendung auf dem kabelaufgehängten Roboter geeignet ist.

Acknowledgments

I would like to express my great appreciation to Andre Fialho Coelho, Dr. Harsimran Singh and Dr.-Ing. Thomas Hulin for their invaluable support throughout the thesis.

Furthermore, I thank Dr.-Ing. Christian Ott and Hrishik Mishra for their great insights and recommendations that helped shape this thesis.

Finally, I would like to express my gratitude to Prof. Dr.-Ing. Alin Albu-Schffer for his supervision and the opportunity to pursue this thesis at the Institute of Robotics and Mechatronics at the German Aerospace Center.

Without all of you, I could not have achieved it. I enjoyed working with you a lot and I hope we can further collaborate in the future!

Contents

Chapter 1

Introduction

1.1 The cable-suspended aerial manipulator

Robotic manipulation is a fascinating field. It allows machines to physically and actively interact with their environment and thus alter reality itself. There are a variety of different use cases for robotic manipulation, a frequent one however are tasks in hard to reach areas.

Aerial manipulators are a typical example of robots addressing this use case. In recent years, different approaches to aerial manipulation have been taken. Unmanned Aerial Vehicles (UAV)s with attached manipulators as presented in [6, 17, 10, 7, 8] benefit from an extremely large workspace, as they can self-sufficiently position themselves. They are used for manipulation tasks of different kinds, including inspection of infrastructural installations such as power lines, which are generally difficult or dangerous to access. Some robots have even been equipped with two manipulators see([17, 10]), which additionally enables them to complete more advanced tasks, such as assembly operations or grasping of large objects.

Typically, low system weight is desired as it reduces the power required to just keep the robot in the air. In [8, 7] however, the manipulator itself already weighs around 15 kg, so the aircraft carrying it is even heavier, but also generally larger scaled.

A different approach to aerial manipulation is suspending robots from cables or ropes. An interesting example is presented in [19]. There, a gripper module with an internal propulsion system is suspended on a soft spring that acts as a partial gravity compensation in a given workspace. Thus, much less power is required to maintain a vertical position, while still a large workspace is preserved.

As another instance of a cable-suspended robot, in [14], the Cable-Suspended Aerial Manipulator (SAM) was presented. It consists of a base platform equipped on the bottom with a 7-degrees of freedom (DoF) manipulator. The manipulator is a KUKA LWR 4: it is comparatively lightweight and features torque sensors in every joint. On the top of the base platform, three cables are mounted on individual winches which can control their respective lengths. The cables' opposite ends are all mounted to one point, frequently the hook of a crane or similar. In addition to that, the SAM features an array of 8 propellers. This array is capable of generating an arbitrarily directed wrench on the SAM. The magnitude of the wrench, of course, is limited and so is the capability of realizing high-frequency wrenches because the propellers need to spin up first in order to produce any force.

The SAM is assumed to be mounted to a fixed suspension point. This means its equilibrium position is with its center of gravity (CoG) right underneath this suspension point. After sufficiently long time without any control input, the SAM would settle there.

Of course, multiple disturbance sources exist that will cause the SAM to move away from this equilibrium point. Examples of these disturbances include wind and movement of the suspension point.

In addition to external disturbance forces, actuation of the manipulator needs to be respected. Although the entire system's center of mass (CoM) would not shift horizontally as there's no external force in that direction, both the base platform's and the end effector's poses with respect to that CoM will change, and so will their respective absolute poses.

In [15], a controller to actively counteract oscillations caused by these disturbances is proposed, which dampens out movements of the platform. Similarily, in [5], an oscillation damping controller is included into a whole-body control framework. There, a compliance controller is applied on the manipulator end effector. However, this requires only six of the the SAM's at least 10 DoF (the number varies with the model used to describe the SAM, it is 10 assuming a spherical pendulum constraint on the platform). In the nullspace of the primary task, oscillation damping of the platform is included. Another example for hierarchical whole-body control on the SAM is given in [4], where it is applied to teleoperation in a way that allows the operator to select different tasks and their priorities for the framework to respect. In [11], teleoperation with the SAM is investigated as well. There, haptic and 3D visual feedback are provided in real-time to the operator, which enables advanced manipulation such as peg-in-hole insertion.

Of all the referenced previous work, none was aimed at increasing its workspace by moving further away from directly underneath the suspension point. Instead, the control approaches applied to the SAM have actively counteracted movements of its platform away from its natural equilibrium point.

However, this strategy considerably reduces the range of motion of the SAM along with its reachable workspace. The propulsion system, which has been used to control the SAM to stay at its natural equilibrium, could be used to shift that equilibrium to a set of points limited by the propellers' maximum thrust, the SAM's weight and the cable length. In order to unlock a greater workspace, potentially enabling the SAM to complete a wider variety of tasks, it would be desirable to have a controller stabilizing a desired equilibrium.

To realize this kind of controller, feedback in the form of the absolute system pose is required. However, it is hard to measure the absolute pose of the SAM by itself. This is a direct result of the suspension on cables, whose angles are not measured proprioceptively (as opposed to, e.g. the joint angles in the lightweight robot (LBR)). This means that the absolute pose needs to be measured exteroceptively, using sensors that observe the system's environment, such as an Inertial Measurement Unit (IMU), a GPS module, or a camera or a Light Detection and Ranging (LIDAR) system for visual odometry.

One of the major drawbacks of this kind of sensors is often a low measurement frequency, in most cases lower than the actuation frequency. In addition to that, sometimes faulty readings might occur, which need to be detected, render the value unusable and further increase the time between measurements. During this time, the dynamical system will most likely not be stationary, but move further along its trajectory.

It is desirable to design an observer that is capable of propagating the system state while no sensor readings are available. For this reason, an accurate model of the system dynamics is required to give a good estimation of the state's trajectory in between measurements.

1.2 Structure of this thesis

After a review of the mathematical background of the concepts used in this thesis, multiple methods to model physical systems in general will be presented, compared and their equivalence will be shown in general and for a specific example. Using one of the presented methods, which is based on Pfaffian constraints, five different models will be proposed to be used to model the SAM. These models differ in multiple ways. They are applicable to different physical setups, in particular regarding the existence of an intermediary mass, such as a hook. Apart from that, they also can be classified into rigid and compliant models. The models vary in complexity and accuracy. Next, two of these models will be experimentally validated. This is done by performing experiments on the real system and then optimizing simulations to accurately reproduce similar results. This way, the models will be compared and some of the system's parameters will be identified. Following that, an observer based on [13] will be designed. In addition to the referenced approach, it will take known wrenches acting on the system, as well as constraints, into account. In addition to that, a position controller will be proposed. Both the observer and the controller will subsequently be analyzed extensively using simulations. Finally, the observer will be applied to experimental data to validate it and show its applicability to the SAM.

1.3 Mathematical prerequisites

Most of this thesis' system equations will be expressed in the the Special Euclidian Group (3-dimensional) (SE(3)). The most important properties of this choice of representation along with some additional mathematical background will be described here.

Notation

We will generally denote positions as r with one bottom right index indicating the point whose position is being expressed. For instance, r_{A} is the position of A. v is a linear velocity, and ω is an angular velocity. In case there are two indices on the bottom right, it denotes a difference between two values. For example, $r_{\mathrm{AB}} = r_{\mathrm{B}} - r_{\mathrm{A}}$ is the vector pointing from A to B, and $v_{\mathrm{AB}} = v_{\mathrm{B}} - v_{\mathrm{A}}$ is the difference of the velocities of points A and B. Important examples of these indices include gt for *ground truth* values, obs for *observer* values, m for *measured* values (in particular IMU for IMU measurements and cam for camera measurements), and r for *reconstructed* values.

We will use multiple different coordinate frames. The bottom left index of any symbol will indicate which frame it is represented in, e.g. ${}_{\mathrm{I}}v$ will be represented in the I frame,

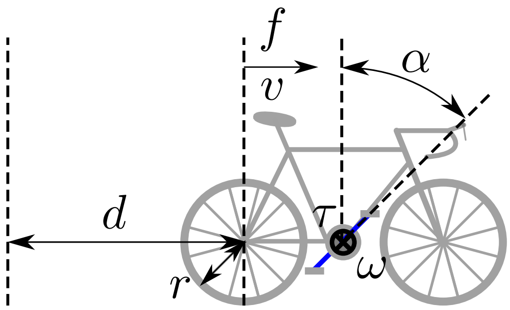

Figure 1.1: The different state descriptors and power ports of the bicycle

which generally denotes the inertial frame. For the I frame in particular, we may omit this index: $v \triangleq {}_{\mathrm{I}}v$.

I as an identity matrix and 0 as a zero vector or matrix are used without explicitly specifying their dimensions throughout this thesis, except when not unambiguously defined by the context.

In plots showing the orientation of a rigid body, r, p, and y will be used to refer to a roll-pitch-yaw representation.

1.3.1 Jacobians

Physical systems' states can be represented in many different ways, a few of which are described in § 2.

A very simple example would be a fixed-gear bicycle as depicted in Fig. 1.1 going along a straight line: one could describe its state by the angle its cranks have turned since starting at a known position (α), which would be a relevant measure when deciding which pedal to push to keep going. At the same time, one could describe the distance it has moved since starting (d), which would be more relevant when trying to decide if it should keep going in the first place.

It is clear that in essence, both these representations describe the same thing. This suggests that we can find a (possibly invertible) mapping from one measure (y) to another (x),

$$x = f(y). \tag{1.1}$$

In our example, $d = \frac{1}{n} r\alpha$, with the gearing ratio n and the wheel radius r. Now we might also like know how quickly the bicycle moves along the line when we know how quickly the pedals are spun. Again, it is intuitive that both are inherently related.

This motivates to find a mapping not only between the values themselves, but also their time derivatives. Knowing a mapping of the form (1.1), we can simply differentiate it to obtain

$$\dot{x} = \frac{\partial f(y)}{\partial y}\dot{y} = J(y)\dot{y}\partial, \tag{1.2}$$

where we introduced the *Jacobian* $J(y)$. Since (1.2) is very general, it demonstrates that there will always be a linear mapping between the time derivatives if a mapping like (1.1) exists.

In our example, we have $\dot{d} = \frac{1}{n} r\dot{\alpha}$. In this special case, $J = \frac{1}{n} r$ is constant.

Let's assume that the bike path leads uphill. This means that there is a constant force pushing the bike backwards. Now we would be interested to find the torque that needs to be applied to the cranks to counteract this force. This torque could be explicitly calculated based on the physical system. However, we already know a relationship between the velocity of the bicycle and the angular velocity of the cranks. Since we assume the bicycle to be well-maintained and slightly idealized, all the power put into the cranks will be translated to drive the bicycle.

In general, power, as a scalar, is invariant with respect to its representation, which implies

$$_{\mathrm{x}}P = {}_{\mathrm{y}}P = P. \tag{1.3}$$

In our example, the power put into the cranks is the product of their angular velocity and the applied torque, $\dot{\alpha}\tau$, whereas the power used to drive the bicycle is its velocity multiplied with the applied force: $\dot{d}f$. We can see that both powers are linear in the state variables' time derivatives.

It is very common that the time derivatives of the values describing a physical system's state represent so-called *flows* φ. If this is the case, it directly implies that the Jacobian maps between those flows like

$$\varphi_{\mathrm{x}} = \dot{x} = J(y)\dot{y} = J(y)\varphi_{\mathrm{y}}. \tag{1.4}$$

These flows could be for example a velocity, a current, or a volumetric flow. What defines them as flows is that there is a corresponding *effort* ε, such that for the pair of flow and effort,

$$\varepsilon^{\mathrm{T}}\varphi = P \tag{1.5}$$

holds.

Those efforts are typically forces, torques, voltages, or pressures. We call a related pair of flow and effort *power conjugated* variables. However, from the definition given here, it is not clear for a pair which value is the effort and which is the flow. As a result, a physical force could be a flow, if its conjugated effort is a velocity.

With (1.3), we can now find the Jacobian's applicability on efforts as

$$\varepsilon_{\mathrm{x}}^{\mathrm{T}}\varphi_{\mathrm{x}} = \varepsilon_{\mathrm{x}}^{\mathrm{T}}J(y)\varphi_{\mathrm{y}} = P = \varepsilon_{\mathrm{y}}^{\mathrm{T}}\varphi_{\mathrm{y}} \tag{1.6a}$$

$$\varepsilon_{\mathrm{y}} = J(y)^{\mathrm{T}}\varepsilon_{\mathrm{x}}. \tag{1.6b}$$

This shows that the transposed Jacobian can map efforts in the opposite direction to the Jacobian mapping between flows. In other words, if the Jacobian maps flows from representation y to representation x, then the transposed Jacobian maps efforts from representation x to representation y.

Coming back to the bicycle examples, we can now find that the required torque to counteract gravity is $\tau = J^{\mathrm{T}}f = \frac{1}{n}rf$.

An important remark is that often (1.1) is not invertible, and as a result, neither is the Jacobian matrix. This is generally a result of the choice of system state variables, which in turn is usually motivated by the physical system.

For example, the state of a robot with 6 rotational joints can be represented by the individual joint angles. There is also a unique mapping from these joint angles to the end effector position in 3-dimensional space. However, it is not possible to find a unique inverse mapping from the end effector position to the joint angles. In addition to that, the Jacobian mapping from joint angular velocities to end effector velocity is rectangular ($J \in \mathbb{R}^{6\times 3}$) and thus not invertible. In case of rectangular Jacobians, a weighted Moore-Penrose-Pseudoinverse for the Jacobian,

$$J^{\dagger,W,\mathrm{r}} = W^{-1}J^{\mathrm{T}}(JW^{-1}J^{\mathrm{T}})^{-1}, JJ^{\dagger,W,\mathrm{r}} = I \tag{1.7a}$$

$$J^{\dagger,W,\mathrm{l}} = (J^{\mathrm{T}}W^{-1}J)^{-1}J^{\mathrm{T}}W^{-1}, J^{\dagger,W,\mathrm{l}}J = I, \tag{1.7b}$$

can be helpful.

The right-sided pseudoinverse $J^{\dagger,W,\mathrm{r}}$ is only defined for $J \in \mathbb{R}^{m\times n}, m < n$ while the left-sided pseudoinverse $J^{\dagger,W,\mathrm{l}}$ is only defined for $J \in \mathbb{R}^{m\times n}, m > n$.

In particular for orientations, it is usually nontrivial to map between different representations. However, the respective Jacobians (mapping between angular velocities) are often much easier to find. In these cases, the Jacobians are not a result of the differentiation of a mapping, but rather found directly.

1.3.2 Rigid body pose and velocity representation

For a rigid body, the distance between any two points fixed on it never changes. Its pose can be fully described by the position (of the origin) and the orientation of a coordinate frame fixed to the body with respect to an inertial reference frame. The position is almost always represented as a 3-dimensional vector containing the displacement from a coordinate system's origin in its respective directions.

The orientation, however, can be described in a multitude of different ways, including, but not limited to, Euler angles such as roll-pitch-yaw or Kardan angles, quaternions, axis-angle pairs or rotation matrices.

Rigid body motion

Let P and Q denote two points on a rigid body. Their velocities are related by

$$v_{\mathrm{P}} = v_{\mathrm{Q}} + \omega \times r_{\mathrm{QP}}. \tag{1.8}$$

Here, v denote linear velocities, whereas ω is the angular velocity of the rigid body. r_{QP} is a vector pointing from Q to P, as illustrated in § 1.3.2.

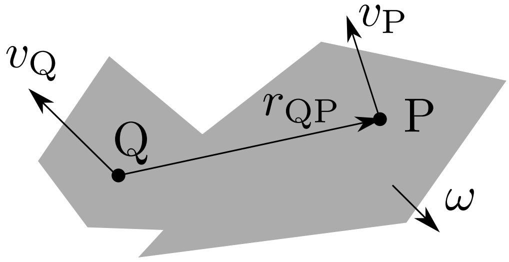

Figure 1.2: The velocities of two points on a rigid body

Rotations in the special orthogonal group

Using rotation matrices, we can map vector representations between differently oriented frames. For these matrices, their bottom left index can be interpreted as where they are mapping to, while their bottom right index shows where it's mapping from. For example, ${}_{\mathrm{A}}R_{\mathrm{B}}$ maps from frame B to frame A, so we can write

$$ {}_{\mathrm{A}}v = {}_{\mathrm{A}}R_{\mathrm{B}}{}_{\mathrm{B}}v. \tag{1.9} $$

Considering that rotations merely provide a different representation of the same vector, they preserve both the length l of vectors and the angles θ between any two vectors, that is

$$ l = \|{}_{\mathrm{A}}v\|_2 = \|{}_{\mathrm{B}}v\|_2 \tag{1.10a} $$

$$ \cos_\theta = \frac{{}_{\mathrm{A}}u^{\mathrm{T}}{}_{\mathrm{A}}v}{\|{}_{\mathrm{A}}u\|_2\|{}_{\mathrm{A}}v\|_2} = \frac{{}_{\mathrm{B}}u^{\mathrm{T}}{}_{\mathrm{B}}v}{\|{}_{\mathrm{B}}u\|_2\|{}_{\mathrm{B}}v\|_2}. \tag{1.10b} $$

Plugging (1.10a) into (1.10b), we obtain ${}_{\mathrm{B}}u^{\mathrm{T}}{}_{\mathrm{B}}v = {}_{\mathrm{A}}u^{\mathrm{T}}{}_{\mathrm{A}}v = {}_{\mathrm{B}}u^{\mathrm{T}}{}_{\mathrm{A}}R_{\mathrm{B}}^{\mathrm{T}}{}_{\mathrm{A}}R_{\mathrm{B}}{}_{\mathrm{B}}v$. Since this holds for any ${}_{\mathrm{B}}v$ and ${}_{\mathrm{B}}u$, we can conclude that ${}_{\mathrm{A}}R_{\mathrm{B}}^{\mathrm{T}}{}_{\mathrm{A}}R_{\mathrm{B}} = I$. This means that a rotation matrix's transpose equals its inverse,

$$ R^{\mathrm{T}}R = RR^{\mathrm{T}} = I. \tag{1.11} $$

This property is called *orthogonality.*

Naturally, any two rotations, applied one after another (called their *composition*), can be expressed as another rotation

$$ {}_{\mathrm{A}}R_{\mathrm{C}} = {}_{\mathrm{A}}R_{\mathrm{B}}\,{}_{\mathrm{B}}R_{\mathrm{C}} \tag{1.12} $$

(1.11) tells us that $(\det R)^2 = 1$, for all rotation matrices. This means that no rotation matrix can have a determinant other than -1 or 1. The axis-angle representation of rotations suggests that every rotation could be decomposed into a composition of two identical rotations around the same axis, but with only half the angle: $R = R^{\frac{1}{2}}R^{\frac{1}{2}}$. Looking at the resulting determinant, we obtain $\det R = (\det R^{\frac{1}{2}})^2 = 1$ for all rotation matrices.

A group G is a mathematical set endowed with a binary operation $\circ$ that satisfies four conditions:

- (Closedness) The operation maps any two elements of the group to another element of the group: $A, B \in G \implies A \circ B \in G$
- (Identity element) There is an identity element. If one of the operands is the identity element, then the result of the operation is the other operand: $\exists I \in G : A \in G \implies A \circ I = I \circ A = A$
- (Inverse element) Every element has an inverse element, such that the operation with both as operands returns the identity element: $\forall A \in G \exists A^{-1} \in G : A \circ A^{-1} = A^{-1} \circ A = I$
- (Associativity) The order in which multiple instances of the operation are executed does not change the result: $A, B, C \in G \implies A \circ (B \circ C) = (A \circ B) \circ C$

1.12 shows that rotations are closed under matrix multiplication. 1.11 shows the inverse of rotation matrices. The identity element I_3 satisfies the definition of a rotation matrix. Their matrix structure ensures associativity, and therefore, the rotation matrices form a group called the Special Orthogonal Group (3-dimensional) (SO(3)).

Taking the time derivative of 1.11, we obtain

$$R^{\mathrm{T}}\dot{R} = -\dot{R}^{\mathrm{T}}R = -(R^{\mathrm{T}}\dot{R})^{\mathrm{T}} = S. \tag{1.13}$$

Thus, we showed that rotation matrices generally satisfy $\dot{R} = RS$ with a skew-symetric $S^{\mathrm{T}} = -S$. This differential equation can be solved for constant S using the matrix exponential

$$R(t) = \exp(St). \tag{1.14}$$

Since the manifold of all rotation matrices, SO(3) is smooth and differentiable, we call it a *Lie group*. As a such, there exists a corresponding *Lie algebra*, in which S resides. It is denoted as $\mathfrak{so}(3)$. The *exponential map* mapping from $\mathfrak{so}(3)$ to SO(3) is the matrix exponential, whereas the *logarithmic map*, which maps from SO(3) to $\mathfrak{so}(3)$, turns out to be the matrix logarithm

$$S = \frac{\log(R(t))}{t}. \tag{1.15}$$

Absolute and local time derivatives

Looking at rotating bodies, it becomes quickly clear that we need to distinguish between local time derivatives and absolute ones. Assume a rigid body with a body frame B with a fixed origin, but rotating with a certain angular velocity ${}_{\mathrm{B}}\omega_{\mathrm{B}}$. Let ${}_{\mathrm{B}}x$ be a point fixed to this rigid body.

Observing its rate of change from the rigid body (*local time derivative*), we obtain

$$\frac{d}{dt}{}_{\mathrm{B}}x = 0. \tag{1.16}$$

This makes sense because the frame of observation rotates along with the rigid body, so it appears that the point doesn't move.

Observing its rate of change in the inertial system, we can find its *absolute* velocity v (*absolute time derivative*), which we can also express in the body frame as

$${}_{\mathrm{I}}v = \frac{d}{dt}{}_{\mathrm{I}}x = \frac{d}{dt}{}_{\mathrm{I}}R_{\mathrm{BB}}x = {}_{\mathrm{I}}R_{\mathrm{BI}}S_{\mathrm{BB}}x \tag{1.17a}$$

$${}_{\mathrm{B}}x_{\delta t} = {}_{\mathrm{B}}v = {}_{\mathrm{B}}R_{\mathrm{II}}v = {}_{\mathrm{I}}S_{\mathrm{BB}}x. \tag{1.17b}$$

This makes sense because from an absolute perspective, the point does move. In particular, its velocity can be computed from the rigid body kinematics, respecting that the body's origin (denoted O) does not move: $v_x = v_{\mathrm{O}} + \omega_{\mathrm{B}} \times r_{\mathrm{O}x} = \omega_{\mathrm{B}} \times x$. Expressing this in the body frame yields

$${}_{\mathrm{B}}v = {}_{\mathrm{B}}\omega_{\mathrm{B}} \times {}_{\mathrm{B}}x. \tag{1.18}$$

Equating (1.17b) and (1.18), we finally give meaning to S in

$$\begin{aligned} {}_{\mathrm{I}}S_{\mathrm{B}} &= ({}_{\mathrm{B}}\omega_{\mathrm{B}})_{\times} && (1.19\mathrm{a}) \\ {}_{\mathrm{I}}\dot{R}_{\mathrm{B}} &= {}_{\mathrm{I}}R_{\mathrm{B}}({}_{\mathrm{B}}\omega_{\mathrm{B}})_{\times}, && (1.19\mathrm{b}) \end{aligned}$$

where we used the expression of the cross product as a matrix-vector product ($u \times v = u_{\times}v, u_{\times} \in \mathbb{R}^{3\times 3}$). More expressions for the time derivative of rotation matrices along with a slightly different derivation can be found in [20].

Generalizing this idea, we can find the absolute derivative for any value as a function of its local derivative,

$${}_{\mathrm{B}}y_{\delta t} = {}_{\mathrm{B}}R_{\mathrm{I}}\frac{d}{dt}{}_{\mathrm{I}}y = {}_{\mathrm{B}}R_{\mathrm{I}}\frac{d}{dt}({}_{\mathrm{I}}R_{\mathrm{BB}}y) = {}_{\mathrm{B}}R_{\mathrm{I}}({}_{\mathrm{I}}R_{\mathrm{B}}\frac{d_{\mathrm{B}}y}{dt} + \frac{d_{\mathrm{I}}R_{\mathrm{B}}}{dt}{}_{\mathrm{B}}y) = \frac{d}{dt}{}_{\mathrm{B}}y + {}_{\mathrm{B}}\omega_{\mathrm{B}} \times {}_{\mathrm{B}}y. \quad (1.20)$$

For the angular velocity of the rigid body, the local time derivative is the same as the absolute one.

For rotation matrices not mapping to an inertial frame, we can find from (1.19b) that

$$\begin{aligned} {}_{\mathrm{A}}\dot{R}_{\mathrm{B}} &= {}_{\mathrm{A}}R_{\mathrm{II}}\dot{R}_{\mathrm{B}} + {}_{\mathrm{A}}\dot{R}_{\mathrm{II}}R_{\mathrm{B}} = {}_{\mathrm{A}}R_{\mathrm{B}}({}_{\mathrm{B}}\omega_{\mathrm{B}})_{\times} - ({}_{\mathrm{A}}\omega_{\mathrm{A}})_{\times}{}_{\mathrm{A}}R_{\mathrm{B}} = {}_{\mathrm{A}}R_{\mathrm{B}}({}_{\mathrm{B}}\omega_{\mathrm{B}} - {}_{\mathrm{A}}R^{\mathrm{T}}_{\mathrm{BA}}\omega_{\mathrm{A}})_{\times} \\ &= {}_{\mathrm{A}}R_{\mathrm{B}}({}_{\mathrm{B}}\omega_{\mathrm{AB}})_{\times}. \end{aligned} \quad (1.21)$$

Poses in the special Euclidian group

We will write the pose of a rigid body as a homogeneous matrix as

$$g_{\mathrm{B}} = \begin{bmatrix} R_{\mathrm{B}} & r_{\mathrm{B}} \\ 0 & 1 \end{bmatrix}. \quad (1.22)$$

Here, $R_{\mathrm{B}} \in \mathrm{SO}(3)$ is the rotation matrix rotating from the rigid body's frame to the inertial frame, and $r_{\mathrm{B}} \in \mathbb{R}^3$ is the coordinates of the rigid body's origin, expressed in the inertial frame.

More general, as shown in Fig. 1.3, we can use these homogeneous matrices to transform between poses,

$${}_{\mathrm{A}}g_{\mathrm{B}} = \begin{bmatrix} {}_{\mathrm{A}}R_{\mathrm{B}} & {}_{\mathrm{A}}r_{\mathrm{AB}} \\ 0 & 1 \end{bmatrix}, \quad (1.23)$$

where ${}_{\mathrm{A}}R_{\mathrm{B}}$ is the rotation matrix rotating from the rigid body's frame frame A, and ${}_{\mathrm{A}}r_{\mathrm{AB}}$ is the coordinates of the rigid body's origin, expressed in frame A. As a result, ${}_{\mathrm{A}}r_{\mathrm{AB}}$ points from frame A's origin to frame B's origin, not from the inertial frame's origin.

One of the benefits of this notation is that it is really easy to map the representation of a point or a vector in the rigid body's coordinate system into another body's frame. For

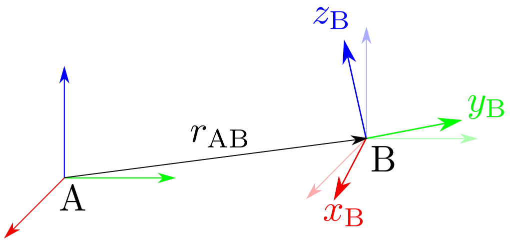

Figure 1.3: The components of a homogeneous transformation matrix: ${}_{\mathrm{A}}R_{\mathrm{B}} = \begin{bmatrix} {}_{\mathrm{A}}x_{\mathrm{B}} & {}_{\mathrm{A}}y_{\mathrm{B}} & {}_{\mathrm{A}}z_{\mathrm{B}} \end{bmatrix}$ is the rotation between both, and ${}_{\mathrm{A}}r_{\mathrm{AB}}$ is the respective translation.

that purpose, we concatenate a 1 for points and a 0 for vectors as a fourth coordinate to their 3-dimensional representation. Then, we achieve

$$\begin{bmatrix} {}_{\mathrm{A}}u \\ 0 \end{bmatrix} = \begin{bmatrix} {}_{\mathrm{A}}R_{\mathrm{B}}\,{}_{\mathrm{B}}u \\ 0 \end{bmatrix} = \begin{bmatrix} {}_{\mathrm{A}}R_{\mathrm{B}} & {}_{\mathrm{A}}r_{\mathrm{AB}} \\ 0 & 1 \end{bmatrix} \begin{bmatrix} {}_{\mathrm{B}}u \\ 0 \end{bmatrix} \tag{1.24a}$$

$$\begin{bmatrix} {}_{\mathrm{A}}x \\ 1 \end{bmatrix} = \begin{bmatrix} {}_{\mathrm{A}}R_{\mathrm{B}}\,{}_{\mathrm{B}}x + {}_{\mathrm{A}}r_{\mathrm{AB}} \\ 1 \end{bmatrix} = \begin{bmatrix} {}_{\mathrm{A}}R_{\mathrm{B}} & {}_{\mathrm{A}}r_{\mathrm{AB}} \\ 0 & 1 \end{bmatrix} \begin{bmatrix} {}_{\mathrm{B}}x \\ 1 \end{bmatrix}, \tag{1.24b}$$

where ${}_{\mathrm{Y}}u$ denotes a vector, whereas ${}_{\mathrm{Y}}x$ denotes a point, each represented in frame Y.

Similarly to rotation matrices, it intuitively makes sense that the application of multiple pose transformations one after another (again called a *composition* of pose transformations) can be represented by another, single pose transformation

$$\begin{aligned} {}_{\mathrm{A}}g_{\mathrm{B}}\,{}_{\mathrm{B}}g_{\mathrm{C}} &= \begin{bmatrix} {}_{\mathrm{A}}R_{\mathrm{B}} & {}_{\mathrm{A}}r_{\mathrm{AB}} \\ 0 & 1 \end{bmatrix} \begin{bmatrix} {}_{\mathrm{B}}R_{\mathrm{C}} & {}_{\mathrm{B}}r_{\mathrm{BC}} \\ 0 & 1 \end{bmatrix} = \begin{bmatrix} {}_{\mathrm{A}}R_{\mathrm{B}}\,{}_{\mathrm{B}}R_{\mathrm{C}} & {}_{\mathrm{A}}r_{\mathrm{AB}} + {}_{\mathrm{A}}R_{\mathrm{B}}\,{}_{\mathrm{B}}r_{\mathrm{BC}} \\ 0 & 1 \end{bmatrix} \\ &= \begin{bmatrix} {}_{\mathrm{A}}R_{\mathrm{C}} & {}_{\mathrm{A}}r_{\mathrm{AC}} \\ 0 & 1 \end{bmatrix} = {}_{\mathrm{A}}g_{\mathrm{C}}. \end{aligned} \tag{1.25}$$

Naturally, the pose transformation from any frame to itself is the identity matrix: There is no rotation (${}_{\mathrm{A}}R_{\mathrm{A}} = I$) and no translation (${}_{\mathrm{A}}r_{\mathrm{AA}} = 0$) between the two frames, implying ${}_{\mathrm{A}}g_{\mathrm{A}} = I$. If we combine this property with the composition as described in (1.25), we observe the following: ${}_{\mathrm{A}}g_{\mathrm{B}}\,{}_{\mathrm{B}}g_{\mathrm{A}} = {}_{\mathrm{A}}g_{\mathrm{A}} = I$, which defines the inverse of pose transformations: ${}_{\mathrm{A}}g_{\mathrm{B}}^{-1} = {}_{\mathrm{B}}g_{\mathrm{A}}$. This makes sense, as transforming from some frame A to another frame B and then transforming back from B to A should not change anything. We can also find a closed form solution for this inverse,

$${}_{\mathrm{A}}g_{\mathrm{B}}^{-1} = {}_{\mathrm{B}}g_{\mathrm{A}} = \begin{bmatrix} {}_{\mathrm{B}}R_{\mathrm{A}} & {}_{\mathrm{B}}r_{\mathrm{BA}} \\ 0 & 1 \end{bmatrix} = \begin{bmatrix} {}_{\mathrm{A}}R_{\mathrm{B}}^{\mathrm{T}} & -{}_{\mathrm{A}}R_{\mathrm{B}}^{\mathrm{T}}\,{}_{\mathrm{A}}r_{\mathrm{AB}} \\ 0 & 1 \end{bmatrix}. \tag{1.26}$$

From this, it can be easily shown that the homogeneous matrices constructed as in (1.23) form a group, which is called SE(3). It is closed under matrix multiplication ((1.25)), has an inverse element ((1.26)) and an identity element (§ 1.3.2), while associativity is provided by the matrix structure. Another property of SE(3) (which distinguishes it from the Euclidian Group (3-dimensional) (E(3))) is that these matrices all have a determinant of 1.

Taking the time derivative of (1.22), we obtain

$$\dot{g} = \begin{bmatrix} R_{\mathrm{B}}({}_{\mathrm{B}}\omega_{\mathrm{B}})_\times & R_{\mathrm{B}}{}_{\mathrm{B}}v_{\mathrm{B}} \\ 0 & 0 \end{bmatrix} = \begin{bmatrix} R_{\mathrm{B}} & r_{\mathrm{B}} \\ 0 & 1 \end{bmatrix} \begin{bmatrix} ({}_{\mathrm{B}}\omega_{\mathrm{B}})_\times & {}_{\mathrm{B}}v_{\mathrm{B}} \\ 0 & 0 \end{bmatrix} = g[{}_{\mathrm{B}}V_{\mathrm{B}}]^\wedge, \tag{1.27}$$

where ${}_{\mathrm{B}}V_{\mathrm{B}} = \begin{bmatrix} {}_{\mathrm{B}}\omega_{\mathrm{B}}^{\mathrm{T}} & {}_{\mathrm{B}}v_{\mathrm{B}}^{\mathrm{T}} \end{bmatrix}^{\mathrm{T}}$ denotes the *body twist* of frame B. This variable contains the *absolute* (i. e. relative to an inertial frame) angular and linear velocities of the frame B, expressed in the frame B. Apart from that, we introduced the *wedge operator*,

$$[{}_{\mathrm{B}}V_{\mathrm{B}}]^\wedge = \begin{bmatrix} ({}_{\mathrm{B}}\omega_{\mathrm{B}})_\times & {}_{\mathrm{B}}v_{\mathrm{B}} \\ 0 & 0 \end{bmatrix}. \tag{1.28}$$

Of course, there is a corresponding inverse operation, which we call the *vee operator*,

$$([{}_{\mathrm{B}}V_{\mathrm{B}}]^\wedge)^\vee = \begin{bmatrix} ({}_{\mathrm{B}}\omega_{\mathrm{B}})_\times & {}_{\mathrm{B}}v_{\mathrm{B}} \\ 0 & 0 \end{bmatrix}^\vee = {}_{\mathrm{B}}V_{\mathrm{B}}. \tag{1.29}$$

We have thus established that SE(3) is smooth and differentiable. This makes it another Lie group, and we denote its corresponding Lie algebra $\mathfrak{se}(3)$.

Analogously to SO(3), we find the solution to (1.27) for constant V using the matrix exponential, defining the *exponential map* from $\mathfrak{se}(3)$ to SE(3) as

$$g(t) = \exp(t[V]^\wedge). \tag{1.30}$$

The corresponding *logarithmic map* from SE(3) to $\mathfrak{se}(3)$ is again the matrix logarithm,

$$[V]^\wedge = \frac{\log(g(t))}{t}. \tag{1.31}$$

The logarithmic map can be used to find a representation of a pose in $\mathbb{R}^6$ as

$$\gamma = [\log(g)]^\vee. \tag{1.32}$$

According to [16, 2], if $\dot{g} = g[V]^\wedge$, this map's derivative can be computed as

$$\dot{\gamma} = \mathcal{B}(\gamma)V \tag{1.33a}$$

$$\mathcal{B}(\gamma) = \sum_{n=0}^{\inf} \frac{(-1)^n B_n}{n!} \mathrm{ad}_\gamma^n = I - \frac{1}{2}\mathrm{ad}_\gamma + f_1(\alpha)\mathrm{ad}_\gamma^2 + f_2(\alpha)\mathrm{ad}_\gamma^4, \tag{1.33b}$$

where $\gamma = \begin{bmatrix} \alpha^{\mathrm{T}} & \beta^{\mathrm{T}} \end{bmatrix}^{\mathrm{T}}$, $f_1(\alpha) = \frac{2}{\|\alpha\|_2^2} + \frac{\|\alpha\|_2 + 3\sin\|\alpha\|_2}{4\|\alpha\|_2(\cos\|\alpha\|_2 - 1)}$, and $f_2(\alpha) = \frac{1}{\|\alpha\|_2^4} + \frac{\|\alpha\|_2 + \sin\|\alpha\|_2}{4\|\alpha\|_2^3(\cos\|\alpha\|_2 - 1)}$.

1.3.3 Adjoints

As explained in § 1.3.2, we can map vectors and points between different frames using homogeneous matrices. In order to do the same to twists, we use the adjoint operation which we will refer to as the *transformation adjoint*. It takes the homogeneous matrix mapping between the frames as an argument, which we indicate as its bottom right index,

$$\mathrm{Ad}_g = \begin{bmatrix} R & 0 \\ r_\times R & R \end{bmatrix}. \tag{1.34}$$

It transforms twists like

$${}_{\mathrm{A}}V = \mathrm{Ad}_{{}_{\mathrm{A}}g_{\mathrm{B}}}{}_{\mathrm{B}}V = \begin{bmatrix} {}_{\mathrm{A}}R_{\mathrm{B}} & 0 \\ ({}_{\mathrm{A}}r_{\mathrm{AB}})_\times {}_{\mathrm{A}}R_{\mathrm{B}} & {}_{\mathrm{A}}R_{\mathrm{B}} \end{bmatrix} \begin{bmatrix} {}_{\mathrm{B}}\omega \\ {}_{\mathrm{B}}v \end{bmatrix} = \begin{bmatrix} {}_{\mathrm{A}}R_{\mathrm{B}}{}_{\mathrm{B}}\omega \\ {}_{\mathrm{A}}R_{\mathrm{B}}{}_{\mathrm{B}}v + ({}_{\mathrm{A}}R_{\mathrm{B}}{}_{\mathrm{B}}\omega) \times {}_{\mathrm{A}}r_{\mathrm{BA}} \end{bmatrix}. \tag{1.35}$$

This operation outputs the twist ${}_{\mathrm{A}}V$ in frame A as if A and B were rigidly connected and frame B moved with the twist ${}_{\mathrm{B}}V$.

The name "adjoint" is derived from its representation in $\mathfrak{se}(3)$ [3],

$$[{}_{\mathrm{A}}V]^\wedge = [\mathrm{Ad}_{{}_{\mathrm{A}}g_{\mathrm{B}}}{}_{\mathrm{B}}V]^\wedge = {}_{\mathrm{A}}g_{\mathrm{B}}[{}_{\mathrm{B}}V]^\wedge {}_{\mathrm{A}}g_{\mathrm{B}}^{-1}. \tag{1.36}$$

This leads to following useful property,

$$[V]^\wedge g = gg^{-1}[V]^\wedge g = g[\mathrm{Ad}_{g^{-1}}V]^\wedge. \tag{1.37}$$

Using power as a frame-invariant value, we can show how the adjoint operation can also map wrenches between different frames. Let the power computed in frame A be $P = {}_{\mathrm{A}}V^{\mathrm{T}}{}_{\mathrm{A}}f$. The power computed in frame B must be identical: $P = {}_{\mathrm{B}}V^{\mathrm{T}}{}_{\mathrm{B}}f$. We plug in (1.35) and obtain $P = {}_{\mathrm{B}}V^{\mathrm{T}}\mathrm{Ad}^{\mathrm{T}}_{{}_{\mathrm{A}}g_{\mathrm{B}}}{}_{\mathrm{A}}f = {}_{\mathrm{B}}V^{\mathrm{T}}{}_{\mathrm{B}}f$. Since we know this must hold for all ${}_{\mathrm{B}}V$, we can conclude

$${}_{\mathrm{B}}f = \mathrm{Ad}^{\mathrm{T}}_{{}_{\mathrm{A}}g_{\mathrm{B}}}{}_{\mathrm{A}}f = \begin{bmatrix} {}_{\mathrm{B}}R_{\mathrm{A}} & -{}_{\mathrm{B}}R_{\mathrm{A}}({}_{\mathrm{A}}r_{\mathrm{AB}})_\times \\ 0 & {}_{\mathrm{B}}R_{\mathrm{A}} \end{bmatrix} \begin{bmatrix} {}_{\mathrm{A}}\tau \\ {}_{\mathrm{A}}\varphi \end{bmatrix} = \begin{bmatrix} {}_{\mathrm{B}}R_{\mathrm{A}}{}_{\mathrm{A}}\tau + {}_{\mathrm{B}}R_{\mathrm{A}}({}_{\mathrm{A}}r_{\mathrm{BA}} \times {}_{\mathrm{A}}\varphi) \\ {}_{\mathrm{B}}R_{\mathrm{A}}{}_{\mathrm{A}}\varphi \end{bmatrix}. \tag{1.38}$$

This operation outputs the equivalent wrench ${}_{\mathrm{B}}f$ in frame B to if B and A were rigidly connected and at frame A, the wrench ${}_{\mathrm{A}}f$ was applied.

We can show that the composition of two transformation adjoints is not only a transformation adjoint itself, but in particular the transformation adjoint of the composition of the individual homogeneous transformations,

$$\begin{aligned}
\mathrm{Ad}_{{}_{\mathrm{A}}g_{\mathrm{B}}}\mathrm{Ad}_{{}_{\mathrm{B}}g_{\mathrm{C}}} &= \begin{bmatrix} {}_{\mathrm{A}}R_{\mathrm{B}} & 0 \\ ({}_{\mathrm{A}}r_{\mathrm{AB}})_{\times}{}_{\mathrm{A}}R_{\mathrm{B}} & {}_{\mathrm{A}}R_{\mathrm{B}} \end{bmatrix} \begin{bmatrix} {}_{\mathrm{B}}R_{\mathrm{C}} & 0 \\ ({}_{\mathrm{B}}r_{\mathrm{BC}})_{\times}{}_{\mathrm{B}}R_{\mathrm{C}} & {}_{\mathrm{B}}R_{\mathrm{C}} \end{bmatrix} \\
&= \begin{bmatrix} {}_{\mathrm{A}}R_{\mathrm{BB}}R_{\mathrm{C}} & 0 \\ ({}_{\mathrm{A}}r_{\mathrm{AB}})_{\times}{}_{\mathrm{A}}R_{\mathrm{BB}}R_{\mathrm{C}} + {}_{\mathrm{A}}R_{\mathrm{B}}({}_{\mathrm{B}}r_{\mathrm{BC}})_{\times}{}_{\mathrm{B}}R_{\mathrm{C}} & {}_{\mathrm{A}}R_{\mathrm{BB}}R_{\mathrm{C}} \end{bmatrix} \\
&= \begin{bmatrix} {}_{\mathrm{A}}R_{\mathrm{C}} & 0 \\ ({}_{\mathrm{A}}r_{\mathrm{AB}})_{\times}{}_{\mathrm{A}}R_{\mathrm{BB}}R_{\mathrm{C}} + ({}_{\mathrm{A}}R_{\mathrm{BB}}r_{\mathrm{BC}})_{\times}{}_{\mathrm{A}}R_{\mathrm{BB}}R_{\mathrm{C}} & {}_{\mathrm{A}}R_{\mathrm{C}} \end{bmatrix} \\
&= \begin{bmatrix} {}_{\mathrm{A}}R_{\mathrm{C}} & 0 \\ ({}_{\mathrm{A}}r_{\mathrm{AB}} + {}_{\mathrm{A}}R_{\mathrm{BB}}r_{\mathrm{BC}})_{\times}{}_{\mathrm{A}}R_{\mathrm{C}} & {}_{\mathrm{A}}R_{\mathrm{C}} \end{bmatrix} = \begin{bmatrix} {}_{\mathrm{A}}R_{\mathrm{C}} & 0 \\ ({}_{\mathrm{A}}r_{\mathrm{AC}})_{\times}{}_{\mathrm{A}}R_{\mathrm{C}} & {}_{\mathrm{A}}R_{\mathrm{C}} \end{bmatrix} = \mathrm{Ad}_{{}_{\mathrm{A}}g_{\mathrm{C}}}.
\end{aligned} \tag{1.39}$$

In the bottom left block, we made use of (2).

(1.39) implies that there should also be a closed form solution to the inverse: $\mathrm{Ad}_{{}_{\mathrm{A}}g_{\mathrm{B}}}\mathrm{Ad}_{{}_{\mathrm{B}}g_{\mathrm{A}}} = \mathrm{Ad}_{{}_{\mathrm{A}}g_{\mathrm{A}}} = \mathrm{Ad}_I = I$ and $\mathrm{Ad}_{{}_{\mathrm{B}}g_{\mathrm{A}}}\mathrm{Ad}_{{}_{\mathrm{A}}g_{\mathrm{B}}} = \mathrm{Ad}_{{}_{\mathrm{B}}g_{\mathrm{B}}} = \mathrm{Ad}_I = I$ mean $\mathrm{Ad}^{-1}_{{}_{\mathrm{A}}g_{\mathrm{B}}} = \mathrm{Ad}_{{}_{\mathrm{B}}g_{\mathrm{A}}}$.

Thus, we showed that the transformation adjoints are closed under multiplication and have an inverse element. In addition to that, the identity matrix provides an identity element and since associativity is given due to the matrix structure, the transformation adjoints form a group.

Using (1.27) and again (2) for the bottom left block, we can compute the time derivative of the transformation adjoint to

$$\frac{d}{dt}\mathrm{Ad}_g = \begin{bmatrix} R\omega & 0 \\ (Rv)_{\times}R + r_{\times}R\omega & R\omega \end{bmatrix} = \begin{bmatrix} R & 0 \\ r_{\times}R & R \end{bmatrix} \begin{bmatrix} \omega_{\times} & 0 \\ v_{\times} & \omega_{\times} \end{bmatrix} = \mathrm{Ad}_g \mathrm{ad}_V. \tag{1.40}$$

This way, we introduced another type of adjoint that we will refer to as the *differential adjoint*. Of course, we can again solve the differential equation for constant V using the matrix exponential,

$$\mathrm{Ad}_g(t) = \exp(\mathrm{ad}_V t). \tag{1.41}$$

We have established that the group of transformation adjoints is differentiable. In addition, it is obtained by a smooth and differentiable mapping from SE(3) onto $\mathbb{R}^{6\times 6}$, which makes it a manifold. Overall, this shows that the group of transformation adjoints is another Lie group.

1.3.4 Rigid body dynamics represented with twists

(1.27) shows how the kinematics of a rigid body can be described using its twist and pose. Here, we derive an expression for the twist's time derivative to represent rigid body dynamics.

Momenta

The linear momentum of a rigid body is

$$p = mv_{\mathrm{CoM}}. \tag{1.42}$$

m is the mass of the body, and v_{CoM} is the absolute linear velocity of its CoM.

Analogously, its angular momentum at the center of mass is

$$L^{\mathrm{CoM}} = \Theta^{\mathrm{CoM}}\omega. \tag{1.43}$$

Θ^{CoM} is the mass moment of inertia at the CoM, and ω is the absolute angular velocity of the body. The upper left index indicates the point of reference.

Laws of motion

Newton's second law (or Euler's first law) for a rigid body in 3D space is

$$p_{\delta t} = \varphi. \tag{1.44}$$

Here, φ is the sum of all forces acting on the body. The equation holds for an *absolute derivative* (see § 1.3.2) of the momentum $p_{\delta t}$.

Euler's second law gives us an analogous expression for rotational dynamics,

$$L_{\delta t} = \tau. \tag{1.45}$$

τ denotes the sum of all torques acting at the reference point of the angular momentum, including resulting torques of eccentrically acting forces. We will generally choose the CoM as reference point, in which case we will omit the index. The equation only holds for an absolute derivative of the momentum $L_{\delta t}$.

Time derivatives of momenta

Since we discuss rigid bodies here, we assume their mass to be constant, which leads to a simple expression of the linear momentum's absolute time derivative in the body frame,

$${}_{\mathrm{B}}p_{\delta t} = m({}_{\mathrm{B}}\dot{v}_{\mathrm{B}} + ({}_{\mathrm{B}}\omega_{\mathrm{B}})_{\times}{}_{\mathrm{B}}v_{\mathrm{B}}). \tag{1.46}$$

Here, ${}_{\mathrm{B}}v_{\mathrm{B}} = {}_{\mathrm{B}}v_{\mathrm{CoM}}$ denotes the velocity of the CoM of the body, expressed in the frame B which is fixed to the body.

The mass moment of inertia of a rigid body is attached to its orientation. If the body rotates, the mass moment of inertia rotates with it. This means that locally, relative to the body frame, it appears constant: $\frac{d}{dt}{}_{\mathrm{B}}\Theta_{\mathrm{B}}^{\mathrm{CoM}} = 0$.

Differentiating in the inertial frame however, it becomes clear that the absolute time derivative of Θ^{CoM} is not zero. For an expression of its absolute time derivative, we use (1.20), finding

$$({}_{\mathrm{B}}\Theta_{\mathrm{B}}^{\mathrm{CoM}})_{\delta t} = {}_{\mathrm{B}}\omega_{\mathrm{B}} \times {}_{\mathrm{B}}\Theta_{\mathrm{B}}^{\mathrm{CoM}}. \tag{1.47}$$

Using (1.47), the absolute time derivative of the angular momentum in the body frame is

$$ {}_{\mathrm{B}}L_{\delta t} = {}_{\mathrm{B}}\Theta_{\mathrm{B}}^{\mathrm{CoM}}\,{}_{\mathrm{B}}\dot{\omega}_{\mathrm{B}} + {}_{\mathrm{B}}\omega_{\mathrm{B}} \times {}_{\mathrm{B}}\Theta^{\mathrm{CoM}}\,{}_{\mathrm{B}}\omega_{\mathrm{B}}. \tag{1.48} $$

Equations of motion

Plugging in 1.46 into 1.44 and 1.48 into 1.45, we obtain

$$ \begin{aligned} \begin{bmatrix} {}_{\mathrm{B}}L_{\delta t} \\ {}_{\mathrm{B}}p_{\delta t} \end{bmatrix} &= \begin{bmatrix} {}_{\mathrm{B}}\Theta_{\mathrm{B}}^{\mathrm{CoM}}\,{}_{\mathrm{B}}\dot{\omega}_{\mathrm{B}} + {}_{\mathrm{B}}\omega_{\mathrm{B}} \times {}_{\mathrm{B}}\Theta^{\mathrm{CoM}}\,{}_{\mathrm{B}}\omega_{\mathrm{B}} \\ m\,{}_{\mathrm{B}}\dot{v} + m({}_{\mathrm{B}}\omega_{\mathrm{B}})_{\times}\,{}_{\mathrm{B}}v \end{bmatrix} \\ &= \begin{bmatrix} {}_{\mathrm{B}}\Theta_{\mathrm{B}}^{\mathrm{CoM}} & 0 \\ 0 & mI \end{bmatrix} \begin{bmatrix} {}_{\mathrm{B}}\dot{\omega}_{\mathrm{B}} \\ {}_{\mathrm{B}}\dot{v}_{\mathrm{B}} \end{bmatrix} + \begin{bmatrix} ({}_{\mathrm{B}}\omega_{\mathrm{B}})_{\times} & ({}_{\mathrm{B}}v_{\mathrm{B}})_{\times} \\ 0 & ({}_{\mathrm{B}}\omega_{\mathrm{B}})_{\times} \end{bmatrix} \begin{bmatrix} {}_{\mathrm{B}}\Theta_{\mathrm{B}}^{\mathrm{CoM}} & 0 \\ 0 & mI \end{bmatrix} \begin{bmatrix} {}_{\mathrm{B}}\omega_{\mathrm{B}} \\ {}_{\mathrm{B}}v_{\mathrm{B}} \end{bmatrix} \\ &= {}_{\mathrm{B}}\Lambda_{\mathrm{B}}\,{}_{\mathrm{B}}\dot{V}_{\mathrm{B}} - \mathrm{ad}^{\mathrm{T}}_{{}_{\mathrm{B}}V_{\mathrm{B}}}\,{}_{\mathrm{B}}\Lambda_{\mathrm{B}}\,{}_{\mathrm{B}}V_{\mathrm{B}} = \begin{bmatrix} {}_{\mathrm{B}}\tau_{\mathrm{B}} \\ {}_{\mathrm{B}}\varphi_{\mathrm{B}} \end{bmatrix} = {}_{\mathrm{B}}f_{\mathrm{B}} \qquad , \end{aligned} \tag{1.49} $$

where we introduced ${}_{\mathrm{B}}\Lambda_{\mathrm{B}} = \mathrm{blkdiag}({}_{\mathrm{B}}\Theta_{\mathrm{B}}^{\mathrm{CoM}}, mI)$, and ${}_{\mathrm{B}}f_{\mathrm{B}} = \begin{bmatrix} {}_{\mathrm{B}}\tau_{\mathrm{B}}^{\mathrm{T}} & {}_{\mathrm{B}}\varphi_{\mathrm{B}}^{\mathrm{T}} \end{bmatrix}^{\mathrm{T}}$. In addition to that, we identified the transpose of a differential adjoint.

Any mass moment of inertia that corresponds to a physical body is positive definite, and thus invertible. Similarly, the mass is positive, and thus Λ is invertible, so we can solve for the (local) time derivative of the body twist,

$$ {}_{\mathrm{B}}\dot{V}_{\mathrm{B}} = \Lambda^{-1}(\mathrm{ad}^{\mathrm{T}}_{{}_{\mathrm{B}}V_{\mathrm{B}}}\,{}_{\mathrm{B}}\Lambda_{\mathrm{B}}\,{}_{\mathrm{B}}V_{\mathrm{B}} + {}_{\mathrm{B}}f_{\mathrm{B}}). \tag{1.50} $$

Multibody systems

Many physical systems consist of multiple bodies. It is trivial to write (1.50) multiple times in one equation,

$$ {}_{\mathrm{S}}\dot{V}_{\mathrm{S}} = {}_{\mathrm{S}}\Lambda_{\mathrm{S}}^{-1}(F({}_{\mathrm{S}}V_{\mathrm{S}})^{\mathrm{T}}\,{}_{\mathrm{S}}\Lambda_{\mathrm{S}}\,{}_{\mathrm{S}}V_{\mathrm{S}} + {}_{\mathrm{S}}f_{\mathrm{S}}). \tag{1.51} $$

Here, with index S, we denote the *system* variables, ${}_{\mathrm{S}}V_{\mathrm{S}} = \begin{bmatrix} {}_{\mathrm{B1}}V_{\mathrm{B1}}^{\mathrm{T}} & {}_{\mathrm{B2}}V_{\mathrm{B2}}^{\mathrm{T}} & \dots \end{bmatrix}^{\mathrm{T}}$, ${}_{\mathrm{S}}\Lambda_{\mathrm{S}} = \mathrm{blkdiag}({}_{\mathrm{B1}}\Lambda_{\mathrm{B1}}, {}_{\mathrm{B2}}\Lambda_{\mathrm{B2}}, \dots)$, $F({}_{\mathrm{S}}V_{\mathrm{S}}) = \mathrm{blkdiag}(\mathrm{ad}_{{}_{\mathrm{B1}}V_{\mathrm{B1}}}, \mathrm{ad}_{{}_{\mathrm{B2}}V_{\mathrm{B2}}}, \dots)$, and ${}_{\mathrm{S}}f_{\mathrm{S}} = \begin{bmatrix} {}_{\mathrm{B1}}f_{\mathrm{B1}}^{\mathrm{T}} & {}_{\mathrm{B2}}f_{\mathrm{B2}}^{\mathrm{T}} & \dots \end{bmatrix}^{\mathrm{T}}$.

Similarly, we can define $g_{\mathrm{S}} = \mathrm{blkdiag}(g_{\mathrm{B1}}, g_{\mathrm{B2}}, \dots)$. Its time derivative is then

$$ \dot{g}_{\mathrm{S}} = g_{\mathrm{S}}G({}_{\mathrm{S}}V_{\mathrm{S}}). \tag{1.52} $$

We used $G({}_{\mathrm{S}}V_{\mathrm{S}}) = \mathrm{blkdiag}([{}_{\mathrm{B1}}V_{\mathrm{B1}}]^{\wedge}, [{}_{\mathrm{B2}}V_{\mathrm{B2}}]^{\wedge}, \dots)$.

Chapter 2

Modeling of constrained systems

Many physical systems can be modeled as a system of multiple free-floating bodies that are coupled through holonomic constraints. For example, a 1-DoF robot with a rotational joint has the constraint that both bodies coincide in a point on the rotation axis and that their relative orientation can only change in the direction of this axis. Constraints inherently lead to a loss of degrees of freedom. For a system with n bodies and c independent constraints, we can compute the number of DoF,

$$|\,\mathrm{DoF}| = 6n - c. \tag{2.1}$$

In this chapter, different approaches to model constrained systems are presented and demonstrated on the example of a spherical pendulum. Note that the derivations are formulated for mechanical systems, but the concepts hold for a variety of different domains as well.

2.1 Generalized coordinates

Kinematic constraints of a system and the resulting loss of DoF can be respected already while modeling the system. This can be done by selecting *generalized coordinates* q, a set of variables that can uniquely and unambiguously identify the exact configuration of the entire system.

In order to model system dynamics, we would like to find a differential equation for the second time derivatives of the generalized coordinates in the general form

$$\ddot{q} = f(q, \dot{q}, u), \tag{2.2}$$

where u denotes the input variable for the system, e. g. motor torques for a robot.

2.1.1 Direct modeling

In many cases, it's the easiest approach to directly find the differential equations of a system by analyzing its structure or by comparing it to a similar system. For this approach, the *forward kinematics* of the individual bodies are found as a function of q,

$${}_{\mathrm{I}}x = f(q). \tag{2.3}$$

${}_{\mathrm{I}}x$ contains the absolute positions of the individual bodies, allowing to obtain their absolute velocities using differentiation,

$$ {}_{\mathrm{I}}v = \frac{\delta}{\delta q} f(q)\dot{q} = J_{\mathrm{T}}(q)\dot{q}, \tag{2.4}$$

where we introduced the *translational Jacobian.* It is used to map the time derivative of the generalized coordinates to translational velocities in the system. We compute them in the inertial frame, where the absolute time derivative and the local one are identical.

It is meaningful to also find the rotational forward kinematics, e. g. in terms of a rotation matrix for each body,

$$ {}_{\mathrm{I}}R_{\mathrm{B}} = f(q). \tag{2.5}$$

Using the time derivative as described in (1.19), we find

$$ ({}_{\mathrm{B}}\omega_{\mathrm{B}})_{\times} = {}_{\mathrm{I}}R_{\mathrm{B}}^{\mathrm{T}} {}_{\mathrm{I}}\dot{R}_{\mathrm{B}}. \tag{2.6}$$

Generally, the angular velocity can then also be expressed in the form

$$ {}_{\mathrm{B}}\omega = J_{\mathrm{R}}(q)\dot{q}, \tag{2.7}$$

where we used the *rotational Jacobian*, which maps the time derivative of the generalized coordinates to angular velocities in the system. We compute the angular velocity in the body frame, where the mass moment of inertia is locally constant.

It is reasonable to assume that the input of a mechanical system consists of forces (φ_{in}) and torques (τ_{in}) acting on the involved bodies. In addition to that, the system itself might involve forces (φ_{sys}) and torques (τ_{sys}), which could depend on the system state. Those can result from dissipative elements such as dampers or from energy storing elements such as springs: $\varphi_{\mathrm{sys}} = \varphi_{\mathrm{d}} + \varphi_{\mathrm{k}}$, $\tau_{\mathrm{sys}} = \tau_{\mathrm{d}} + \tau_{\mathrm{k}}$.

Once the Jacobians and thus expressions for the translational and the angular velocities of all bodies in the system are found, the momenta can be computed using their mass moments of inertia and masses according to (1.42) and (1.43). After taking their time derivatives, (1.44) and (1.45) can be used to finally obtain the dynamics in a form like (2.2) for every body,

$$ \begin{bmatrix} J_{\mathrm{R}}(q) \\ J_{\mathrm{T}}(q) \end{bmatrix} \ddot{q} = \begin{bmatrix} \Theta^{-1}(\tau_{\mathrm{in}} + \tau_{\mathrm{sys}} - (J_{\mathrm{R}}(q)\dot{q})_{\times}\Theta J_{\mathrm{R}}(q)\dot{q}) - \dot{J}_{\mathrm{R}}(q)\dot{q} \\ m^{-1}(\varphi_{\mathrm{in}} + \varphi_{\mathrm{sys}}) - \dot{J}_{\mathrm{T}}(q)\dot{q} \end{bmatrix}. \tag{2.8}$$

In particular for constrained systems, this system of equations is over-determined because we have $6n$ equations for only $6n - c$ DoF (see (2.1)).

2.1.2 Lagrange formalism

If it is difficult to directly identify the differential equations describing a dynamical system, but generalized coordinates can be obtained, the Lagrange's equations of the second kind provide a helpful procedure.

First, the kinetic energy of the system is expressed as a function of the generalized coordinates and their first time derivatives,

$$E_{\mathrm{kin}} = f(q, \dot{q}). \tag{2.9}$$

Particularly for mechanical systems, we have

$$E_{\mathrm{kin}} = \sum_i \frac{1}{2} m_i {}_{\mathrm{T}}v_i^{\mathrm{T}} {}_{\mathrm{T}}v_i + \frac{1}{2} {}_{\mathrm{B},i}\omega_i^{\mathrm{T}} {}_{\mathrm{B},i}\Theta_i^{\mathrm{CoM}} {}_{\mathrm{B},i}\omega_i, \tag{2.10}$$

where m is the mass of the body, and Θ^{CoM} is the mass moment of inertia with its CoM as a reference point. Note that the linear part is calculated in the inertial frame, whereas the rotational part is calculated in the body frame, where the mass moment is locally constant.

Similarly, the potential energy is expressed as a function of the generalized coordinates,

$$E_{\mathrm{pot}} = f(q). \tag{2.11}$$

Finally, non-conservative inputs, including those produced by system components (such as forces from a damper), are identified. They might act in directions different to the generalized coordinates. As shown in (1.6), we can use the transposed Jacobians to transform forces and torques,

$$\begin{aligned} P_{\mathrm{R}} = \dot{q}^{\mathrm{T}} u_\tau = {}_{\mathrm{B}}\omega^{\mathrm{T}} {}_{\mathrm{B}}\tau = \dot{q}^{\mathrm{T}} J_{\mathrm{R}}^{\mathrm{T}}(q) {}_{\mathrm{B}}\tau \qquad & (2.12\mathrm{a}) \\ u_\tau = J_{\mathrm{R}}^{\mathrm{T}}(q) {}_{\mathrm{B}}\tau, \qquad & (2.12\mathrm{b}) \end{aligned}$$

and

$$\begin{aligned} P_{\mathrm{T}} = \dot{q}^{\mathrm{T}} u_\varphi = {}_{\mathrm{I}}v^{\mathrm{T}} {}_{\mathrm{I}}\varphi = \dot{q}^{\mathrm{T}} J_{\mathrm{T}}^{\mathrm{T}}(q) {}_{\mathrm{I}}\varphi \qquad & (2.13\mathrm{a}) \\ u_\varphi = J_{\mathrm{T}}^{\mathrm{T}}(q) {}_{\mathrm{I}}\varphi. \qquad & (2.13\mathrm{b}) \end{aligned}$$

Then, the nonconservative inputs, in particular for mechanical systems, are

$$Q = f(q, \dot{q}, u) = \sum_i J_{\mathrm{T},i}^{\mathrm{T}}(q) Q_{\mathrm{T},i}(u, q, \dot{q}) + J_{\mathrm{R},i}^{\mathrm{T}}(q) Q_{\mathrm{R},i}(u, q, \dot{q}). \tag{2.14}$$

Once these three functions are obtained, they are related using

$$\left(\frac{\delta}{\delta \dot{q}} E_{\mathrm{kin}}\right)_{\delta t} - \frac{\delta}{\delta q} E_{\mathrm{kin}} + \frac{\delta}{\delta q} E_{\mathrm{pot}} = Q. \tag{2.15}$$

(2.15) directly provides a differential equation of the dynamical system. Differently to (2.8), we obtain exactly $6n - c$ equations, which is a minimal representation of the system.

For mechanical systems, we obtain

$$
\begin{aligned}
&(\sum_i m_i J_{\mathrm{T},i\mathrm{T}}^{\mathrm{T}} J_{\mathrm{T},i}\dot{q} + J_{\mathrm{R},i\mathrm{B},i}^{\mathrm{T}} \Theta_i^{\mathrm{CoM}} J_{\mathrm{R},i}\dot{q})_{\delta t} \\
&-(\sum_i m_i \dot{J}_{\mathrm{T},i\mathrm{T}}^{\mathrm{T}} J_{\mathrm{T},i}\dot{q} + \dot{J}_{\mathrm{R},i\mathrm{B},i}^{\mathrm{T}} \Theta_i^{\mathrm{CoM}} J_{\mathrm{R},i}\dot{q}) + \frac{\delta}{\delta q} E_{\mathrm{pot}} \\
&= (\sum_i m_i (J_{\mathrm{T},i\mathrm{T}}^{\mathrm{T}} J_{\mathrm{T},i}\ddot{q} + \dot{J}_{\mathrm{T},i\mathrm{T}}^{\mathrm{T}} J_{\mathrm{T},i}\dot{q} + J_{\mathrm{T},i\mathrm{T}}^{\mathrm{T}} \dot{J}_{\mathrm{T},i}\dot{q}) - (\sum_i m_i \dot{J}_{\mathrm{T},i\mathrm{T}}^{\mathrm{T}} J_{\mathrm{T},i}\dot{q} + \dot{J}_{\mathrm{R},i\mathrm{B},i}^{\mathrm{T}} \Theta_i^{\mathrm{CoM}} J_{\mathrm{R},i}\dot{q}) \\
&+(J_{\mathrm{R},i\mathrm{B},i}^{\mathrm{T}} \Theta_i^{\mathrm{CoM}} J_{\mathrm{R},i}\ddot{q} + \dot{J}_{\mathrm{R},i\mathrm{B},i}^{\mathrm{T}} \Theta_i^{\mathrm{CoM}} J_{\mathrm{R},i}\dot{q} \\
&+J_{\mathrm{R},i\mathrm{B},i}^{\mathrm{T}} \Theta_i^{\mathrm{CoM}} \dot{J}_{\mathrm{R},i}\dot{q} + J_{\mathrm{R},i\mathrm{B},i}^{\mathrm{T}} (J_{\mathrm{R},i}\dot{q})_{\times} \Theta_i^{\mathrm{CoM}} J_{\mathrm{R},i}\dot{q})) + \frac{\delta}{\delta q} E_{\mathrm{pot}} \\
&= (\sum_i m_i (J_{\mathrm{T},i\mathrm{T}}^{\mathrm{T}} J_{\mathrm{T},i}\ddot{q} + J_{\mathrm{T},i\mathrm{T}}^{\mathrm{T}} \dot{J}_{\mathrm{T},i}\dot{q}) \\
&+(J_{\mathrm{R},i\mathrm{B},i}^{\mathrm{T}} \Theta_i^{\mathrm{CoM}} J_{\mathrm{R},i}\ddot{q} + J_{\mathrm{R},i\mathrm{B},i}^{\mathrm{T}} \Theta_i^{\mathrm{CoM}} \dot{J}_{\mathrm{R},i}\dot{q} + J_{\mathrm{R},i\mathrm{B},i}^{\mathrm{T}} (J_{\mathrm{R},i}\dot{q})_{\times} \Theta_i^{\mathrm{CoM}} J_{\mathrm{R},i}\dot{q})) + \frac{\delta}{\delta q} E_{\mathrm{pot}} \\
&= \sum_i ((m_i J_{\mathrm{T},i\mathrm{T}}^{\mathrm{T}} J_{\mathrm{T},i} + J_{\mathrm{R},i\mathrm{B},i}^{\mathrm{T}} \Theta_i^{\mathrm{CoM}} J_{\mathrm{R},i})\ddot{q} + m_i J_{\mathrm{T},i\mathrm{T}}^{\mathrm{T}} \dot{J}_{\mathrm{T},i}\dot{q} \\
&+J_{\mathrm{R},i\mathrm{B},i}^{\mathrm{T}} \Theta_i^{\mathrm{CoM}} \dot{J}_{\mathrm{R},i}\dot{q} + J_{\mathrm{R},i\mathrm{B},i}^{\mathrm{T}} (J_{\mathrm{R},i}\dot{q})_{\times} \Theta_i^{\mathrm{CoM}} J_{\mathrm{R},i}\dot{q}) + \frac{\delta}{\delta q} E_{\mathrm{pot}} = Q \qquad .
\end{aligned}
\tag{2.16}
$$

2.2 Constrained bodies

One way to express constraints is using a scalar function of the form

$$f(x) = 0. \tag{2.17}$$

Here, x is a vector of state variables. Taking the time derivative of (2.17), we find the formulation

$$\frac{\delta f}{\delta x}\dot{x} = 0. \tag{2.18}$$

We will denote $\frac{\delta f}{\delta x} = A(x)$ as the *Pfaffian constraint* matrix.

For the case of a single rigid body, we can rewrite (2.18) in terms of the body pose and the body twist,

$$A_{\mathrm{B}}(g_{\mathrm{B}})_{\mathrm{B}}V_{\mathrm{B}} = 0. \tag{2.19}$$

For a system of rigid bodies (see § 1.3.4), it can be formulated as

$$A_{\mathrm{S}}(g_{\mathrm{S}})_{\mathrm{S}}V_{\mathrm{S}} = 0. \tag{2.20}$$

$A_{\mathrm{S}}(g_{\mathrm{S}})$ can contain entries that couple multiple bodies.

For the sake of legibility, we omit in the following the argument of the constraint matrix: $A = A_{\mathrm{S}}(g_{\mathrm{S}})$ as well as any indices S.

2.2.1 Explicit constraint wrenches

It is possible to ensure the constraints are satisfied by explicitly modeling constraint wrenches f_{c}. Generally, those constraint wrenches must act solely along the directions of the constraints,

$$ {}_{\mathrm{S}}f_{\mathrm{c}} = A_{\mathrm{S}}(g_{\mathrm{S}})^{\mathrm{T}}\lambda_{\mathrm{c}}. \tag{2.21} $$

This can be motivated by the fact that constraint wrenches are *passive*, which means they never produce any power, i.e.

$$ {}_{\mathrm{S}}f_{\mathrm{c}}^{\mathrm{T}}\,{}_{\mathrm{S}}V_{\mathrm{S}} = \lambda_{\mathrm{c}}^{\mathrm{T}}A_{\mathrm{S}}(g_{\mathrm{S}})\,{}_{\mathrm{S}}V_{\mathrm{S}} = 0. \tag{2.22} $$

If we assume a system of rigid bodies to satisfy an arbitrary Pfaffian constraint, we want it to satisfy both (2.20) and (1.51). We assume the initial conditions to satisfy (2.20) and take its time derivative to obtain

$$ \dot{A}V + A\dot{V} = 0. \tag{2.23} $$

Plugging in (1.51) with $f = f_{\mathrm{in}} + A^{\mathrm{T}}\lambda_{\mathrm{c}}$ yields

$$ \dot{A}V + A\Lambda^{-1}(F(V)^{\mathrm{T}}\Lambda V + f_{\mathrm{in}} + A^{\mathrm{T}}\lambda_{\mathrm{c}}) = 0. \tag{2.24} $$

Solving for λ_{c}, we get

$$ \lambda_{\mathrm{c}} = (A\Lambda^{-1}A^{\mathrm{T}})^{-1}(A\Lambda^{-1}(-F(V)^{\mathrm{T}}\Lambda V - f_{\mathrm{in}}) - \dot{A}V). \tag{2.25} $$

Using this result, we can write the dynamics as

$$ \dot{V} = (I - \Lambda^{-1}A^{\mathrm{T}}(A\Lambda^{-1}A^{\mathrm{T}})^{-1}A)\Lambda^{-1}(F(V)^{\mathrm{T}}\Lambda V + f_{\mathrm{in}}) - \Lambda^{-1}A^{\mathrm{T}}(A\Lambda^{-1}A^{\mathrm{T}})^{-1}\dot{A}V. \tag{2.26} $$

$P = I - \Lambda^{-1}A^{\mathrm{T}}(A\Lambda^{-1}A^{\mathrm{T}})^{-1}A$ is a projection matrix ($PP = P$), which projects the dynamics into the directions that satisfy the constraints (i.e. are orthogonal to the constraints): $AP = (A - A) = 0$. In fact, the only term causing accelerations parallel to the constraints is $\dot{A}V$, which is dependent of the constraints' derivative itself.

If $AV = 0$, it appears useful to use $A\dot{V} = -\dot{A}V$ to eliminate $\dot{A}$ and obtain

$$ (I - \Lambda^{-1}A^{\mathrm{T}}(A\Lambda^{-1}A^{\mathrm{T}})^{-1}A)\dot{V} = (I - \Lambda^{-1}A^{\mathrm{T}}(A\Lambda^{-1}A^{\mathrm{T}})^{-1}A)\Lambda^{-1}(F(V)^{\mathrm{T}}\Lambda V + f_{\mathrm{in}}). \tag{2.27} $$

However, in order to obtain this equation, we already assumed $AV = 0$ instead of ensuring it, so any $\dot{V} = (F(V)^{\mathrm{T}}\Lambda V + f_{\mathrm{in}})$ solves it. This problem manifests in the projection matrix not being invertible, which indicates that this equation doesn't fully define $\dot{V}$.

2.2.2 Decomposition

As constraints inherently reduce the degrees of freedom of the system they're applied to, they allow us to represent the entire system in a reduced space.

For this, we find a decomposition of the system's velocities ${}_{\mathrm{S}}V_{\mathrm{S}}$ as

$$\nu = \begin{bmatrix} \nu_\perp \\ \nu_\parallel \end{bmatrix} = \begin{bmatrix} D_\perp^{\mathrm{T}} \\ D_\parallel^{\mathrm{T}} \end{bmatrix} V = D^{\mathrm{T}} V. \tag{2.28}$$

Here, $\nu_\perp$ contains the portion of the system velocity that is orthogonal to the constraints, i.e. satisfies the constraints, whereas $\nu_\parallel$ contains the portion parallel to (i.e. violating) the constraints. D is an orthogonal matrix that decomposes the system velocity into $\nu_\parallel$ and $\nu_\perp$.

As we require $\nu_\parallel = D_\parallel^{\mathrm{T}} V = 0$, it is reasonable to choose $D_\parallel$'s columns as linear combinations of the column vectors of A^{T},

$$D_\parallel = A^{\mathrm{T}} H_\parallel(A) \tag{2.29}$$

It is convenient to select a set of orthonormal vectors spanning the image of A^{T}, for example using the Gram-Schmidt algorithm, as this choice ensures $D_\parallel^{\mathrm{T}} D_\parallel = I$.

We can show that in order for D to be invertible, $D_\perp$ must be a linear combination of the column vectors of $I - A^{\mathrm{T}}(AA^{\mathrm{T}})^{-1}A$, as those are all orthogonal to $D_\parallel$,

$$D_\perp = (I - A^{\mathrm{T}}(AA^{\mathrm{T}})^{-1}A) H_\perp(A). \tag{2.30}$$

If we again select $H_\perp(A)$ to choose a set of orthonormal vectors spanning its image, D as a whole is orthogonal, which we assume from here.

$H_\perp(A) \in \mathbb{R}^{n\times(n-c)}$ is not square and as such not invertible.

After computing $D_\parallel$, it is already clear what the image of $D_\perp$ must be in order for D to be orthogonal. As a result, it is possible to simply complete an orthonormal basis of $\mathbb{R}^{6n}$ for n bodies and use these completing vectors as $D_\perp$'s columns.

To find the dynamics in the decomposed space, we differentiate (2.28) with respect to time and plug in (1.51) with $f = f_{\mathrm{in}} + A^{\mathrm{T}}\lambda_{\mathrm{c}}$ to obtain

$$\begin{bmatrix} \dot\nu_\perp \\ \dot\nu_\parallel \end{bmatrix} = \dot D^{\mathrm{T}} V + D^{\mathrm{T}} \dot V = \dot D^{\mathrm{T}} V + D^{\mathrm{T}} \Lambda^{-1}(F(V)^{\mathrm{T}} \Lambda V + f_{\mathrm{in}} + A^{\mathrm{T}}\lambda_{\mathrm{c}}). \tag{2.31}$$

In order for the constraint to be respected, we require $\dot\nu_\parallel = 0$. (2.31) gives us the explicit expression

$$\dot\nu_\parallel = \dot D_\parallel^{\mathrm{T}} V + D_\parallel^{\mathrm{T}} \Lambda^{-1}(F(V)^{\mathrm{T}} \Lambda V + f_{\mathrm{in}} + A^{\mathrm{T}}\lambda_{\mathrm{c}}) = 0. \tag{2.32}$$

We solve it for

$$\lambda_{\mathrm{c}} = (D_\parallel^{\mathrm{T}} \Lambda^{-1} A^{\mathrm{T}})^{-1}(D_\parallel^{\mathrm{T}} \Lambda^{-1}(-F(V)^{\mathrm{T}} \Lambda V - f_{\mathrm{in}}) - \dot D_\parallel^{\mathrm{T}} V). \tag{2.33}$$

We can then write the reduced dynamics in the orthogonal space, where

$$\dot{\nu}_\perp = \dot{D}_\perp^{\mathrm{T}} V + D_\perp^{\mathrm{T}} \Lambda^{-1} (F(V)^{\mathrm{T}} \Lambda V + f_{\mathrm{in}} + A^{\mathrm{T}} \lambda_{\mathrm{c}}). \tag{2.34}$$

Inverting (2.28) and respecting $\nu_{\|} = 0$, we obtain

$$V = D\nu = \begin{bmatrix} D_\perp & D_{\|} \end{bmatrix} \begin{bmatrix} \nu_\perp \\ \nu_{\|} \end{bmatrix} = D_\perp \nu_\perp. \tag{2.35}$$

2.3 Equivalence of all approaches

Since all the approaches aim to describe the same physical system, the resulting differential equations must be equivalent.

2.3.1 Equivalence of approaches based on generalized coordinates

In (2.16), we can plug in (2.8) to show it satisfies the same dynamics,

$$\begin{aligned}
&\sum_i (m_i J_{\mathrm{T},i}^{\mathrm{T}} (m^{-1} (\varphi_{\mathrm{in},i} + \varphi_{\mathrm{sys},i}) - \dot{J}_{\mathrm{T},i} \dot{q}) + m_i J_{\mathrm{T},i\mathrm{T}}^{\mathrm{T}} \dot{J}_{\mathrm{T},i} \dot{q} \\
&+ J_{\mathrm{R},i\mathrm{B},i}^{\mathrm{T}} \Theta_i^{\mathrm{CoM}} ((_{\mathrm{B},i} \Theta_i^{\mathrm{CoM}})^{-1} (\tau_{\mathrm{in},i} + \tau_{\mathrm{sys},i} - (J_{\mathrm{R},i} \dot{q})_{\times \mathrm{B},i} \Theta_i^{\mathrm{CoM}} J_{\mathrm{R},i} \dot{q}) - \dot{J}_{\mathrm{R},i} \dot{q}) \\
&+ J_{\mathrm{R},i\mathrm{B},i}^{\mathrm{T}} \Theta_i^{\mathrm{CoM}} \dot{J}_{\mathrm{R},i} \dot{q} + J_{\mathrm{R},i}^{\mathrm{T}} (J_{\mathrm{R},i} \dot{q})_{\times \mathrm{B},i} \Theta_i^{\mathrm{CoM}} J_{\mathrm{R},i} \dot{q}) + \frac{\delta}{\delta q} E_{\mathrm{pot}} \\
&= \sum_i (J_{\mathrm{T},i}^{\mathrm{T}} (\varphi_{\mathrm{in},i} + \varphi_{\mathrm{d},i} + \varphi_{\mathrm{k},i}) + J_{\mathrm{R},i}^{\mathrm{T}} (\tau_{\mathrm{in},i} + \tau_{\mathrm{d},i} + \tau_{\mathrm{k},i})) + \frac{\delta}{\delta q} E_{\mathrm{pot}} \\
&= \sum_i J_{\mathrm{T},i}^{\mathrm{T}} Q_{\mathrm{T},i}(u, q, \dot{q}) + J_{\mathrm{R},i}^{\mathrm{T}} Q_{\mathrm{R},i}(u, q, \dot{q}).
\end{aligned} \tag{2.36}$$

The equation holds if we use $\sum_i (J_{\mathrm{T},i}^{\mathrm{T}} \varphi_{\mathrm{k}} + J_{\mathrm{R},i}^{\mathrm{T}} \tau_{\mathrm{k}}) = -\frac{\delta}{\delta q} E_{\mathrm{pot}}$ and $\varphi_{\mathrm{in}} + \varphi_{\mathrm{d}} = Q_{\mathrm{T},i}(u, q, \dot{q})$, $\tau_{\mathrm{in}} + \tau_{\mathrm{d}} = Q_{\mathrm{R},i}(u, q, \dot{q})$, showing that the potential forces can be expressed as a gradient of a potential field and that the non-conservative forces result from dissipative elements and inputs.

2.3.2 Equivalence of approaches based on constrained rigid bodies

We chose $D_{\|}$'s columns as an orthonormal set of linear combinations of A^{T}, i. e. $D_{\|} = A^{\mathrm{T}} H(A)$, where $H(A)$ is a full rank mapping (else $D_{\|}$ couldn't have orthonormal columns). Plugging this into (2.33), we obtain

$$\begin{aligned}
\lambda_{\mathrm{c}} &= (H(A)^{\mathrm{T}} A \Lambda^{-1} A^{\mathrm{T}})^{-1} (H(A)^{\mathrm{T}} A \Lambda^{-1} (-F(V)^{\mathrm{T}} \Lambda V - f_{\mathrm{in}}) - H(A)^{\mathrm{T}} \dot{A} V - \dot{H}(A)^{\mathrm{T}} A V) \\
&= (A \Lambda^{-1} A^{\mathrm{T}})^{-1} H(A)^{-\mathrm{T}} H(A)^{\mathrm{T}} (A \Lambda^{-1} (-F(V)^{\mathrm{T}} \Lambda V - f_{\mathrm{in}}) - \dot{A} V) \\
&= (A \Lambda^{-1} A^{\mathrm{T}})^{-1} (A \Lambda^{-1} (-F(V)^{\mathrm{T}} \Lambda V - f_{\mathrm{in}}) - \dot{A} V).
\end{aligned} \tag{2.37}$$

It is clear that this derivation of λ leads to the exact same value as (2.25).

Taking (2.35)'s time derivative, we obtain an expression for the dynamics in full, non-reduced space,

$$\begin{aligned}
&\dot{V} = \dot{D}\nu + D\dot{\nu} = -D\dot{D}^{\mathrm{T}}D\nu + D_{\perp}\dot{D}_{\perp}^{\mathrm{T}}V + D_{\perp}D_{\perp}^{\mathrm{T}}\Lambda^{-1}(F(V)^{\mathrm{T}}\Lambda V + f_{\mathrm{in}} + A^{\mathrm{T}}\lambda_{\mathrm{c}})\\
&= -D_{\parallel}\dot{D}_{\parallel}^{\mathrm{T}}V - D_{\perp}\dot{D}_{\perp}^{\mathrm{T}}V + D_{\perp}\dot{D}_{\perp}^{\mathrm{T}}V + D_{\perp}D_{\perp}^{\mathrm{T}}\Lambda^{-1}(F(V)^{\mathrm{T}}\Lambda V + f_{\mathrm{in}} + A^{\mathrm{T}}\lambda_{\mathrm{c}})\\
&= -D_{\parallel}\dot{D}_{\parallel}^{\mathrm{T}}V + D_{\perp}D_{\perp}^{\mathrm{T}}\Lambda^{-1}(F(V)^{\mathrm{T}}\Lambda V + f_{\mathrm{in}} + A^{\mathrm{T}}\lambda_{\mathrm{c}})\\
&= \Lambda^{-1}(F(V)^{\mathrm{T}}\Lambda V + f_{\mathrm{in}} + A^{\mathrm{T}}\lambda_{\mathrm{c}}).
\end{aligned} \tag{2.38}$$

This is, as expected, exactly what we used in (2.31). In the last step, we used the identity

$$\begin{aligned}
&(I - D_{\perp}D_{\perp}^{\mathrm{T}})\Lambda^{-1}(F(V)^{\mathrm{T}}\Lambda V + f_{\mathrm{in}} + A^{\mathrm{T}}\lambda_{\mathrm{c}})\\
&= D\begin{bmatrix} D_{\perp}^{\mathrm{T}} \\ D_{\parallel}^{\mathrm{T}} \end{bmatrix}(I - D_{\perp}D_{\perp}^{\mathrm{T}})((I - \Lambda^{-1}A^{\mathrm{T}}(A\Lambda^{-1}A^{\mathrm{T}})^{-1}A)\Lambda^{-1}(F(V)^{\mathrm{T}}\Lambda V + f_{\mathrm{in}})\\
&-\Lambda^{-1}A^{\mathrm{T}}(A\Lambda^{-1}A^{\mathrm{T}})^{-1}\dot{A}V)\\
&= D\begin{bmatrix} D_{\perp}^{\mathrm{T}} \\ H(A)^{\mathrm{T}}A \end{bmatrix}(I - D_{\perp}D_{\perp}^{\mathrm{T}})((I - \Lambda^{-1}A^{\mathrm{T}}(A\Lambda^{-1}A^{\mathrm{T}})^{-1}A)\Lambda^{-1}(F(V)^{\mathrm{T}}\Lambda V + f_{\mathrm{in}})\\
&-\Lambda^{-1}A^{\mathrm{T}}(A\Lambda^{-1}A^{\mathrm{T}})^{-1}\dot{A}V)\\
&= D\begin{bmatrix} 0 \\ -H(A)^{\mathrm{T}}\dot{A}V \end{bmatrix} = -D_{\parallel}H(A)^{\mathrm{T}}\dot{A}V = -D_{\parallel}\dot{D}_{\parallel}V.
\end{aligned} \tag{2.39}$$

This shows that the dynamics can be losslessly represented in the reduced space and, if needed, be mapped into the system velocities or even the system accelerations.

2.3.3 Equivalence of approaches based on generalized coordinates and on constrained rigid bodies

Using generalized coordinates, we can write the body twists of every single body in the system using the Jacobians as

$${}_{\mathrm{B}}V_{\mathrm{B}} = \begin{bmatrix} {}_{\mathrm{B}}\omega_{\mathrm{B}} \\ {}_{\mathrm{B}}v_{\mathrm{B}} \end{bmatrix} = \begin{bmatrix} J_{\mathrm{R}}(q) \\ {}_{\mathrm{B}}R_{\mathrm{I}}J_{\mathrm{T}}(q) \end{bmatrix}\dot{q} = J_{\mathrm{V}}(q)\dot{q}. \tag{2.40}$$

We can also find the time derivative of the body twist in terms of q,

$$\begin{aligned}
&\frac{d}{dt}(J_{\mathrm{V}}\dot{q}) = {}_{\mathrm{B}}\dot{V}_{\mathrm{B}} = \begin{bmatrix} \dot{J}_{\mathrm{R}}\dot{q} + J_{\mathrm{R}}\ddot{q} \\ {}_{\mathrm{B}}\dot{R}_{\mathrm{I}}J_{\mathrm{T}}\dot{q} + {}_{\mathrm{B}}R_{\mathrm{I}}\dot{J}_{\mathrm{T}}\dot{q} + {}_{\mathrm{B}}R_{\mathrm{I}}J_{\mathrm{R}}\ddot{q} \end{bmatrix}\\
&= \begin{bmatrix} \dot{J}_{\mathrm{R}}\dot{q} + \Theta^{-1}(\tau_{\mathrm{in}} + \tau_{\mathrm{sys}} - (J_{\mathrm{R}}\dot{q})_{\times}\Theta J_{\mathrm{R}}\dot{q}) - \dot{J}_{\mathrm{R}}\dot{q} \\ -{}_{\mathrm{B}}R_{\mathrm{I}}({}_{\mathrm{I}}R_{\mathrm{B}}J_{\mathrm{R}}\dot{q})_{\times}J_{\mathrm{T}}\dot{q} + {}_{\mathrm{B}}R_{\mathrm{I}}\dot{J}_{\mathrm{T}}\dot{q} + {}_{\mathrm{B}}R_{\mathrm{I}}m^{-1}(\varphi_{\mathrm{in}} + \varphi_{\mathrm{sys}}) - {}_{\mathrm{B}}R_{\mathrm{I}}\dot{J}_{\mathrm{T}}\dot{q} \end{bmatrix}\\
&= \begin{bmatrix} \Theta^{-1}(\tau_{\mathrm{in}} + \tau_{\mathrm{sys}} - (J_{\mathrm{R}}\dot{q})_{\times}{}_{\mathrm{B}}R_{\mathrm{I}}\Theta J_{\mathrm{R}}\dot{q}) \\ -(J_{\mathrm{R}}\dot{q})_{\times}{}_{\mathrm{B}}R_{\mathrm{I}}J_{\mathrm{T}}\dot{q} + {}_{\mathrm{B}}R_{\mathrm{I}}m^{-1}(\varphi_{\mathrm{in}} + \varphi_{\mathrm{sys}}) \end{bmatrix}\\
&= \Lambda^{-1}(\mathrm{ad}_{J_{\mathrm{V}}^{\mathrm{T}}\dot{q}}\Lambda J_{\mathrm{V}}\dot{q} + {}_{\mathrm{B}}f_{\mathrm{u}} + {}_{\mathrm{B}}f_{\mathrm{sys}}).
\end{aligned} \tag{2.41}$$

For multi-body systems, we can obtain $J_{\mathrm{S}}(q) = \begin{bmatrix} J_{\mathrm{V1}}(q) & J_{\mathrm{V2}}(q) & \dots \end{bmatrix}$. The time derivative of the system twist is then

$$\frac{d}{dt}(J_{\mathrm{S}}\dot{q}) = {}_{\mathrm{S}}\Lambda_{\mathrm{S}}^{-1}(F^{\mathrm{T}}(J_{\mathrm{S}}\dot{q})_{\mathrm{S}}\Lambda_{\mathrm{S}}J_{\mathrm{S}}\dot{q} + f_{\mathrm{u}} + f_{\mathrm{sys}}). \tag{2.42}$$

Knowing that the system velocities satisfy $AJ_{\mathrm{S}}(q)\dot{q} = 0$ (as the generalized coordinates have been constructed respecting the constraints), we can derive $\dot{A}J_{\mathrm{S}}(q)\dot{q} + A\frac{d}{dt}(J_{\mathrm{S}}\dot{q}) = 0$. Using this, we take the time derivative of ${}_{\mathrm{S}}V_{\mathrm{S}}$ and obtain

$$\begin{aligned}
&\frac{d}{dt}{}_{\mathrm{S}}V_{\mathrm{S}} = \frac{d}{dt}(J_{\mathrm{S}}\dot{q}) \\
&= \frac{d}{dt}(J_{\mathrm{S}}\dot{q}) - \Lambda^{-1}A^{\mathrm{T}}(A\Lambda^{-1}A^{\mathrm{T}})^{-1}(\dot{A}J_{\mathrm{S}}\dot{q} + A\frac{d}{dt}(J_{\mathrm{S}}\dot{q})) \\
&= (I - \Lambda^{-1}A^{\mathrm{T}}(A\Lambda^{-1}A^{\mathrm{T}})^{-1}A)\frac{d}{dt}(J_{\mathrm{S}}\dot{q}) - \Lambda^{-1}A^{\mathrm{T}}(A\Lambda^{-1}A^{\mathrm{T}})^{-1}\dot{A}J_{\mathrm{S}}\dot{q} \\
&= (I - \Lambda^{-1}A^{\mathrm{T}}(A\Lambda^{-1}A^{\mathrm{T}})^{-1}A)\Lambda^{-1}(F^{\mathrm{T}}(J_{\mathrm{S}}\dot{q})\Lambda J_{\mathrm{S}}\dot{q} + f_{\mathrm{u}} + f_{\mathrm{sys}}) \\
&-\Lambda^{-1}A^{\mathrm{T}}(A\Lambda^{-1}A^{\mathrm{T}})^{-1}\dot{A}J_{\mathrm{S}}\dot{q} \\
&= (I - \Lambda^{-1}A^{\mathrm{T}}(A\Lambda^{-1}A^{\mathrm{T}})^{-1}A)\Lambda^{-1}(F^{\mathrm{T}}({}_{\mathrm{S}}V_{\mathrm{S}})\Lambda_{\mathrm{S}}V_{\mathrm{S}} + f_{\mathrm{u}} + f_{\mathrm{sys}}) \\
&-\Lambda^{-1}A^{\mathrm{T}}(A\Lambda^{-1}A^{\mathrm{T}})^{-1}\dot{A}_{\mathrm{S}}V_{\mathrm{S}}.
\end{aligned} \tag{2.43}$$

Thus, we showed that ${}_{\mathrm{S}}V_{\mathrm{S}} = J_{\mathrm{S}}(q)\dot{q}$ satisfies (2.26), with $f_{\mathrm{in}} = f_{\mathrm{u}} + f_{\mathrm{sys}}$.

Furthermore, In (2.35), we have an expression of the same form as (2.40): ${}_{\mathrm{S}}V_{\mathrm{S}} = D_{\perp}(g)\nu_{\perp}$. It is clear that the body poses solely depend on the generalized coordinates: $g = g(q)$, because generalized coordinates must be able to describe the entire system's configuration (see § 2.1). From that, we have $D_{\perp}(g) = D_{\perp}(q)$. Since we already know that both $D_{\perp}(q)$ and $J_{\mathrm{S}}(q)$ have the same image, we can conclude that there is an invertible mapping $P(q)$ which satisfies

$$J_{\mathrm{S}}(q) = D_{\perp}(q)P(q). \tag{2.44}$$

From that, we find an expression for $\nu_{\perp}$ in terms of the generalized coordinates' time derivatives,

$$J_{\mathrm{S}}\dot{q} = D_{\perp}P\dot{q} = D_{\perp}\nu_{\perp} \tag{2.45a}$$

$$\nu_{\perp} = P\dot{q} \tag{2.45b}$$

$$\dot{q} = P^{-1}\nu_{\perp} \tag{2.45c}$$

$$\dot{\nu}_{\perp} = \dot{D}_{\perp}^{\mathrm{T}}V + D_{\perp}^{\mathrm{T}}\dot{V} = \dot{P}\dot{q} + P\ddot{q}. \tag{2.45d}$$

Plugging (2.43) into (2.45d) and rearranging, we can find P in

$$\begin{aligned}
&\dot{\nu}_{\perp} = \dot{P}\dot{q} + P\ddot{q} = \dot{D}_{\perp}^{\mathrm{T}}V + D_{\perp}^{\mathrm{T}}\dot{V} \\
&= \dot{D}_{\perp}^{\mathrm{T}}J_{\mathrm{S}}\dot{q} + D_{\perp}^{\mathrm{T}}((I - \Lambda^{-1}A^{\mathrm{T}}(A\Lambda^{-1}A^{\mathrm{T}})^{-1}A)(\dot{J}_{\mathrm{S}}\dot{q} + J_{\mathrm{S}}\ddot{q}) - \Lambda^{-1}A^{\mathrm{T}}(A\Lambda^{-1}A^{\mathrm{T}})^{-1}\dot{A}J_{\mathrm{S}}\dot{q}) \\
&= D_{\perp}^{\mathrm{T}}(I - \Lambda^{-1}A^{\mathrm{T}}(A\Lambda^{-1}A^{\mathrm{T}})^{-1}A)J_{\mathrm{S}}\ddot{q} \\
&+(\dot{D}_{\perp}^{\mathrm{T}}J_{\mathrm{S}} + D_{\perp}^{\mathrm{T}}\dot{J}_{\mathrm{S}} - D_{\perp}^{\mathrm{T}}\Lambda^{-1}A^{\mathrm{T}}(A\Lambda^{-1}A^{\mathrm{T}})^{-1}A\dot{J}_{\mathrm{S}} - D_{\perp}^{\mathrm{T}}\Lambda^{-1}A^{\mathrm{T}}(A\Lambda^{-1}A^{\mathrm{T}})^{-1}\dot{A}J_{\mathrm{S}})\dot{q} \\
&= D_{\perp}^{\mathrm{T}}(I - \Lambda^{-1}A^{\mathrm{T}}(A\Lambda^{-1}A^{\mathrm{T}})^{-1}A)J_{\mathrm{S}}\ddot{q} \\
&+(\dot{D}_{\perp}^{\mathrm{T}}J_{\mathrm{S}} + D_{\perp}^{\mathrm{T}}\dot{J}_{\mathrm{S}} - D_{\perp}^{\mathrm{T}}\Lambda^{-1}A^{\mathrm{T}}(A\Lambda^{-1}A^{\mathrm{T}})^{-1}A\dot{J}_{\mathrm{S}} - D_{\perp}^{\mathrm{T}}\Lambda^{-1}A^{\mathrm{T}}(A\Lambda^{-1}A^{\mathrm{T}})^{-1}\dot{A}J_{\mathrm{S}} \\
&+\frac{d}{dt}(D_{\perp}^{\mathrm{T}}\Lambda^{-1}A^{\mathrm{T}}(A\Lambda^{-1}A^{\mathrm{T}})^{-1})AJ_{\mathrm{S}})\dot{q} \\
&= D_{\perp}^{\mathrm{T}}(I - \Lambda^{-1}A^{\mathrm{T}}(A\Lambda^{-1}A^{\mathrm{T}})^{-1}A)J_{\mathrm{S}}\ddot{q} + \frac{d}{dt}(D_{\perp}^{\mathrm{T}}(I - \Lambda^{-1}A^{\mathrm{T}}(A\Lambda^{-1}A^{\mathrm{T}})^{-1}A)J_{\mathrm{S}})\dot{q} \\
&= P\ddot{q} + \dot{P}\dot{q}.
\end{aligned} \tag{2.46}$$

However, although we found the explicit expression $P = D_{\perp}^{\mathrm{T}}(I - \Lambda^{-1}A^{\mathrm{T}}(A\Lambda^{-1}A^{\mathrm{T}})^{-1}A)J_{\mathrm{S}}$, it does not provide us with an explicit mapping between the Pfaffian constraint matrix and the system Jacobians as indicated in (2.44) because it depends on those values itself.

2.4 Modeling a spherical pendulum

As an example for the different approaches leading to the same result, we model a spherical pendulum as shown in Fig. 3.1a, using the proposed approaches. We assume an arbitrary wrench, expressed in the platform frame, ${}_{\mathrm{P}}f_{\mathrm{in}}^{\mathrm{P}} = \begin{bmatrix}{}_{\mathrm{P}}\tau_{\mathrm{in}}^{\mathrm{P}}\,{}_{\mathrm{P}}\varphi_{\mathrm{in}}^{\mathrm{P}}\end{bmatrix}^{\mathrm{T}}$, acting on the platform CoM as input.

We will denote the suspension point as S, and the platform CoM as P. The platform's mass is m_{P}, and its inertia with the CoM as reference point is $\Theta_{\mathrm{P}}^{\mathrm{CoM}}$.

2.4.1 Generalized coordinates

As generalized coordinates, we can choose three angles: α defining a rotation of the pendulum arm around the inertial frame's x-axis, β defining a rotation of the arm around the rotated y-axis, and finally γ defining a rotation around the twice rotated z-axis (the pendulum arm itself). Together, $q = \begin{bmatrix}\alpha & \beta & \gamma\end{bmatrix}^{\mathrm{T}}$ unambiguously, however not quite uniquely (There's a singularity at the unstable equilibrium point of the pendulum), define the full configuration of the pendulum.

With these angles we can define the pendulum orientation in the inertial frame to

$${}_{\mathrm{I}}R_{\mathrm{P}} = R_x(\alpha)R_y(\beta)R_z(\gamma) = \begin{bmatrix}1 & 0 & 0\\ 0 & \cos\alpha & -\sin\alpha\\ 0 & \sin\alpha & \cos\alpha\end{bmatrix}\begin{bmatrix}\cos\beta & 0 & \sin\beta\\ 0 & 1 & 0\\ -\sin\beta & 0 & \cos\beta\end{bmatrix}\begin{bmatrix}\cos\gamma & -\sin\gamma & 0\\ \sin\gamma & \cos\gamma & 0\\ 0 & 0 & 1\end{bmatrix}. \tag{2.47}$$

Direct modeling

The first step of directly modeling the dynamics is to select a frame where they should be modeled. In this case, it makes sense to choose a frame fixed to the suspension point whose orientation is that of the platform. It is clear that this frame is fixed with respect to the rigid body, as the body itself is fixed to the suspension point.

We find the equivalent mass moment of inertia with the suspension point as reference point using the parallel axis theorem,

$$ {}_{\mathrm{P}}\Theta_{\mathrm{P}}^{\mathrm{S}} = {}_{\mathrm{P}}\Theta_{\mathrm{P}}^{\mathrm{CoM}} + m_{\mathrm{P}}(\|{}_{\mathrm{P}}r_{\mathrm{SP}}\|_2^2 I - {}_{\mathrm{P}}r_{\mathrm{SP}}\,{}_{\mathrm{P}}r_{\mathrm{SP}}^{\mathrm{T}}) = {}_{\mathrm{P}}\Theta_{\mathrm{P}}^{\mathrm{CoM}} - m_{\mathrm{P}}({}_{\mathrm{P}}r_{\mathrm{SP}})_{\times}^2. \tag{2.48} $$

${}_{\mathrm{P}}\Theta_{\mathrm{P}}^{\mathrm{CoM}}$ and ${}_{\mathrm{P}}r_{\mathrm{SP}}$ being constants makes ${}_{\mathrm{P}}\Theta_{\mathrm{P}}^{\mathrm{S}}$ a constant as well.

Next, we compute ${}_{\mathrm{P}}\omega_{\mathrm{P}}$ as a function of q and $\dot{q}$,

$$ \begin{aligned} {}_{\mathrm{P}}\omega_{\mathrm{P}} &= \begin{bmatrix} 0 \\ 0 \\ \dot{\gamma} \end{bmatrix} + R_z(\gamma)^{\mathrm{T}} \left(\begin{bmatrix} 0 \\ \dot{\beta} \\ 0 \end{bmatrix} + R_y(\beta)^{\mathrm{T}} \begin{bmatrix} \dot{\alpha} \\ 0 \\ 0 \end{bmatrix} \right) \\ &= \left(\begin{bmatrix} 0 & 0 & 0 \\ 0 & 0 & 0 \\ 0 & 0 & 1 \end{bmatrix} + R_z(\gamma)^{\mathrm{T}} \left(\begin{bmatrix} 0 & 0 & 0 \\ 0 & 1 & 0 \\ 0 & 0 & 0 \end{bmatrix} + R_y(\beta)^{\mathrm{T}} \begin{bmatrix} 1 & 0 & 0 \\ 0 & 0 & 0 \\ 0 & 0 & 0 \end{bmatrix} \right) \right) \begin{bmatrix} \dot{\alpha} \\ \dot{\beta} \\ \dot{\gamma} \end{bmatrix} \\ &= \begin{bmatrix} \cos\beta\cos\gamma & \sin\gamma & 0 \\ -\cos\beta\sin\gamma & \cos\gamma & 0 \\ \sin\beta & 0 & 1 \end{bmatrix} \begin{bmatrix} \dot{\alpha} \\ \dot{\beta} \\ \dot{\gamma} \end{bmatrix} = J_{\mathrm{R}}(q)\dot{q}, \end{aligned} \tag{2.49} $$

where we found the rotational Jacobian $J_{\mathrm{R}}(q)$.

It's derivative with respect to q is

$$ \frac{\delta}{\delta t} J_{\mathrm{R}}(q) = \begin{bmatrix} \cos\beta\cos\gamma & \sin\gamma & 0 \\ -\cos\beta\sin\gamma & \cos\gamma & 0 \\ \sin\beta & 0 & 1 \end{bmatrix}. \tag{2.50} $$

The angular velocity's time derivative is

$$ \begin{aligned} {}_{\mathrm{P}}\dot{\omega}_{\mathrm{P}} &= \begin{bmatrix} -\sin\beta\cos\gamma\dot{\beta} - \cos\beta\sin\gamma\dot{\gamma} & \cos\gamma\dot{\gamma} & 0 \\ \sin\beta\sin\gamma\dot{\beta} - \cos\beta\cos\gamma\dot{\gamma} & -\sin\gamma\dot{\gamma} & 0 \\ \cos\beta\dot{\beta} & 0 & 1 \end{bmatrix} \begin{bmatrix} \dot{\alpha} \\ \dot{\beta} \\ \dot{\gamma} \end{bmatrix} \\ &+ \begin{bmatrix} \cos\beta\cos\gamma & \sin\gamma & 0 \\ -\cos\beta\sin\gamma & \cos\gamma & 0 \\ \sin\beta & 0 & 1 \end{bmatrix} \begin{bmatrix} \ddot{\alpha} \\ \ddot{\beta} \\ \ddot{\gamma} \end{bmatrix} \\ &= \dot{J}_{\mathrm{R}}(q, \dot{q})\dot{q} + J_{\mathrm{R}}(q)\ddot{q}. \end{aligned} \tag{2.51} $$

This allows us to write the absolute time derivative of the pendulum's angular momentum as

$$({}_{\mathrm{P}}\Theta^{\mathrm{S}}_{\mathrm{P}}{}_{\mathrm{P}}\omega_{\mathrm{P}})_{\delta t} = {}_{\mathrm{P}}\Theta^{\mathrm{S}}_{\mathrm{P}}{}_{\mathrm{P}}\dot{\omega}_{\mathrm{P}} + {}_{\mathrm{P}}\omega_{\mathrm{P}} \times {}_{\mathrm{P}}\Theta^{\mathrm{S}}_{\mathrm{P}}{}_{\mathrm{P}}\omega_{\mathrm{P}}. \tag{2.52}$$

Now, we find the equivalent torques caused by ${}_{\mathrm{P}}f_{\mathrm{in}}$, which acts on the platform as

$${}_{\mathrm{P}}\tau^{\mathrm{S}} = {}_{\mathrm{P}}\tau^{\mathrm{P}}_{\mathrm{in}} + {}_{\mathrm{P}}r_{\mathrm{SP}} \times {}_{\mathrm{P}}\varphi^{\mathrm{P}}_{\mathrm{in}}. \tag{2.53}$$

Finally, we obtain the dynamics as

$$({}_{\mathrm{P}}\Theta^{\mathrm{S}}_{\mathrm{P}}{}_{\mathrm{P}}\omega_{\mathrm{P}})_{\delta t} = {}_{\mathrm{P}}\tau^{\mathrm{S}} \tag{2.54a}$$

$${}_{\mathrm{P}}\dot{\omega}_{\mathrm{P}} = ({}_{\mathrm{P}}\Theta^{\mathrm{S}}_{\mathrm{P}})^{-1}({}_{\mathrm{P}}\tau^{\mathrm{S}} - {}_{\mathrm{P}}\omega_{\mathrm{P}} \times {}_{\mathrm{P}}\Theta^{\mathrm{S}}_{\mathrm{P}}{}_{\mathrm{P}}\omega_{\mathrm{P}}) \tag{2.54b}$$

$$\ddot{q} = J_{\mathrm{R}}^{-1}(({}_{\mathrm{P}}\Theta^{\mathrm{S}}_{\mathrm{P}})^{-1}({}_{\mathrm{P}}\tau^{\mathrm{S}} - (J_{\mathrm{R}}\dot{q}) \times {}_{\mathrm{P}}\Theta^{\mathrm{S}}_{\mathrm{P}}J_{\mathrm{R}}\dot{q}) - \dot{J}_{\mathrm{R}}\dot{q}). \tag{2.54c}$$

Lagrange 2 formalism

Another way to derive ${}_{\mathrm{P}}\omega_{\mathrm{P}}$ is to make use of (1.19b), yielding

$$\begin{aligned}({}_{\mathrm{P}}\omega_{\mathrm{P}})_{\times} &= {}_{\mathrm{I}}R^{\mathrm{T}}_{\mathrm{P}}{}_{\mathrm{I}}\dot{R}_{\mathrm{P}} \\ &= \begin{bmatrix} 0 & -\sin\beta\dot{\alpha} - \dot{\gamma} & -\cos\beta\sin\gamma\dot{\alpha} + \cos\gamma\dot{\beta} \\ \sin\beta\dot{\alpha} + \dot{\gamma} & 0 & -\cos\beta\cos\gamma\dot{\alpha} - \sin\gamma\dot{\beta} \\ \cos\beta\sin\gamma\dot{\alpha} - \cos\gamma\dot{\beta} & \cos\beta\cos\gamma\dot{\alpha} + \sin\gamma\dot{\beta} & 0 \end{bmatrix}.\end{aligned} \tag{2.55}$$

We also need the linear velocity, ${}_{\mathrm{I}}v_{\mathrm{P}}$. For this, we first define the position of the body CoM in terms of q as

$${}_{\mathrm{I}}r_{\mathrm{IP}} = {}_{\mathrm{I}}R_{\mathrm{P}}{}_{\mathrm{P}}r_{\mathrm{IP}} = {}_{\mathrm{I}}R_{\mathrm{P}} \begin{bmatrix} 0 \\ 0 \\ -l \end{bmatrix} = \begin{bmatrix} -\sin\beta l \\ \cos\beta\sin\alpha l \\ -\cos\beta\cos\alpha l \end{bmatrix}. \tag{2.56}$$

Taking its derivative, we find the linear velocity of the body CoM,

$${}_{\mathrm{I}}v_{\mathrm{P}} = \begin{bmatrix} 0 & -\cos\beta l & 0 \\ \cos\beta\cos\alpha l & -\sin\beta\sin\alpha l & 0 \\ \cos\beta\sin\alpha l & \sin\beta\cos\alpha l & 0 \end{bmatrix} \dot{q} = J_{\mathrm{T}}(q)\dot{q} = {}_{\mathrm{I}}R_{\mathrm{P}}({}_{\mathrm{P}}r_{\mathrm{SP}})_{\times}J_{\mathrm{R}}(q)\dot{q}, \tag{2.57}$$

where we found the translational Jacobian $J_{\mathrm{T}}(q)$ along with a useful identity relating it to the rotational Jacobian.

Using this identity, we can compute the kinetic energy,

$$E_{\mathrm{kin}} = \frac{1}{2}m_{\mathrm{P}}{}_{\mathrm{P}}v^{\mathrm{T}}_{\mathrm{P}}{}_{\mathrm{P}}v_{\mathrm{P}} + \frac{1}{2}{}_{\mathrm{P}}\omega^{\mathrm{T}}_{\mathrm{P}}{}_{\mathrm{P}}\Theta^{\mathrm{CoM}}_{\mathrm{P}}{}_{\mathrm{P}}\omega_{\mathrm{P}} = \frac{1}{2}\dot{q}^{\mathrm{T}}J^{\mathrm{T}}_{\mathrm{R}}{}_{\mathrm{P}}\Theta^{\mathrm{S}}_{\mathrm{P}}J_{\mathrm{R}}\dot{q}. \tag{2.58}$$

We don't explicitly consider gravity (it could be expressed in f_{in}, though) or any other potential field with respect to which there could be potential energy.

Next, we use the Jacobians to map the forces and torques acting on P into the configuration space, finding

$$Q = J_{\mathrm{T}}^{\mathrm{T}}{}_{\mathrm{I}}R_{\mathrm{PP}}\varphi_{\mathrm{in}}^{\mathrm{S}} + J_{\mathrm{R}}^{\mathrm{T}}{}_{\mathrm{P}}\tau_{\mathrm{in}}^{\mathrm{S}} = J_{\mathrm{R}}^{\mathrm{T}}(({}_{\mathrm{P}}r_{\mathrm{SP}})_{\times}{}_{\mathrm{P}}\varphi_{\mathrm{in}}^{\mathrm{S}} + \tau_{\mathrm{in}}^{\mathrm{S}}) = J_{\mathrm{R}}^{\mathrm{T}}{}_{\mathrm{P}}\tau^{\mathrm{S}}. \tag{2.59}$$

Now we can directly transition to differentiating the kinetic energy, first with respect to q (using $\frac{\delta}{\delta q}J_{\mathrm{R}}(q)\dot{q} = \dot{J}_{\mathrm{R}}(q)$), yielding

$$\frac{\delta}{\delta q}E_{\mathrm{kin}} = \dot{J}_{\mathrm{R}}^{\mathrm{T}}{}_{\mathrm{P}}\Theta_{\mathrm{P}}^{\mathrm{S}}J_{\mathrm{R}}\dot{q}. \tag{2.60}$$

Next, we differentiate the energy with respect to $\dot{q}$ and subsequently take the absolute time derivative,

$$\begin{aligned}\left(\frac{\delta}{\delta \dot{q}}E_{\mathrm{kin}}\right)_{\delta t} &= (J_{\mathrm{R}}^{\mathrm{T}}{}_{\mathrm{P}}\Theta_{\mathrm{P}}^{\mathrm{S}}J_{\mathrm{R}}\dot{q})_{\delta t} \\ &= J_{\mathrm{R}}^{\mathrm{T}}{}_{\mathrm{P}}\Theta_{\mathrm{P}}^{\mathrm{S}}J_{\mathrm{R}}\ddot{q} + \dot{J}_{\mathrm{R}}^{\mathrm{T}}{}_{\mathrm{P}}\Theta_{\mathrm{P}}^{\mathrm{S}}J_{\mathrm{R}}\dot{q} + J_{\mathrm{R}}^{\mathrm{T}}{}_{\mathrm{P}}(J_{\mathrm{R}}\dot{q})_{\times}\Theta_{\mathrm{P}}^{\mathrm{S}}J_{\mathrm{R}}\dot{q} + J_{\mathrm{R}}^{\mathrm{T}}{}_{\mathrm{P}}\Theta_{\mathrm{P}}^{\mathrm{S}}\dot{J}_{\mathrm{R}}\dot{q}.\end{aligned} \tag{2.61}$$

Finally, we plug into (2.15) and obtain

$$\left(\frac{\delta}{\delta \dot{q}}E_{\mathrm{kin}}\right)_{\delta t} - \frac{\delta}{\delta q}E_{\mathrm{kin}} = J_{\mathrm{R}}^{\mathrm{T}}{}_{\mathrm{P}}\Theta_{\mathrm{P}}^{\mathrm{S}}J_{\mathrm{R}}\ddot{q} + J_{\mathrm{R}}^{\mathrm{T}}{}_{\mathrm{P}}(J_{\mathrm{R}}\dot{q})_{\times}\Theta_{\mathrm{P}}^{\mathrm{S}}J_{\mathrm{R}}\dot{q} + J_{\mathrm{R}}^{\mathrm{T}}{}_{\mathrm{P}}\Theta_{\mathrm{P}}^{\mathrm{S}}\dot{J}_{\mathrm{R}}\dot{q} = Q \tag{2.62a}$$

$$\begin{aligned}\ddot{q} &= J_{\mathrm{R}}^{-1}({}_{\mathrm{P}}\Theta_{\mathrm{P}}^{\mathrm{S}})^{-1}J_{\mathrm{R}}^{-\mathrm{T}}(Q - J_{\mathrm{R}}^{\mathrm{T}}{}_{\mathrm{P}}(J_{\mathrm{R}}\dot{q})_{\times}\Theta_{\mathrm{P}}^{\mathrm{S}}J_{\mathrm{R}}\dot{q} - J_{\mathrm{R}}^{\mathrm{T}}{}_{\mathrm{P}}\Theta_{\mathrm{P}}^{\mathrm{S}}\dot{J}_{\mathrm{R}}\dot{q}) \\ &= J_{\mathrm{R}}^{-1}(({}_{\mathrm{P}}\Theta_{\mathrm{P}}^{\mathrm{S}})^{-1}({}_{\mathrm{P}}\tau^{\mathrm{S}} - (J_{\mathrm{R}}\dot{q})_{\times}\Theta_{\mathrm{P}}^{\mathrm{S}}J_{\mathrm{R}}\dot{q}) - \dot{J}_{\mathrm{R}}\dot{q}).\end{aligned} \tag{2.62b}$$

As expected, (2.62b) is identical to (2.54).

2.4.2 Constrained rigid body

For a rigid pendulum, we can consider the entire assembly as one rigid body revolving around the suspension point, fixing the suspension point itself to the rigid body. As a result, the suspension point's position will be constant with respect to any other frame fixed to the pendulum,

$${}_{\mathrm{P}}R_{\mathrm{SS}}r_{\mathrm{SP}} = {}_{\mathrm{S}}R_{\mathrm{P}}^{\mathrm{T}}{}_{\mathrm{S}}r_{\mathrm{SP}} = \mathit{const}. \tag{2.63}$$

To obtain a Pfaffian constraint matrix, we take its time derivative,

$$-({}_{\mathrm{P}}\omega_{\mathrm{P}})_{\times}{}_{\mathrm{S}}R_{\mathrm{P}}^{\mathrm{T}}{}_{\mathrm{S}}r_{\mathrm{SP}} + {}_{\mathrm{S}}R_{\mathrm{P}}^{\mathrm{T}}{}_{\mathrm{S}}v_{\mathrm{P}} = {}_{\mathrm{P}}r_{\mathrm{SP}} \times {}_{\mathrm{P}}\omega_{\mathrm{P}} + {}_{\mathrm{P}}v_{\mathrm{P}} = \begin{bmatrix}({}_{\mathrm{P}}r_{\mathrm{SP}})_{\times} & I\end{bmatrix}\begin{bmatrix}{}_{\mathrm{P}}\omega_{\mathrm{P}} \\ {}_{\mathrm{P}}v_{\mathrm{P}}\end{bmatrix} = A_{\mathrm{PP}}V_{\mathrm{P}} = 0. \tag{2.64}$$

We obtain the rigid body equation as described in (1.8) with ${}_{\mathrm{S}}v_{\mathrm{S}} = 0$. This is reasonable considering that the constraint formulated in (2.63) was motivated precisely by the observation that the suspension point (which is an inertial point) is fixed to the pendulum body. In this case, A_{P} is constant.

The relationship between ${}_{\mathrm{P}}V_{\mathrm{P}}$ and $\dot{q}$ is given by (2.49) and (2.57) as

$$
{}_{\mathrm{P}}V_{\mathrm{P}} = \begin{bmatrix} {}_{\mathrm{P}}\omega_{\mathrm{P}} \\ {}_{\mathrm{P}}v_{\mathrm{P}} \end{bmatrix} = \begin{bmatrix} J_{\mathrm{R}}(q) \\ J_{\mathrm{T}}(q) \end{bmatrix} \dot{q} = \begin{bmatrix} I \\ -({}_{\mathrm{P}}r_{\mathrm{SP}})_{\times} \end{bmatrix} J_{\mathrm{R}}(q)\dot{q}. \tag{2.65}
$$

Now, it is clear that the velocities computed using the generalized coordinates always follow the constraints, i. e.

$$
A_{\mathrm{PP}}V_{\mathrm{P}} = \begin{bmatrix} ({}_{\mathrm{P}}r_{\mathrm{SP}})_{\times} & I \end{bmatrix} \begin{bmatrix} I \\ -({}_{\mathrm{P}}r_{\mathrm{SP}})_{\times} \end{bmatrix} J_{\mathrm{R}}(q)\dot{q} = (({}_{\mathrm{P}}r_{\mathrm{SP}})_{\times} - ({}_{\mathrm{P}}r_{\mathrm{SP}})_{\times})J_{\mathrm{R}}(q)\dot{q} = 0. \tag{2.66}
$$

Thus, we have shown that (2.43) holds, and therefore the chosen constraints lead to the same dynamics as (2.54).

Chapter 3

Modeling the cable-suspended aerial manipulator

Most observers are model-based, at least to an extent. Including known information about the system properties can dramatically improve performance when compared to model-free approaches. These improvements, however, strongly depend on the accuracy of the underlying model and its parameters. Poor selection of these can lead to decreased performance even to the point of divergence.

In this chapter, we compare five different ways to model the SAM, as shown in Fig. 3.1, and propose a way to identify their respective parameters.

While the SAM interacts with the environment, its end effector pose with respect to the environment is fixed and/or known. Through knowledge of the joint angles and the manipulator's forward kinematics, this also implies knowledge of the base platform pose and as such of the whole system. In general, the platform tends to be quasi-stationary while the manipulator operates, whereas the manipulator tends to be stationary while the platform is moving. The proposed observer targets the platform pose, which has a tendency to change only with the manipulator being fixed. This motivates the simplification being used throughout this chapter, which regards the entire SAM including its manipulator and the base as a single rigid body.

3.1 Rigid pendulum

The least complex way to model the SAM is as a spherical pendulum (see Fig. 3.1a). The respective Pfaffian constraint matrix has been derived in § 2.4.2.

The major benefit of this model is its low complexity. For instance, $p_\times$ and therefore A are constant in the body frame.

However, the real system does not always respect (2.64) in its entirety.

3.2 Rigid double pendulum

When the SAM is operating outdoors, it is usually connected to its carrying device through a hook which comes with a considerable mass. As a result, the kinematics and the dynamics of a rigid pendulum fail to accurately represent the real system.

Introducing another mass representing the hook into the model can be done by extending it to a double pendulum (see Fig. 3.1b). This means that the angular and linear velocities of the hook are related according to its single pendulum properties. The analogous relationship for the platform is similar, but needs to respect the linear velocity of the hook itself, leading the relations

$$\begin{aligned} v_{\mathrm{H}} &= \omega_{\mathrm{H}} \times p_{\mathrm{H}} && (3.1\mathrm{a}) \\ v_{\mathrm{P}} &= v_{\mathrm{H}} + \omega_{\mathrm{P}} \times r_{\mathrm{HP}}. && (3.1\mathrm{b}) \end{aligned}$$

We can write these relations again using a Pfaffian constraint matrix,

$$\begin{bmatrix} ({}_{\mathrm{H}}p_{\mathrm{H}})_\times & I & 0 & 0 \\ 0 & -{}_{\mathrm{P}}R_{\mathrm{H}} & ({}_{\mathrm{P}}r_{\mathrm{HP}})_\times & I \end{bmatrix} \begin{bmatrix} {}_{\mathrm{H}}\omega_{\mathrm{H}} \\ {}_{\mathrm{H}}v_{\mathrm{H}} \\ {}_{\mathrm{P}}\omega_{\mathrm{P}} \\ {}_{\mathrm{P}}v_{\mathrm{P}} \end{bmatrix} = AV = 0. \tag{3.2}$$

Note that there's a coupling term (the rotation matrix that is applied to the hook's linear velocity) in the constraint matrix. This is a result of the constraints not only acting on the rigid bodies individually, but also on their relative motion.

3.3 Compliant pendulum

The cables that the SAM is suspended from are not perfectly rigid in reality. To the contrary, they exhibit stiffness and damping properties. In some cases (see § 4.6.2), these properties play an important role and the rigid pendulum reaches its limits.

The model proposed here can be seen as a rigid pendulum with *soft constraints*, see Fig. 3.1c. Instead of strictly ensuring a set of constraints, it respects them using wrenches that depend on the violation of the constraints.

In particular, we model the SAM's suspension to consist of a multidimensional system consisting of a spring and a parallel damper. We assume those to connect the SAM to an ideal body that follows the hard constraints and represents the pose at which the spring is relaxed. We choose the pose of this ideal body as translationally close as possible to the SAM pose: Both their origins and the suspension point lie on one line. The ideal body's origin (p_{i}) lies on that line at a distance matching the suspension's length (l_0). It's orientation is chosen such that the z-axis (z_{i}) points towards the suspension point, satisfying

$$\begin{aligned} p_{\mathrm{i}} &= \frac{l_0}{\|p_{\mathrm{P}}\|_2} p_{\mathrm{P}} && (3.3\mathrm{a}) \\ z_{\mathrm{i}} &= -\frac{p_{\mathrm{P}}}{\|p_{\mathrm{P}}\|_2}. && (3.3\mathrm{b}) \end{aligned}$$

We model the soft constraints' spring with a linear force pulling the SAM toward the ideal body, and a torque acting around an axis orthogonal to both z-axes.

For the damping, we only consider those velocities that disobey the hard constraints. We find those using $V_{\|} = A^{\mathrm{T}}(AA^{\mathrm{T}})^{-1}AV$.

In summary, this defines the soft constraint wrench acting on the rigid body representing the SAM to

$$f_{\mathrm{c}} = K \begin{bmatrix} \frac{z_{\mathrm{P}} \times z_{\mathrm{i}}}{\|z_{\mathrm{P}} \times z_{\mathrm{i}}\|_2} \angle(z_{\mathrm{P}}, z_{\mathrm{i}}) \\ p_{\mathrm{i}} - p_{\mathrm{P}} \end{bmatrix} - DA^{\mathrm{T}}(AA^{\mathrm{T}})^{-1}AV. \tag{3.4}$$

Here, K and D are the stiffness and damping gains, respectively. For additional accuracy with respect to the real system, we only engage f_c once $\|p_{\mathrm{P}}\|_2 > l$, i. e. when the suspension is under tension. In addition to that, we can also disengage the soft constraints once its force part acts in the opposite direction than towards the suspension point, which could happen even when $\|p_{\mathrm{P}}\|_2 < l$ for high damping gains.

These considerations might improve accuracy, but they also considerably increase the complexity and introduce additional nonlinearities.

3.4 Compliant double pendulum

Of course, the nonrigid properties of the cables can also show in the case that the SAM is mounted to a hook or another intermediary mass, see Fig. 3.1d.

The constraint wrench acting on the SAM is computed identically to what is described in (3.4). The line between the SAM's and the intermediary mass' origins marks the direction of the ideal body's z-axis. On this same line lies the ideal body's origin at a distance matching the suspension's length from the intermediary mass.

Since the intermediary mass is suspended from just a single cable, this cable's compliance will not cause previously unrespected rotation of the hook, hence we model this cable simply as a linear spring. Again, this spring connects the hook to an ideal body that respects the hard constraints.

Effectively, we combine hard and soft constraints for the intermediary mass: There is a soft constraint on its position along it's z-axis, and there's hard constraints on its angular velocity. The hard constraints can be expressed as

$$v = \omega \times p + v_{z_{\mathrm{H}}}. \tag{3.5}$$

Note that the linear velocity in the body frame's z-direction is no longer required to be zero. In fact, since the body frame of the intermediary mass (H) is chosen such that the z-axis points towards the suspension point, w have ${}_{\mathrm{H}}p_{\mathrm{H}} = \begin{bmatrix} 0 & 0 & l(t) \end{bmatrix}^{\mathrm{T}}$. This directly implies a way to reduce A to allow for motion along the body z-axis,

$$\begin{bmatrix} ({}_{\mathrm{H}}p_{\mathrm{H}})_{\times} & I \end{bmatrix} \begin{bmatrix} {}_{\mathrm{H}}\omega_{\mathrm{H}} \\ {}_{\mathrm{H}}v_{\mathrm{H}} \end{bmatrix} - \begin{bmatrix} 0 \\ {}_{\mathrm{H}}v_{z_{\mathrm{H}}} \end{bmatrix} = \begin{bmatrix} 0 & -l(t) & 0 & 1 & 0 & 0 \\ l(t) & 0 & 0 & 0 & 1 & 0 \\ 0 & 0 & 0 & 0 & 0 & 1-1 \end{bmatrix} V = \begin{bmatrix} A_{\mathrm{r}} \\ 0 \end{bmatrix} V. \tag{3.6}$$

Plugging into 2.25, we can see that a soft constraint force in z_H-direction does not influence the hard constraint forces because $A_\mathrm{r}\Lambda^{-1}f_\mathrm{sc} = A_\mathrm{r}\begin{bmatrix} 0 \\ m^{-1}k(l(t)-l_0) \end{bmatrix} = 0$. With this, we can finally write the full constraint forces for the system as

$$f_{\mathrm{c,\ P}} = K \begin{bmatrix} 0 \\ p_{\mathrm{i,\ H}} - p_\mathrm{H} \\ \frac{z_\mathrm{P} \times z_{\mathrm{i,\ P}}}{\|z_\mathrm{P} \times z_{\mathrm{i,\ P}}\|_2} \angle(z_\mathrm{P}, z_{\mathrm{i,\ P}}) \\ p_{\mathrm{i,\ P}} - p_\mathrm{P} \end{bmatrix} - DA^\mathrm{T}(AA^\mathrm{T})^{-1}AV + \begin{bmatrix} A_\mathrm{r}^\mathrm{T}\lambda_{\mathrm{c,\ r}} \\ 0 \end{bmatrix}. \tag{3.7}$$

Note that the velocities to be dampened are found based on the full hard constraints, not on the reduced constraints.

3.5 Compliant 4-cable suspension

To precisely model exactly what is happening in the real system with very little abstraction, we can model every cable individually (as sketched in Fig. 3.1e) as a linear spring-damper combination that only engages under tension and only produces pulling forces. Their respective forces are modeled as

$$l(t) = \|p_\mathrm{B} - p_\mathrm{A}\|_2 \tag{3.8a}$$

$$\dot{l}(t) = \frac{p_\mathrm{B} - p_\mathrm{A}}{l(t)}(v_\mathrm{B} - v_\mathrm{A}) \tag{3.8b}$$

$$f_{\mathrm{c,\ AB}} = \frac{p_\mathrm{B} - p_\mathrm{A}}{\|p_\mathrm{B} - p_\mathrm{A}\|_2} \max(0, k(l(t) - l_0) - \dot{l}(t)). \tag{3.8c}$$

Here, l_0 denotes the relaxed length of the modeled spring.

Denoting the cable mounting points at the SAM as C1, C2, and C3, we can find the resulting constraint wrench on the CoM as

$$\begin{aligned} f_{\mathrm{c,\ P}} &= \mathrm{Ad}^\mathrm{T}_{\mathrm{C1}g_\mathrm{P}} \begin{bmatrix} 0 \\ f_{\mathrm{c,\ C1H}} \end{bmatrix} + \mathrm{Ad}^\mathrm{T}_{\mathrm{C2}g_\mathrm{P}} \begin{bmatrix} 0 \\ f_{\mathrm{c,\ C2H}} \end{bmatrix} + \mathrm{Ad}^\mathrm{T}_{\mathrm{C3}g_\mathrm{P}} \begin{bmatrix} 0 \\ f_{\mathrm{c,\ C3H}} \end{bmatrix} \\ &= \begin{bmatrix} r_{\mathrm{c,\ PC1}} \times f_{\mathrm{c,\ C1H}} + r_{\mathrm{c,\ PC2}} \times f_{\mathrm{c,\ C2H}} + r_{\mathrm{c,\ PC3}} \times f_{\mathrm{c,\ C3H}} \\ f_{\mathrm{c,\ C1H}} + f_{\mathrm{c,\ C2H}} + f_{\mathrm{c,\ C3H}} \end{bmatrix}. \end{aligned} \tag{3.9}$$

This serves as a good example on how to apply the transposed transformation adjoints to compute the equivalent wrenches in the CoM.

We assume the intermediary mass to behave like a point mass, with all cable forces pointing directly at its CoM. Therefore, we don't consider any torques acting on it. The resulting force on the intermediary mass is

$$f_{\mathrm{c,\ H}} = -f_{\mathrm{c,\ C1H}} - f_{\mathrm{c,\ C2H}} - f_{\mathrm{c,\ C3H}} + f_{\mathrm{c,\ HS}}. \tag{3.10}$$

3.6 Modeling the entire system

Most robots consist of a serial interconnection of translational and rotational joints. Looking at these joints, they provide only a single degree of freedom each. This implies that there are 5-dimensional constraints between any two subsequent bodies of a robot of that type.

In this section, we find these constraints and a method to construct the differential equations of motion for a general robot is described.

Rotational joints

For a rotational joint, the translational velocity of the joint itself can be found from either of the connected links using the rigid body equation (1.8),

$$v_{\mathrm{J1}} = v_{\mathrm{L1}} + \omega_{\mathrm{L1}} \times r_{\mathrm{L1J1}} \tag{3.11a}$$

$$v_{\mathrm{J1}} = v_{\mathrm{L2}} + \omega_{\mathrm{L2}} \times r_{\mathrm{L2J1}}. \tag{3.11b}$$

This gives us a three-dimensional constraint on the linear velocities. In addition to that, their angular velocities are related as well, as

$$\omega_{\mathrm{L2}} = \omega_{\mathrm{L1}} + R_{\mathrm{J1}} \begin{bmatrix} 0 \\ 0 \\ \dot{q}_1 \end{bmatrix}. \tag{3.12}$$

Here, R_{J1} is the orientation of the rotational joint, with its z-axis being the axis of rotation. This equation gives us a two-dimensional constraint on the angular velocities. We can extract two independent equations by representing them in the joint frame and omitting the equation in z-direction, which contains the unknown $\dot{q}_1$. For this omitting operation, we use a *selection matrix* S, yielding

$$\begin{aligned} \begin{bmatrix} 1 & 0 & 0 \\ 0 & 1 & 0 \\ 0 & 0 & 0 \end{bmatrix} {}_{\mathrm{L1}}R_{\mathrm{J1}}^{\mathrm{T}}\,{}_{\mathrm{L1}}\omega_{\mathrm{L2}} = \begin{bmatrix} 1 & 0 & 0 \\ 0 & 1 & 0 \\ 0 & 0 & 0 \end{bmatrix} {}_{\mathrm{L1}}R_{\mathrm{J1}}^{\mathrm{T}}\,{}_{\mathrm{L1}}\omega_{\mathrm{L1}} + \begin{bmatrix} 1 & 0 & 0 \\ 0 & 1 & 0 \\ 0 & 0 & 0 \end{bmatrix} \begin{bmatrix} 0 \\ 0 \\ \dot{q}_1 \end{bmatrix} \\ S_{\mathrm{L1}}R_{\mathrm{J1}}^{\mathrm{T}}\,{}_{\mathrm{L1}}\omega_{\mathrm{L2}} = S_{\mathrm{L1}}R_{\mathrm{J1}}^{\mathrm{T}}\,{}_{\mathrm{L1}}\omega_{\mathrm{L1}}. \end{aligned} \tag{3.13}$$

If we combine (3.11) with (3.13), the Pfaffian constraint matrix is

$$A_{\mathrm{r}} = \begin{bmatrix} -({}_{\mathrm{L1}}r_{\mathrm{L1J1}})_{\times} & I & {}_{\mathrm{L1}}R_{\mathrm{L2}}({}_{\mathrm{L2}}r_{\mathrm{L2J1}})_{\times} & -{}_{\mathrm{L1}}R_{\mathrm{L2}} \\ S_{\mathrm{L1}}R_{\mathrm{J1}}^{\mathrm{T}} & 0 & -S_{\mathrm{L1}}R_{\mathrm{J1}}^{\mathrm{T}}\,{}_{\mathrm{L1}}R_{\mathrm{L2}} & 0 \end{bmatrix}, \tag{3.14}$$

where L1 and L2 denote the first and second link, respectively, and J1 is the joint between them.

Translational joints

For a translational joint, we can directly see that both bodies' rotational velocities must be identical, satisfying

$$\omega_{\mathrm{L2}} = \omega_{\mathrm{L1}}. \tag{3.15}$$

The relationship between the translational velocities is again based on the rigid body equation (1.8),

$$v_{\mathrm{L2}} = v_{\mathrm{L1}} + \omega_{\mathrm{L1}} \times r_{\mathrm{L1L2}} + R_{\mathrm{J1}} \begin{bmatrix} 0 \\ 0 \\ \dot{q}_1 \end{bmatrix}. \tag{3.16}$$

Similar to (3.13), we can extract two independent equations from (3.16),

$$S_{\mathrm{L1}} R^{\mathrm{T}}_{\mathrm{J1L1}} v_{\mathrm{L2}} = S_{\mathrm{L1}} R^{\mathrm{T}}_{\mathrm{J1L1}} v_{\mathrm{L1}} + S_{\mathrm{L1}} R^{\mathrm{T}}_{\mathrm{J1}} ({}_{\mathrm{L1}}\omega_{\mathrm{L1}} \times {}_{\mathrm{L1}}r_{\mathrm{L1L2}}). \tag{3.17}$$

Finally, the Pfaffian constraint matrix is

$$A_{\mathrm{t}} = \begin{bmatrix} I & 0 & -{}_{\mathrm{L1}}R_{\mathrm{L2}} & 0 \\ -S_{\mathrm{L1}} R^{\mathrm{T}}_{\mathrm{J1}} ({}_{\mathrm{L1}}r_{\mathrm{L1L2}})_{\times} & S_{\mathrm{L1}} R^{\mathrm{T}}_{\mathrm{J1}} & 0 & -S_{\mathrm{L1}} R^{\mathrm{T}}_{\mathrm{J1L1}} R_{\mathrm{L2}} \end{bmatrix}. \tag{3.18}$$

Constructing equations of motion

Using (3.14) and (3.18), it is possible to construct the equations of motion and those for the observer directly. For a m-link robot, m rigid bodies are considered. Generally, their equations of motion are described in (2.26) and (1.52). The constraint matrix can be constructed from the joints connecting the individual links as

$$A_{\mathrm{robot}} = \begin{bmatrix} A_{\mathrm{j1,7:12}} & 0 & 0 & 0 & \dots \\ \multicolumn{2}{c}{A_{\mathrm{j2}}} & 0 & 0 & \dots \\ 0 & \multicolumn{2}{c}{A_{\mathrm{j3}}} & 0 & \dots \\ 0 & 0 & \multicolumn{2}{c}{A_{\mathrm{j4}}} & \dots \\ \vdots & & \ddots & & \ddots \end{bmatrix}. \tag{3.19}$$

In the first row, a connection to a inertially fixed body is assumed, hence the first 6 columns of the first joint constraint matrix can be omitted.

The applied wrench f_{in} for each body consists of the two efforts in the preceding and subsequent joints, along with external wrenches, such as the gravity force. The constraint forces, which of course also act on the bodies, do not need to be computed explicitly.

This representation is sufficient for any serial robot. Using different constraints, even parallel robots or different multi-body systems can be represented in this way.

The SAM including its manipulator consists of 8 or 9 bodies depending on the configuration regarding an intermediary mass. The constraints imposed on it are the platform constraints (depending on the model), followed by 7 rotational joints. The applied wrench f_{in} can be computed using IMU measurements to obtain the gravity force, and the control inputs to obtain the joint torques and the propulsion wrench on the platform. The current pose can be extended from a single measurement anywhere on the SAM to the entire system using forward kinematics of the manipulator. In the case of a double pendulum assumption for the platform, the intermediary mass's position (and its orientation up to a rotation around its z-axis) can be found as well: We know it's exactly in the z-direction of the platform frame at a known distance. For the orientation, we know that its z-axis points towards the suspension point. We can even determine the distance between the intermediary mass and the suspension point, which gives us the option to model this connection as a translationally compliant cable instead of a rigid one, using

$$r_{\mathrm{H}} = r_{\mathrm{P}} + l_{\mathrm{P}} z_{\mathrm{P}} \tag{3.20a}$$

$$z_{\mathrm{H}} = -\frac{r_{\mathrm{H}}}{\|r_{\mathrm{H}}\|_2} \tag{3.20b}$$

$$l_{\mathrm{H}} = \|r_{\mathrm{H}}\|_2. \tag{3.20c}$$

Overall, this shows how the SAM as a whole fits into the framework used throughout this thesis.

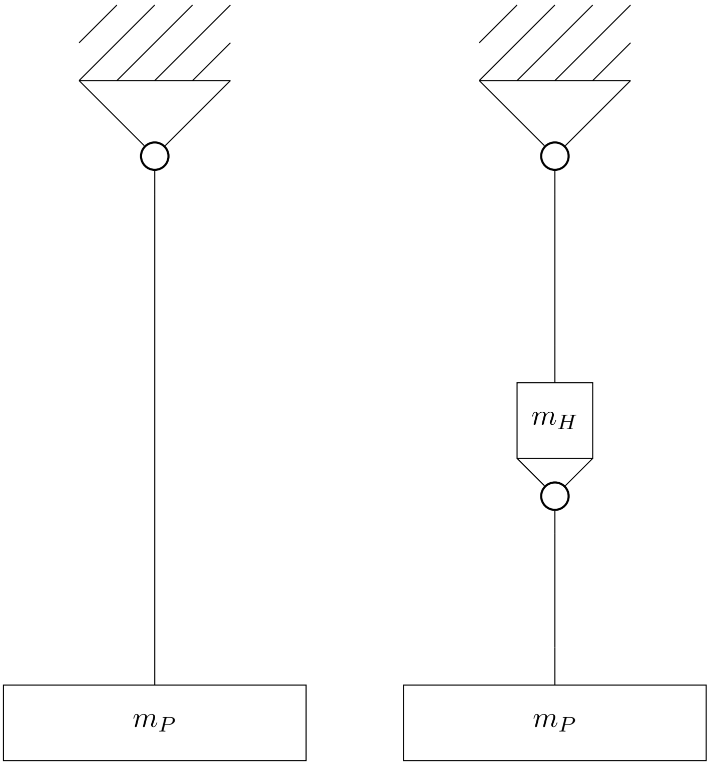

(a) Rigid pendulum (b) Rigid double pendulum

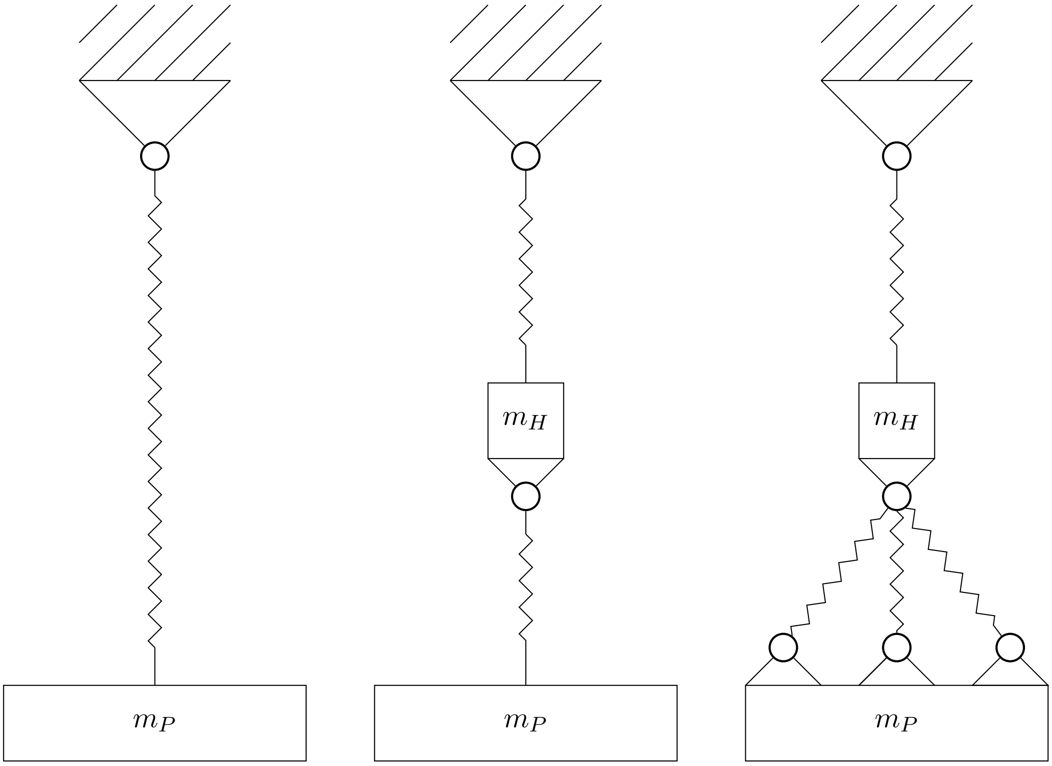

(c) Elastic pendulum (d) Elastic double pendulum (e) Individual compliant cables

Figure 3.1: Different models of the SAM

Chapter 4

System identification

The SAM is a very complex system. As a result, its exact dynamic characteristics are difficult to directly compute or measure. In this chapter, we will optimize parameters to optimally replicate experimental data in simulations.

Both single-mass models presented in § 3 will be optimally fit to data collected from experiments that are explicitly designed to highlight specific parameters' effects. After that has been done, the remaining residuals will be compared.

Finally, a model which provides a good balance between complexity and accuracy of system representation will be selected as a base for the observer.

4.1 Limited parameter space

In this application, most parameters are physically limited to a subspace of $\mathbb{R}$. In particular, masses, stiffnesses and damping parameters need to be positive and mass moments of inertia need to be positive definite. Moreover, rough estimations of the range for each parameter are often available. By limiting the parameter space accordingly, the result will be ensured to be reasonable and the optimization will be vastly accelerated.

The parameter ranges can be expressed as

$$W_{\min,i} < W_i < W_{\max,i} \tag{4.1}$$

The resulting allowed parameter space will be denoted as $\mathbb{P}$.

4.2 Starting values

Good starting values dramatically improve optimization performance. The optimization approach presented here starts by evaluating the cost function at a given number of different points randomly sampled from a uniform distribution and selecting the point with the lowest cost from those. Here, a greater number of points is expensive, so there is a tradeoff between exceptionally good starting values and execution time. It makes sense to not choose the number too high, as an optimization will follow anyways to minimize the remaining cost. With a higher number of parameters to optimize for, it becomes more justifiable to invest more time into finding good starting values, as the optimization itself is more expensive.

4.3 Numerical gradient descent

In the experiments, the absolute pose of the SAM's platform will be measured. Subsequently, simulations will be run to replicate the experimental results. After the simulation has been run, the trajectories of the experimental pose and the simulated pose will be compared and their mean-square error (MSE) will provide a cost function to minimize. Explicitly, the cost function is

$$C = \sum_{t=0}^{t_{\text{end}}} \sum_{i=0}^{n} \| (\log(g_{i,\text{gt}}^{-1}[t] \tilde{g}_i[t]))^{\vee} \|_2, \tag{4.2}$$

where t_{end} is the experiment duration, and n is the number of involved bodies. g_{gt} are the ground truth poses, and $\tilde{g}$ are the simulation results.

We don't take the mathematical difference between the poses, as this is not a meaningful operation in SE(3), but rather finding the homogeneous transformation from the simulated pose ($\tilde{g}$) to the ground truth pose (g_{gt}). In order to assess the magnitude of this mapping, we use the logarithmic map to obtain a value in $\mathfrak{se}(3)$, as this is isomorphic to $\mathbb{R}^6$. Finally we sum the squared norms of the representation in $\mathbb{R}^6$ for all measured bodies for all times.

In order to reduce the cost gradually, gradient descent will be implemented. Due to the complexity of the cost function, this will be done using *numerical gradients*, as the analytical gradient with respect to the parameters W is not easy to obtain, in particular $\frac{\delta}{\delta W} \tilde{g}$.

The numerical gradients are obtained using the central difference scheme as

$$d = (\nabla_W C)_i(W) = \frac{C(W + h e_i) - C(W - h e_i)}{2h} \tag{4.3}$$

Here, for $h \to 0$, the numerical gradient will be identical with the analytical one, so we choose a small h that is still numerically stable.

It is clear that obtaining this gradient is expensive, as for every parameter, two evaluations of C are required. Recall that every evaluation of C requires a full run of the simulation. This of course motivates efforts to simplify the simulations as much as possible, but also to reduce the number of full gradient computations.

Basic gradient descent works by iteratively evaluating the gradient at the current point in parameter space and then "stepping" a small distance in the opposite direction,

$$W_{k+1} = W_k - \alpha \nabla_W C(W_k). \tag{4.4}$$

Here, we need to ensure the parameters satisfy (4.1). To this end, we compute the updated parameters in a more conservative way, using

$$\begin{aligned} \gamma &= \min\Big(\max_{(W_k + \gamma_l \nabla_W C(W_k)) \in \mathbb{P}} \gamma_l, \alpha\Big) \\ W_{k+1} &= W_k - \gamma \nabla_W C(W_k), \end{aligned} \tag{4.5}$$

where $(W_k + \gamma_l \nabla_W C(W_k)) \in \mathbb{P} \iff W_{\min,i} < (W_{k,i} + \gamma_l (\nabla_W C(W_k))_i) < W_{\max,i}$. This constraint preserves direction, and it only scales the step size when necessary to comply with the limitations. This has the drawback of finding local minima at the parameter limits if the gradient at the limit points toward the limit, as this requires $\gamma = 0$. This special case can be handled by simply ignoring the limiting coordinate of the gradient and setting it to zero before finding γ and applying the step. The idea of this approach is that after a few steps, the gradient might point away from the border again, as we assume that the global minimum is not at the parameter limits.

In general, gradient descent works for small enough α, as the gradient always points into the direction with the largest gain per distance, so going the opposite way ensures that the value will decrease until a minimum is found. However, taking very small steps is essential for this approach, as the gradient is only valid for the exact point it's evaluated at.

Taking very small steps, however, means that a lot of steps are required to reach a minimum, which means a lot of numerical gradient evaluations are necessary.

4.3.1 Line search

One method to dynamically optimize the step size is so called line search (see [18]). For this, the minimum of the cost function along the direction of the gradient is found. This is a function $f : \mathbb{R} \to \mathbb{R}$, so it is comparatively easy to analyze. For instance, finding the numerical derivative with respect to distance traveled in the gradient direction takes only 2 function evaluations instead of $2n$ that a full gradient takes, using

$$\frac{\delta}{\delta\mu} C = \frac{C(W - \mu\nabla_W C - h\nabla_W C) - C(W - \mu\nabla_W C + h\nabla_W C)}{2h}. \tag{4.6}$$

It is clear that there is a minimum where the derivative's value changes from a negative to a positive value. We already know that the derivative has a negative value at $\mu = 0$. Note that there might be multiple minima along the line; we will try to find the minimum closest to the current point. For this, we gradually increase μ until we encounter a positive value of the derivative. A quick approach to this is to iteratively multiply μ by a factor $m > 1$,

$$\mu_{k+1} = m\mu_k. \tag{4.7}$$

Once we find a μ_k with a positive derivative, we know that the minimum must be between $\mu_l = \mu_{k-1}$ and $\mu_r = \mu_k$. In order to find the exact point, we use bisection.

We iteratively evaluate the derivative in the middle $\mu_m = 0.5(\mu_r + \mu_l)$ between the right border μ_r, at which the derivative is positive, and the left border μ_l, at which it's negative. In case the derivative in the middle is positive, it becomes the new right border ($\mu_r = \mu_m$), if it's negative, it becomes the new left border ($\mu_l = \mu_m$). This way, the distance between the borders (in between which the minimum must lie) exponentially decreases: every iteration, it halves.

Algorithmus 4.1 : Bisection algorithm

```
Data : $\mu_l$, $\mu_r, \varepsilon$
Result : $\mu_{\text{opt}}$
begin
    while $|\mu_r - \mu_l| > \varepsilon$ do
        $\mu_m = 0.5(\mu_r + \mu_l)$
        if $\frac{\delta}{\delta\mu} C\Big|_{\mu_m} > 0$ then
            $\mu_r = \mu_m$
        else
            $\mu_l = \mu_m$
    $\mu_{\text{opt}} = \mu_m$
```

4.3.2 Adam

In case of a small number of parameters, line search might be comparatively expensive in relation to the gradient evaluation. In this case, it can be more efficient to stick closer to basic gradient descent.

However, a lot of research has been done in this field as it is an important part of deep learning algorithms. One typically well performing optimization algorithm is Adaptive Moment Estimation (Adam) as presented in [9].

Here, both moving averages of the gradient (m) and its squared norm (p) are computed and used for the descent. This leads to the update rules

$$m[k+1] = \frac{1}{1-\beta_1^{[}k+1]}(\beta_1 m[k] + (1-\beta_1)\nabla_W C) \tag{4.8a}$$

$$v[k+1] = \frac{2}{1-\beta_2^{[}k+1]}(\beta_2 v[k] + (1-\beta_2)\|\nabla_W C\|_2^2) \tag{4.8b}$$

$$W[k+1] = W[k] - \frac{1}{\sqrt{v[k+1]}+\varepsilon}\alpha m[k+1]. \tag{4.8c}$$

The major benefit of using the moving average gradients in this application is that it is more robust against noise in the gradient, which is likely to occur in numerical gradients based on experimental data.

4.4 Local minima

Although gradient descent will usually converge to a minimum, it is not guaranteed that this will be the global minimum. In fact, in high-dimensional optimization problems, a lot of global minima exist, with sometimes dramatically high cost residuals.

In this application, it is undesirable to find a local minimum with high cost, as it doesn't perform well at representing the real data. Thus, the optimization algorithm used here identifies local minima .

Typically, a local minimum is easy to identify as convergence at a suspiciously high cost. It makes sense to define this "suspiciously high" cost in terms of the convergence criteria. For instance, if we are looking for a final cost of C_{desired}, it makes sense to select the threshold to classify a local minimum as useless at any cost higher than $C_{\text{threshold}} = 1.5C_{\text{desired}}$.

After a local minimum has been identified, it will be classified and stored as such. Then, new starting parameters will be found to optimize from, with the intention to find a better minimum.

4.4.1 Restarting the optimization after finding a local minimum

After finding local minima, it is desirable to not reach them again from different starting values. As such, it is meaningful to keep track of both the starting values and the respective minima reached from there. Both can subsequently be avoided when selecting new starting values and while optimizing from there.

It is justifiable to invest a considerable effort in finding a meaningful starting point and in avoiding previously explored minima. Therefore, we again test multiple possible starting values, as described in § 4.2.

The cost function however will be extended by potential terms depending on the distance to previously explored points to push the exploration into a "new" direction,

$$C = \sum_{t=0}^{t_{\text{end}}} \sum_{i=0}^{n} \|(\log(g_{i,\text{gt}}^{-1}(t)\tilde{g}_i(t)))^{\vee}\|_2 + \sum_{k=0}^{m} \frac{1}{\|W - W_k\|_2^2}\theta. \tag{4.9}$$

$\theta < 1$ is the intensity of the local minima-avoiding potential field. The intention is to increase the cost around and at local minima that have been explored earlier such that they don't appear as local minima anymore, like filling potholes in a damaged street.

For the optimization, the repelling effect for the previous starting points will be disabled, as it is not meaningful.

Once the optimization starts to converge, this potential field will be entirely disabled.

4.5 Convergence handling

It is useful to detect when convergence takes place. It can be used to engage active parameter decay, or to restart the optimization if it is at a high-cost local minimum.

4.5.1 Convergence indicators

There are several indicators which suggest that the optimization is approaching a minimum.

Differential quotient

It is useful to identify if the cost or the parameters circle around a certain point over time, as this can indicate convergence. To this end, the differential quotient of the values can be taken over a few iterations. It makes sense to do so over an uneven number r of iterations, as the values tend to switch between two neighborhoods of values every iteration as a result of overshoot. Then, the differential quotient is defined as

$$R_{\mathrm{DQ}}[k] = \frac{X[k] - X[k-r]}{r}, \tag{4.10}$$

where X can be for example the cost, or the parameter vector. It is meaningful to choose r comparatively large to reduce the effect of high-frequency changes.

This rate of change itself can already give an idea if the respective value stagnates. However, it still carries some noise with it. in order to minimize that, we can average the differential quotient over a couple of iterations. This is equivalent to taking the differential quotient of the averages, and a meaningful metric, defined as

$$\begin{aligned} R_{\mathrm{ADQ}} &= \frac{1}{n} \sum_{k=n-l}^{n} R_{\mathrm{DQ}}[k] = \frac{1}{n} \sum_{k=n-l}^{n} \frac{X[k] - X[k-r]}{r} \\ &= \frac{\frac{1}{n} \sum_{k_1=n-l}^{n} X[k_1] - \frac{1}{n} \sum_{k_2=n-l}^{n} X[k_2 - r]}{r}. \end{aligned} \tag{4.11}$$

For low values of $|R_{\mathrm{ADQ}}|$, it is justified to assume that the respective values orbit in around a nearly fixed mean. If this is the case for the cost function, it means that there is no long-term trend to a decrease in its value.

Value differences

While the differential quotient over many iterations can provide information about the long-term tendency of the respective value, it is also useful to know its high-frequency behavior. The differences of subsequent values can provide important information in this regard. It gives an idea of the amplitude for high frequency effects.

Differences sign changes

The frequency of short-term changes in the values is another useful metric. It is directly correlated to the frequency of sign changes of the value differences.

4.5.2 Reacting to different indicators

The presented metrics contain valuable information about the optimization progress. Depending on their values, we can make informed decisions about changes and adaptations of the process.

Low average differential quotient

As described earlier, a low value of the differential quotient indicates that no more meaningful long-term changes are to be expected. First of all, this indicates that the contraction area of a local minimum is reached. This is a good time to disable the potential field helping to avoid previously explored minima as presented in § 4.4.1 to ensure it is an actual minimum of the underlying scalar field. This can be done by simply setting $\theta = 0$.

If the repelling field of the previous minima has already been disengaged, we can have a look at the short-term behavior: If there are high-frequency effects with comparatively high amplitude, this indicates continuous overshoot. This can be tackled by reducing the step size ($\alpha \leftarrow a\alpha, 0 < a < 1$).

If there is no considerable high-frequency effects and the current cost is relatively high, we can conclude that we have reached a local minimum that is not the global minimum. in that case, we store the current set of parameters as local minimum coordinates and restart the optimization from new starting coordinates as explained in § 4.4.1.

High average differential quotient

If the step size is chosen too high, we might experience high-frequency changes in cost and parameters even without notably stagnating means. If this is the case, the step size needs to be reduced, as well.

Optimizer performance

The described optimization algorithm has been applied to the 4-dimensional implementation of the *Ackley* function as developed in [1], which, similar to the cost functions in this chapter, has many local minima and one global minimum with a considerably lower value. The function is defined as

$$C_{\text{ack}}(x) = -20 \exp\left(-0.2\sqrt{\frac{1}{4}\sum_{i=1}^{4} x_i^2}\right) - \exp\left(-0.2\sqrt{\frac{1}{4}\sum_{i=1}^{4} \cos 2\pi x_i}\right) + 20 + \exp(1) \tag{4.12}$$

The optimization domain has been chosen to $x_i \in [-32.76832.768)$. The algorithm's behavior is described in Fig. 4.1.

4.6 Experimental data

Experiments with the SAM are essential for the system identification process.

4.6.1 Experimental setup

The experiments have been conducted in a single pendulum configuration of the SAM, i.e. without any considerable mass placed between the suspension point and the platform. We collected ground truth data using the vision-based Vicon system (see [12] for performance analysis). The full setup is depicted in Fig. 4.3. Throughout this section, we will use V to denote the Vicon system's inertial frame which has been calibrated to have the z-axis point in the opposite direction of gravitational acceleration, I to denote an inertial frame whose origin is in the suspension point with the same orientation as V, L to denote the frame fixed to SAM which is observed by the Vicon system, and B to

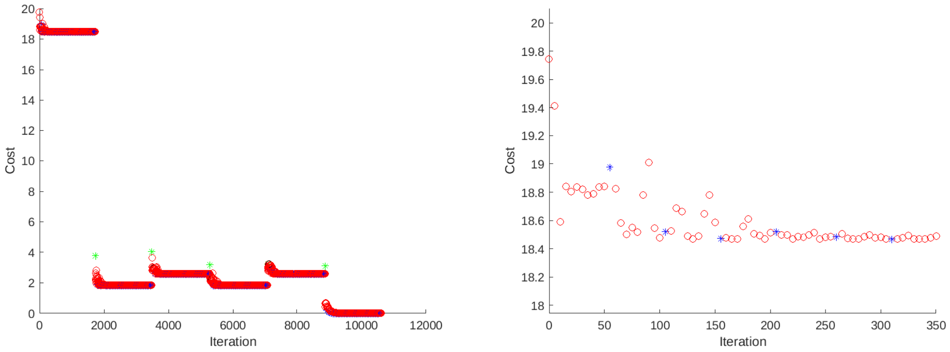

(a) Successful optimization

(b) Detailed view

Figure 4.1: The optimizer running on the Ackley function. In Fig. 4.1b, the first 350 iterations are shown in detail. The blue stars mark a reduction of the step size α, whereas the green stars mark the selection of a new parameter and a restart. In the first 50 iterations, jumps in the cost function take place that indicate overshoot in a larger scale. These jumps are detected and the step size is reduced. It can be seen that this improves the issue, but needs to be repeated multiple times. After 1735 iterations, the value does not decrease anymore, while the minimum step size has been reached. As a reaction, a restart is initiated. Finally, after finding 5 local minima, the optimization ends up at the global minimum at $(0,0,0,0)$ and terminates, because it satisfies the termination condition $C_{\text{ack}} < 1e - 6$.

denote the frame fixed to SAM with its origin in the CoM and with the z-axis pointing towards the suspension point in the resting state. The different coordinate frames are illustrated in Fig. 4.2.

Note that the Vicon system provides the transformations from L to V, ${}_{\mathrm{I}}g_{\mathrm{L}}$. We are generally more interested in the transformations from B to I, ${}_{\mathrm{I}}g_{\mathrm{B}}$, however, which we are going to extract in the subsequent steps.

4.6.2 Experiment formats

The data collected in the experiments is analyzed to find kinematic and dynamic parameters of SAM, which are an integral part of the observer.

To this end, multiple experiments with different target values have been conducted. The experimental data is then used as a ground truth to fit kinematic and dynamic parameters of the system to. All of the parameters are found through optimization (as described in this chapter) even if direct algebraic equations for individual datapoints are available. This is done to avoid overfitting to those individual points and to leverage the entire dataset available to average out high-frequency noise.

Passive swings

It was not possible to calibrate the Vicon system's inertial frame to the suspension point because it was not in the field of view.

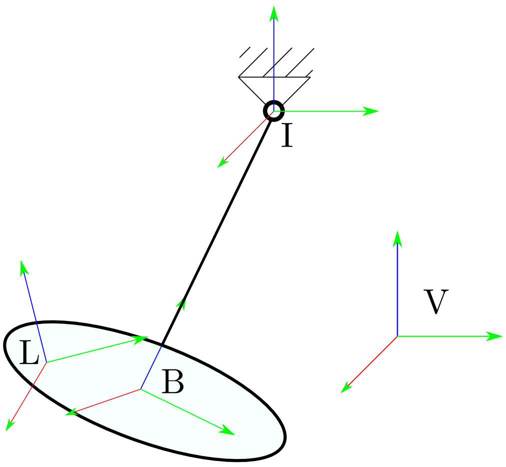

Figure 4.2: The different coordinate frames in the experimental setup: B and L are fixed to the platform, V and I are inertial.

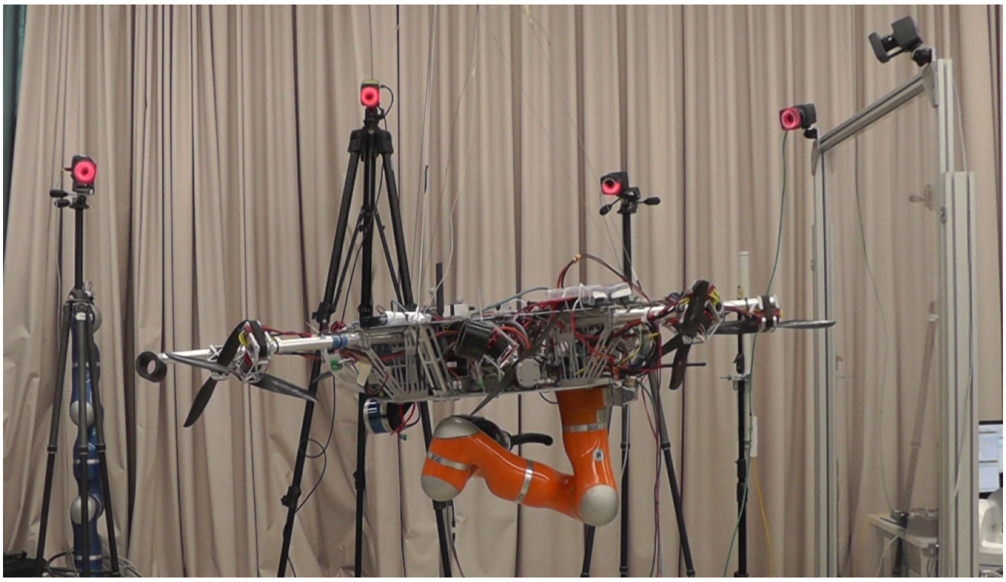

Figure 4.3: The experimental setup with the SAM swinging. At the top, the Vicon cameras can be seen.

In order to identify the suspension point's coordinates represented in the Vicon inertial frame, the platform has been excited manually to swing about its suspension point (see Fig. 4.4).

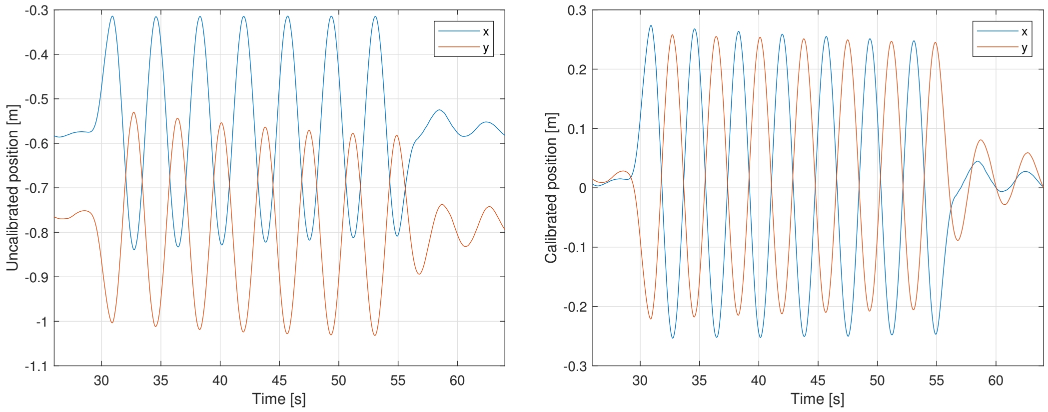

(a) Original data from the Vicon system

(b) Calibrated data

Figure 4.4: Passive swings of the SAM. The calibration has been chosen such that the swings' equilibrium point is exactly at 0.

Subsequently, the suspension point has been identified as the point whose distance to the body-fixed coordinate frame's origin varies the least. This is motivated by the assumption of the suspending cable's length being mostly constant throughout this experiment. The suspension point minimizes the cost function

$$C_{\mathrm{sus}} = var({}_{\mathrm{V}}P_{\mathrm{VI}} - {}_{\mathrm{V}}p_{\mathrm{VL}}), \tag{4.13}$$

where ${}_{\mathrm{V}}P_{\mathrm{VI}} = const.$ is the suspension point's coordinates in the V frame, and ${}_{\mathrm{V}}p_{\mathrm{VL}}$ denotes the L frame's origin's position in the V frame, which changes over time.

Using ${}_{\mathrm{V}}P_{\mathrm{VI}}$, we can easily find ${}_{\mathrm{I}}g_{\mathrm{L}}$ as

$${}_{\mathrm{I}}g_{\mathrm{V}} = \begin{bmatrix} I & -{}_{\mathrm{V}}P_{\mathrm{VI}} \\ 0 & 1 \end{bmatrix} \tag{4.14a}$$

$${}_{\mathrm{I}}g_{\mathrm{L}} = {}_{\mathrm{I}}g_{\mathrm{V}}\,{}_{\mathrm{V}}g_{\mathrm{L}}. \tag{4.14b}$$

We know that the equilibrium state of SAM requires its CoM to be exactly below its suspension point, although we don't know how far below. The oscillations of SAM will take place around this equilibrium, which indicates that the translation from L to B (${}_{\mathrm{L}}\tilde{g}_{\mathrm{B}} = const.$) minimizes

$$C_{\mathrm{CoMAx}} = \frac{1}{t_{\mathrm{e}}} \sum_{t=0}^{t_{\mathrm{e}}} \left\| \begin{bmatrix} 1 & 0 & 0 \\ 0 & 1 & 0 \\ 0 & 0 & 0 \end{bmatrix} \left({}_{\mathrm{I}}R_{\mathrm{L}}[t]\,{}_{\mathrm{L}}\tilde{r}_{\mathrm{B}} + {}_{\mathrm{I}}r_{\mathrm{IL}}[t]\right) \right\|_2^2 . \tag{4.15}$$

This cost function is just the average x and y coordinates of B in I, which we assume to be 0. Note that the assumption of the equilibrium point being exactly underneath the suspension point does not provide any information about its position along the B frame's z-axis, which leaves (4.15) invariable in this parameter. For this reason, we denote the transformation used here as ${}_{\mathrm{L}}\tilde{g}_{\mathrm{B}}$ instead of ${}_{\mathrm{L}}g_{\mathrm{B}}$.

In addition to the translation, ${}_{\mathrm{L}}g_{\mathrm{B}}$ might also contain a constant rotation. In order to find this rotation, we require the B frame's z-axis to point towards the suspension point. The resulting cost function to be minimized by ${}_{\mathrm{L}}\tilde{R}_{\mathrm{B}}$ is then

$$C_{\mathrm{BRot}} = \frac{1}{t_{\mathrm{e}}} \sum_{t=0}^{t_{\mathrm{e}}} \angle\left({}_{\mathrm{I}}z_{\mathrm{B}}, -{}_{\mathrm{I}}r_{\mathrm{IB}}\right) = \frac{1}{t_{\mathrm{e}}} \sum_{t=0}^{t_{\mathrm{e}}} \angle\left({}_{\mathrm{I}}R_{\mathrm{L}}[t]\,{}_{\mathrm{L}}\tilde{R}_{\mathrm{B}} \begin{bmatrix} 0 \\ 0 \\ 1 \end{bmatrix}, -{}_{\mathrm{I}}r_{\mathrm{IL}} - {}_{\mathrm{I}}R_{\mathrm{L}}[t]\,{}_{\mathrm{L}}r_{\mathrm{LB}} \right), \tag{4.16}$$

where ${}_{\mathrm{I}}z_{\mathrm{B}}$ denotes the B frame's z-axis, described in I, and ${}_{\mathrm{I}}r_{\mathrm{IB}}$ is the vector from I's origin to B's origin. We would like those to be parallel.

Again, this requirement leaves one degree of freedom for the rotation, which is around the B frame's z-axis. In total, with this step, we can find ${}_{\mathrm{L}}g_{\mathrm{B}}$ up to translation and rotation along the B frame's z-axis as

$$ {}_{\mathrm{L}}g_{\mathrm{B}} = {}_{\mathrm{L}}\tilde{g}_{\mathrm{B}} \begin{bmatrix} & 0 \\ R_z(\gamma) & 0 \\ & z_{\mathrm{CoM}} \\ 0 & 1 \end{bmatrix}. \tag{4.17}$$

Constant and sinusoidal unidirectional force

The second experiment used for system identification consisted of constant and sinusoidal actuation of the SAM with a force pointing in one known direction (see Fig. 4.5).

This experiment directly provides the missing parameters to fully define γ, which was missing in 4.17. The optimal γ minimizes the cost function

$$C_{\gamma} = \frac{1}{t_{\mathrm{e}}} \sum_{t=0}^{t_{\mathrm{e}}} {}_{\mathrm{I}}v_{\mathrm{rot}}^{\mathrm{T}}\,{}_{\mathrm{I}}z_{\mathrm{I}} = \frac{1}{t_{\mathrm{e}}} \sum_{t=0}^{t_{\mathrm{e}}} ({}_{\mathrm{I}}R_{\mathrm{L}}[t]\,{}_{\mathrm{L}}\tilde{R}_{\mathrm{B}} R_z(\gamma)\,{}_{\mathrm{B}}v_{\mathrm{rot}})^{\mathrm{T}} \begin{bmatrix} 0 \\ 0 \\ 1 \end{bmatrix}, \tag{4.18}$$

where $R_z(\gamma)$ denotes a rotation matrix representing a rotation around the z-axis, ${}_{\mathrm{B}}v_{\mathrm{rot}}$ is the motion's rotation axis, which we know in the B frame, and z_{I} is the z-axis of the I frame. The optimal value fitting the experimental data was $\gamma = 12$.

Complex dataset for dynamic parameters

One experiment has been performed which combines excitement of the system in multiple absolute directions. In order to achieve this, a sinusoidal excitement in a constant direction with respect to the body frame was enabled. Subsequently, the SAM's yaw was controlled to arbitrarily changing piecewise constant values. Overall, the exciting force's direction was constant with respect to the body frame, whereas the Newton-Euler equations held in the inertial frame. This led to movement of the SAM in all possible

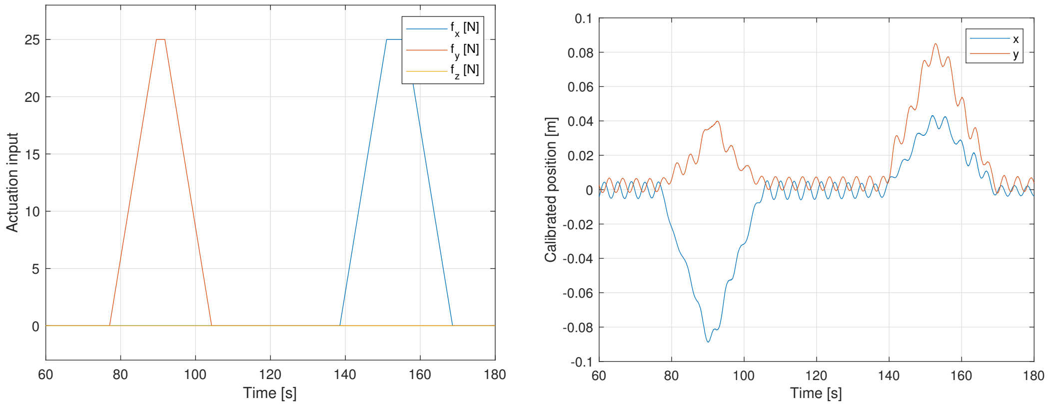

(a) Forces in the body frame (b) Position in the inertial frame

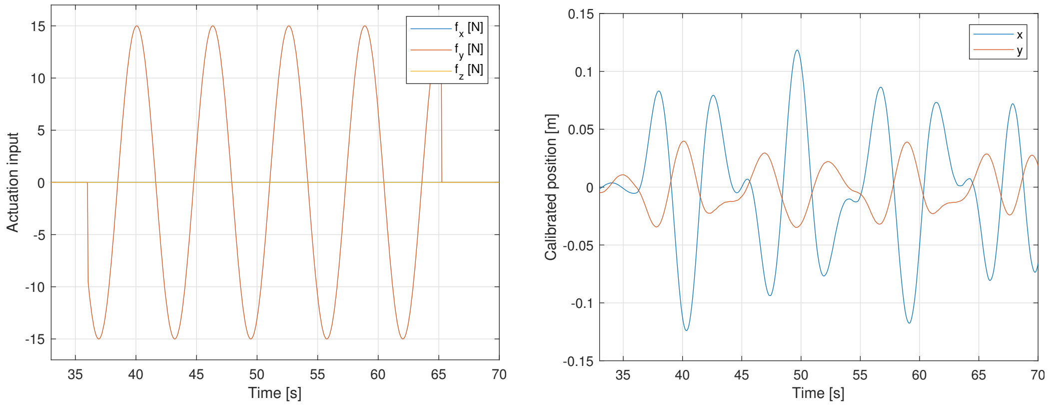

(c) Forces in the body frame (d) Position in the inertial frame

Figure 4.5: Active swings and holds of the SAM. It is clear that these experiments emphasize the relative orientation between the inertial and the body frame, as the input is given in the body frame, but the position readings are obtained in the inertial frame. In the experiments shown in the top row, a force has been slowly ramped up and down in one direction, whereas in the bottom row, a sinusoidal force was exerted.

directions. As a result, the data collected from this experiment should contain a lot of information about the system.

An optimization has been run on sets from all collected data to find the dynamic parameters of the system, along with the distance of the CoM from the suspension point, which finally completes ${}_{\mathrm{L}}g_{\mathrm{B}}$. The cost function used was the general one from (4.9). The parameters to optimize for were

$$W = \begin{bmatrix} m \\ \lambda_1 \Theta \\ \lambda_2 \Theta \\ \lambda_3 \Theta \\ \xi_\Theta \\ l \end{bmatrix}, \tag{4.19}$$

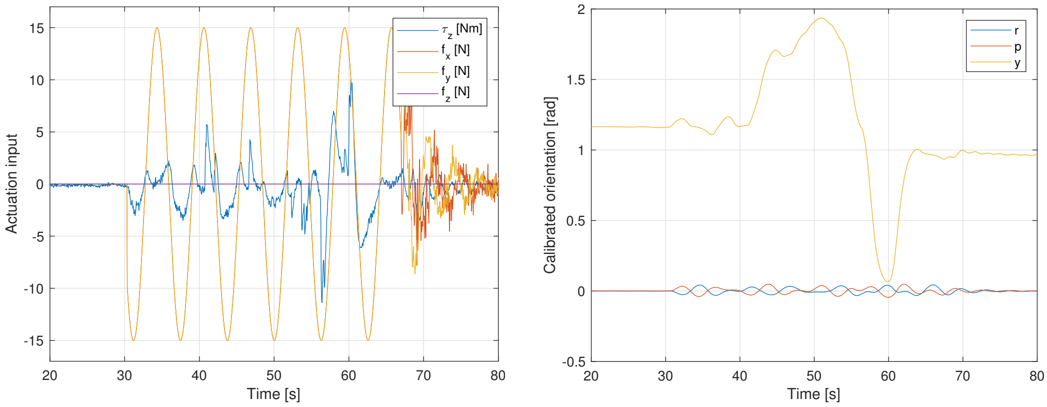

(a) Forces and torques in the body frame

(b) Orientation in the inertial frame

Figure 4.6: Sinusoidal force applied in changing absolute directions: In the body frame it's always in x-direction, the system's yaw however is being arbitrarily changed over time which changes the body z-axis' direction with it.

where the constraints on the inertia matrix Θ (it has to be symmetric and positive definite) have been respected implicitly, m is the SAM's mass and l denotes the distance of the CoM to the suspension point. We define only 6 relevant elements in W and then construct Θ from them as

$$R_\Theta = \exp((\xi_\Theta)^\wedge_\times) \tag{4.20a}$$

$$\Theta = R_\Theta^\mathrm{T} \begin{bmatrix} \lambda_1(\Theta) & 0 & 0 \\ 0 & \lambda_2(\Theta) & 0 \\ 0 & 0 & \lambda_3(\Theta) \end{bmatrix} R_\Theta . \tag{4.20b}$$

As shown in Fig. 4.7, the data collected in the experiments is unfortunately not conclusive for some of these values. In particular the mass moment of inertia of the system does not show a strong correlation to the cost function value. This can be explained by the very long arm of the pendulum with respect to the dimensions of the SAM itself. The equivalent mass moment of inertia around the suspension point (see (2.48)) is influenced mostly by the mass and the pendulum arm length at the values considered. Assuming $m = 55\,\mathrm{kg}$, $l = 3.5\,\mathrm{m}$ and $\lambda_{\max}(\Theta) = 25\,\mathrm{kgm}^2$, the body's inertia only makes up roughly $\frac{\lambda_{\max}(\Theta)}{ml^2+\lambda_{\max}(\Theta)} = 3.6\,\%$ of the equivalent mass moment of inertia.
This effect does not influence the mass moment of inertia around the body z-axis. However, most of the conducted experiments had a yaw controller enabled that inhibited any yaw motion. The exception is the dataset described in this section, which features some controlled, but arbitrary yaw maneuvers. These however are embedded in a set of very complex movement, so overall it makes up just a small part of the cost function and therefore is not prioritized in the optimization.

Although it is difficult to optimize the mass moment of inertia around the body z-axis on the entire dataset, we can still find estimates on it based on individual sections of the experiments. In particular, the yaw control introduces considerable angular acceleration.

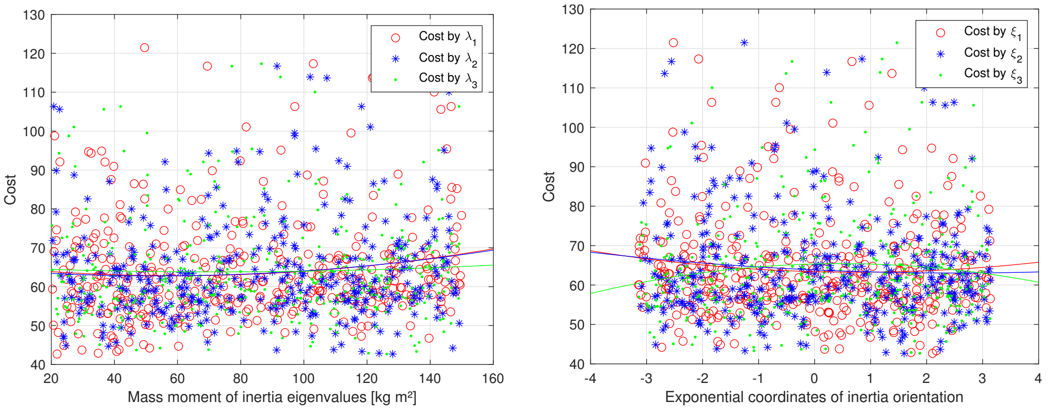

(a) Influence of the inertia eigenvalues. (b) Influence of the inertia orientation.

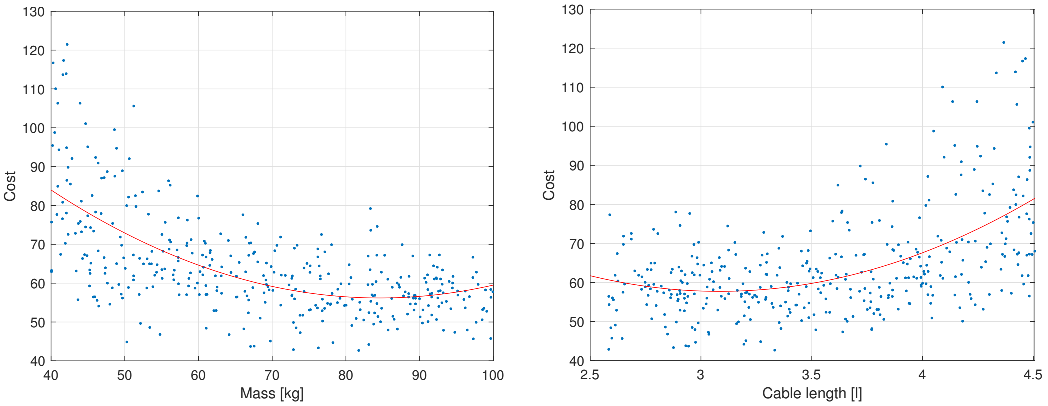

(c) Influence of the mass. (d) Influence of the cable length.

Figure 4.7: The correlation between model parameters and cost function values with respect to (4.2). Quadratic functions have been fit to the data. They don't show pronounced minima for the parameters of the mass moment of inertia: it can be concluded that those do not play a major role in the cost function, whereas the system mass and cable length each have a considerable influence.

Using data from different occasions where this takes place and applying it to (1.45), we obtain

$$\Theta_z = \frac{\tau}{\alpha} \tag{4.21}$$

as a relationship between the angular acceleration α, torque τ, and the mass moment of inertia around the z-axis, Θ_z. We can take the average of this value over a time where knowingly only τ causes α, in particular at the the times when the controller is turned on. In Fig. 4.8, the results of matching the angular acceleration to the input torque using Θ_z are shown. It shows that taking the numerical second derivative is quite noisy. However, the noise is rather comparatively frequent, and as such, taking the average over some time mostly cancels its effects. The resulting value is $\Theta_z = 14.33\,\mathrm{kgm}^2$. For reference, that is about the same as a homogeneous cylinder with a mass of 60 kg and a radius of 0.7 m.

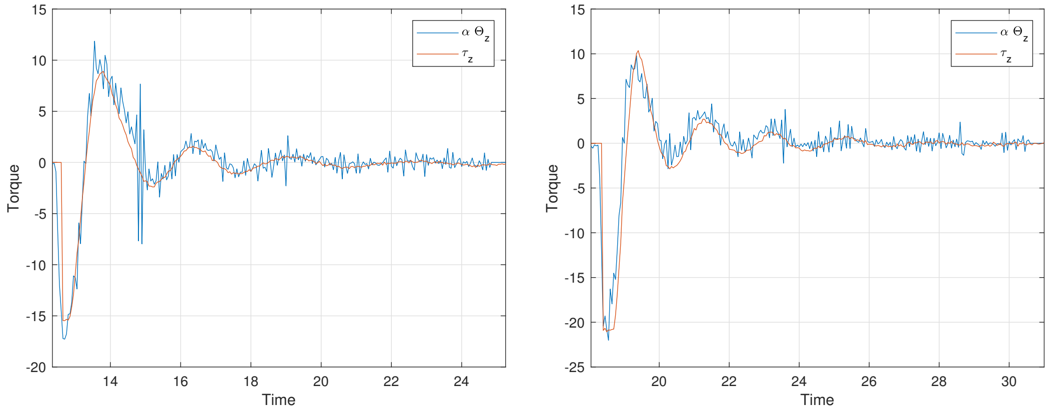

Figure 4.8: Two instances of the yaw controller being turned on and generating significant angular accelerations. Both sides of (1.45) are fit to match as closely as possible, despite noise resulting from numerical differentiation. Outliers are ignored.

Since we can't properly determine them using the optimization, we set $\xi_\Theta = 0$ and $\lambda_1(\Theta) = \lambda_2(\Theta) = 10\,\mathrm{kgm}^2$ as well as $\lambda_3(\Theta) = 14.33\,\mathrm{kg}$. The mass moment of inertia around the axes orthogonal to the z-axis have been chosen smaller than that around the z-axis, because the SAM's platform, which contains most of its mass, is comparatively flat. Overall, the optimization was thus reduced to two remaining parameters.

Dropping the system

Although the primary model assumed for the SAM is a rigid pendulum, we know that the cables from which it is suspended are not perfectly rigid, but actually compliant, with a stiffness k and a damping coefficient d.

A somewhat radical way to collect data that strongly depends on these values is to lift the system until its weight is no longer supported by its cables and then drop it to fall into the cables. This way, a trajectory (see Fig. 4.9)that heavily depends on those parameters can be generated, which in turn can be analyzed to obtain information about the compliance.

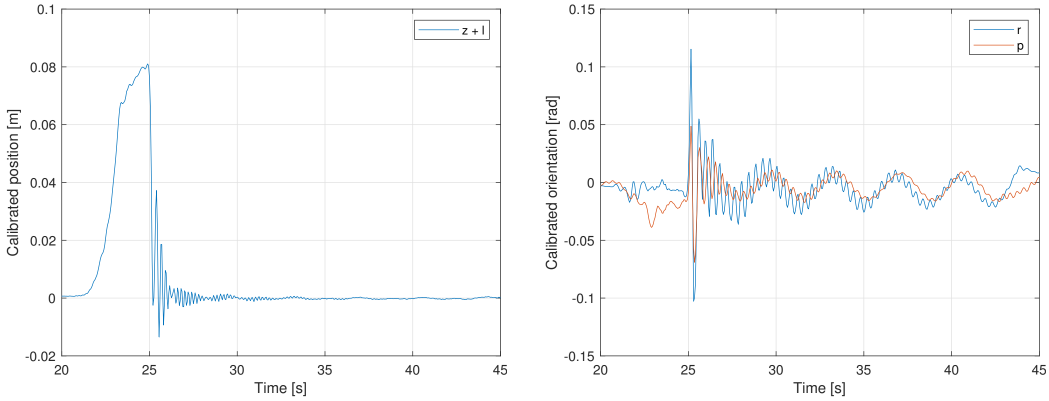

Figure 4.9: The response of the SAM to dropping into the cables.

Using the dynamics parameters obtained from earlier optimizations, we can optimize purely for the damping and stiffness properties of the SAM. The cost function used was the general one from (4.9). The simulation parameters to optimize for were

$$W = \begin{bmatrix} k_\mathrm{t} \\ k_\mathrm{r} \\ d_\mathrm{t} \\ d_\mathrm{r} \end{bmatrix} . \tag{4.22}$$

Here, k_t and k_r are the translational and rotational stiffnesses, and d_t and d_r the respective damping gains. The model to be optimized was § 3.3, with $K = \mathrm{blkdiag}(k_\mathrm{r} I_3, k_\mathrm{t} I_3)$ and $D = \mathrm{blkdiag}(d_\mathrm{r} I_3, d_\mathrm{t} I_3)$. The rotational and translational gains have been assumed to be multiples of the identity, respectively, as a reasonable simplification that significantly aids the optimization.

4.6.3 Optimization results

The remaining two parameters of the rigid model were determined to $m = 79.075\,\mathrm{kg}$ and $l = 3.4832\,\mathrm{m}$. It is very likely that the optimal mass for the model is not the true mass of the SAM, as that is assumed to be lower. Nevertheless, it best represented the collected data, so it is to be expected that it will also perform optimally in the observer. In this instance, absolute accuracy of the value is not the main priority.

The obtained distance between the suspension point and the CoM of the SAM seems to be very realistic.

While most experiments could be closely reproduced by the simulations (see Figs. 4.10 to 4.12), the inputs from § 4.6.2 directly exploit a weakness of the approach. Overall, the simulations could be considered a feedforward-only observer, as they do receive the wrenches applied to the real system, but not any of the state values. As such, they are naturally prone too suffer from drift. In most of the experiments, that drift could never grow to large, because gravity would always pull the system back towards the equilibrium, and the yaw control fixed the yaw angle. In the optimization, the yaw controller's torque was disregarded because so were the disturbances causing the yaw controller to engage in the first place. In the mentioned experiments however, the yaw torque plays a major role and as such can not be ignored. These torques, in combination with a potentially inaccurate value for Θ_z, are directed in a fully unconstrained direction with no potential field gradient along it, which means there is no inherent equilibrium the state would converge to. As a result, the error could grow unboundedly, and as a consequence, the simulations could not reproduce these experiments accurately (see Fig. 4.13). For this reason, their respective data will not be considered in the model comparison.

For the compliant model, the identified values are $k_\mathrm{t} = 54\,589\,\mathrm{N/m}$, $k_\mathrm{r} = 1903\,\mathrm{N\,m/rad}$, $d_\mathrm{t} = 435.9\,\mathrm{N\,s/m}$, $d_\mathrm{r} = 69.3\,\mathrm{N\,m\,s/rad}$. The reconstructed trajectory for the drop experiments is shown in Fig. 4.14.

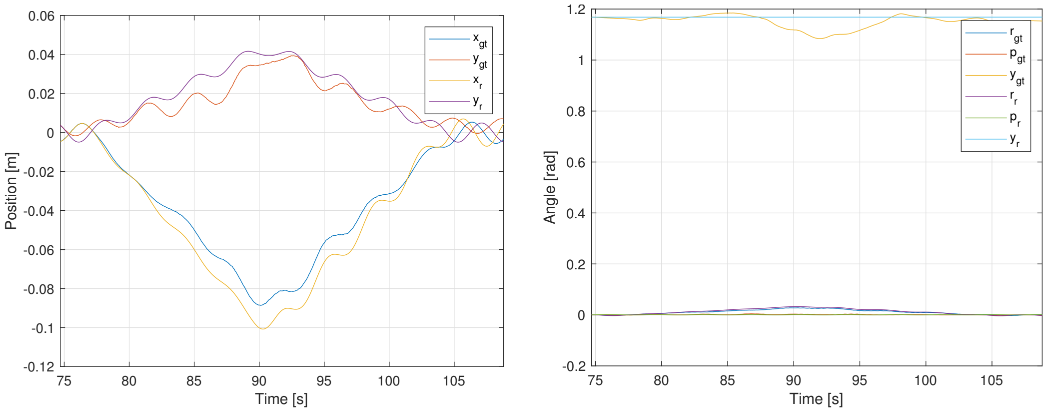

(a) Reproducing the position

(b) Reproducing the orientation

Figure 4.10: Reproducing the experiments featuring constant forces. In Fig. 4.10b, it is clear that the yaw angle was changing in the real data, but the simulation modeled no cause for any rotation around the body z-axis. It is remarkable that even 30 seconds after the most recent measurement, the simulated position is within a few centimeters of the experimentally generated trajectory.

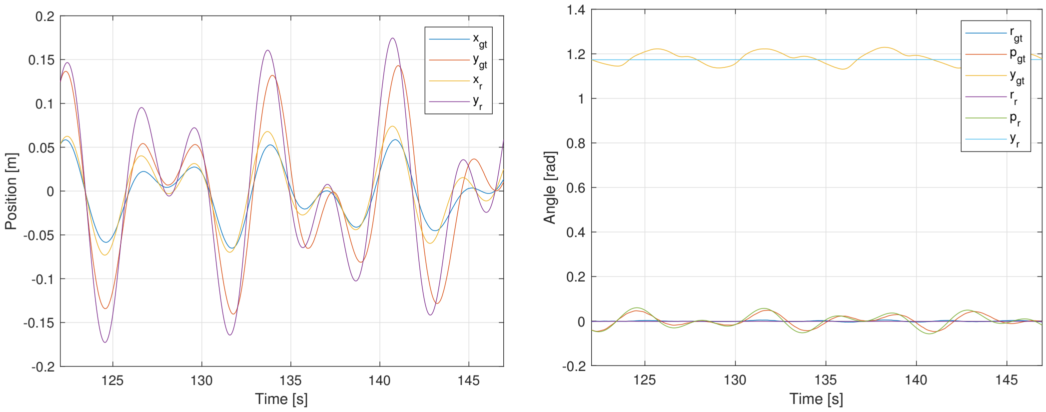

(a) Reproducing the position

(b) Reproducing the orientation

Figure 4.11: Reproducing the experiments featuring sinusoidal forces. Again, in Fig. 4.11b, it is clear that the yaw angle was changing in the real data, but the simulation modeled no cause for any movement around the body z-axis.

4.6.4 Model comparison

After all the parameters had been obtained, we compared the different models on how well they could reconstruct the individual experiments.

We only compare the single mass models here, as those respecting an intermediary mass would not be meaningful with regards to the experimental setup.

A comparison of remaining cost function values (according to (4.2)) for the two models is given in § 4.6.4. Here, it is noteworthy that the cost for the varying forces experiment is especially high, as previously explained. Apart from that, the values are similar with the exception of the dropping experiment. In Fig. 4.15, a typical trajectory of the difference

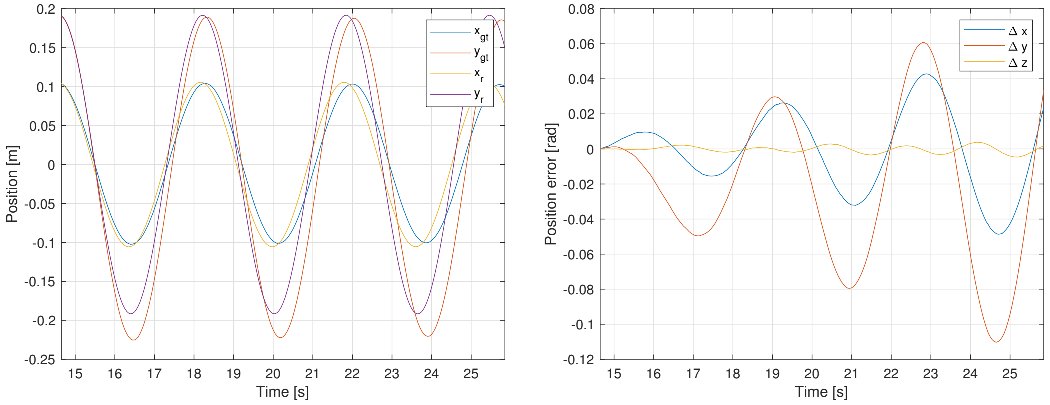

(a) Reproducing the position (b) Error in reproduced position

Figure 4.12: The simulated model seems to have a slightly higher natural frequency than the real data. This leads to a harmonic amplitude change of the position error, but no unbounded drift, because the system and the simulation will always move around the same equilibrium. It should be noted that this is an indicator that the distance between the suspension point and the CoM has been chosen too long. However, this value best fits the data and therefore might still be better suited to be used.

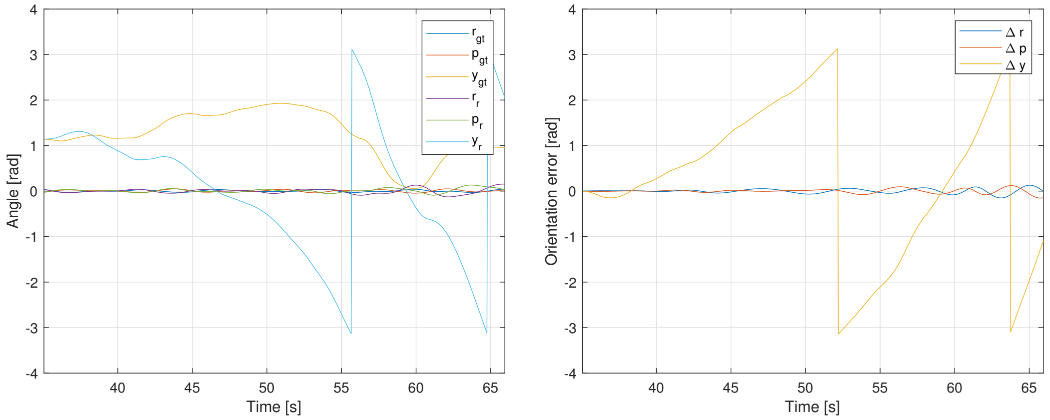

(a) Reproducing the orientation (b) Orientation error

Figure 4.13: Drift in the yaw angle accumulates quickly enough to soon render the simulated values entirely meaningless.

between the models in the first seconds is shown. However, the cost values of both models are particularly high on this experiment, meaning that neither can accurately represent it.

Overall, the rigid pendulum model performed well at reproducing the results from the experiments. In everyday operation, the SAM is unlikely to violate the rigid pendulum assumption as extremely as in the drop experiments. As such, it is a reasonable choice to model the SAM accurately without the need for an unnecessarily complex model.

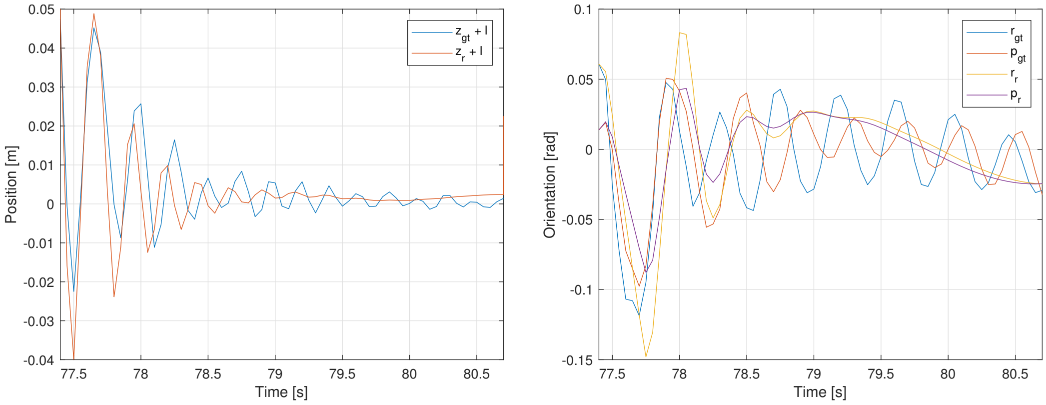

(a) Reproducing the position (b) Reproducing the orientation

Figure 4.14: The reconstructed trajectory of the drop experiments. It is clear that the reconstruction is not perfect. This indicates that the model is not fully representative of the real system. For instance, the oscillation frequency does not decrease exponentially in the real system, which is particularly significant for the orientation. As such, the parameters can't perfectly fit the entire timeseries. Instead, the beginning is focused because it features higher variations, which are especially expensive in the quadratic cost function. In addition to that, the measurement frequency of 20 Hz of the Vicon system might be too low to detailedly capture these high frequency oscillations.

Table 4.1: Evaluation of the two models

Experiment	Rigid pendulum cost	Compliant pendulum cost
Passive Swings	0.0034	0.0045
Constant Force	0.0064	0.0063
Sinusoidal Force	0.0027	0.0024
Dropping the SAM	0.0370	0.0222
(Varying forces (§ 4.6.2)	2.8758	2.8409)

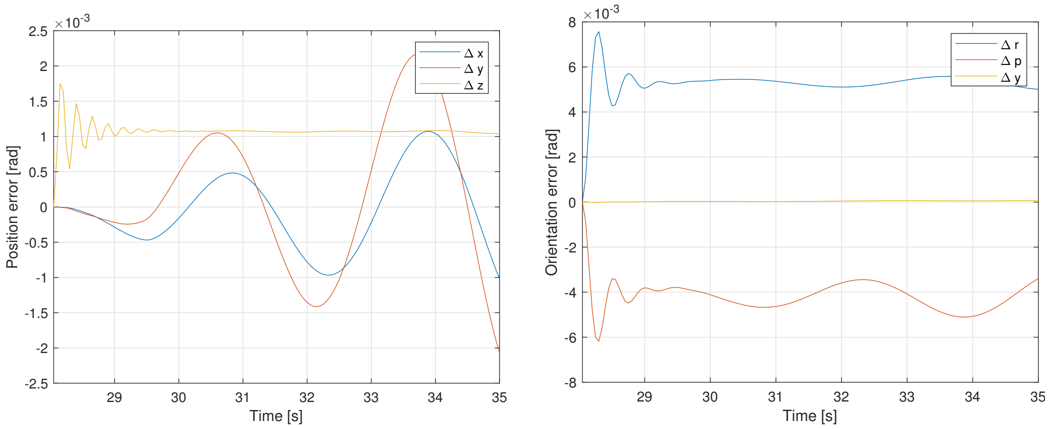

(a) Position difference

(b) Orientation difference

Figure 4.15: The difference between both models starts with the compliant model converging to its equilibrium with respect to the soft constraints. This happens because in the experimental data, slight variances with respect to the pendulum constraints‘ occur, such that the initial conditions are not guaranteed to be at the compliant model's equilibrium. Overall, the difference is considerably lower than that of the individual models to the experimental data.

Chapter 5

Observer Design

Notation

In this chapter, we will denote values that correspond to an observer with the same symbols used for the respective values in the observed system, but adding a hat $\hat{\ }$. For example, V is the twist of the real (observed) system, while $\hat{V}$ denotes the twist of the observer.

In particular, B denotes the body frame of the observed system, whereas $\hat{B}$ is the body frame of the observer. It is important to consider which frame the values are represented in in order to ensure that all values of an expression are compatible and the result is meaningful.

In addition to that, V and g denote the *system state* as introduced in § 1.3.4, not necessarily that of just one rigid body.

5.1 A nonlinear observer for free-floating rigid bodies

In [13], an observer is proposed which estimates position and velocity of free-floating rigid bodies, on which this work is mainly based. In this section, we will sketch its working principles.

5.1.1 Observed system

We assume that the pose of the body to be observed satisfies

$$\dot{g} = g \cdot [{}_{\mathrm{B}}V]^{\wedge}\,, \tag{5.1}$$

which defines ${}_{\mathrm{B}}V$ as the body velocity as described in (1.27).

The system's dynamics are

$$\frac{d}{dt}\Lambda\,{}_{\mathrm{B}}V - \mathrm{ad}^{\mathrm{T}}_{{}_{\mathrm{B}}V}\Lambda\,{}_{\mathrm{B}}V = 0 \tag{5.2a}$$

$$\dot{V}^{\mathrm{b}} = \Lambda^{-1}\mathrm{ad}^{\mathrm{T}}_{{}_{\mathrm{B}}V}\Lambda\,{}_{\mathrm{B}}V\,, \tag{5.2b}$$

the dynamics of a rigid body as described in (1.50) with no wrench acting on it. This is reasonable because the observer is designed for free-floating bodies, which are assumed to not have any external wrenches acting on them.

5.1.2 Errors

The approach assumes infrequent measurements of the true pose g. To bridge the time when no measurements are available, it continuously propagates the estimated pose $\hat{g}$. Of course, this propagated pose might deviate from the true pose of the system.

We call the difference between the estimated and the true pose η and define it as

$$\eta = \hat{g}^{-1} g = {}_{\hat{\mathrm{B}}}\eta_{\mathrm{B}}\,. \tag{5.3}$$

Whenever no new measurements are available, the state propagation without measurements is realized by setting $\eta = I$.

η maps from the observed system's body frame to the estimated body frame. We define $\varepsilon = [\log(\eta)]^{\vee}$ as a vector representation of the pose error. This is useful, as it resides in $\mathbb{R}^6 \cong \mathfrak{se}(3)$ instead of SE(3).

Similarly to the pose error, we also define a velocity error

$${}_{\mathrm{B}}V_{\mathrm{e}} = {}_{\mathrm{B}}V - \mathrm{Ad}_{\eta^{-1}}{}_{\hat{\mathrm{B}}}\hat{V}. \tag{5.4}$$

The transformation adjoint into the true pose's frame is applied to the estimated velocity to enable a meaningful comparison of both velocities in the same frame.

5.1.3 Observer

The observer follows equations of motion similar to those of the observed system itself in order to be able to accurately predict its motion while no measurements are available.

The estimated pose's time derivative is chosen to

$$\dot{\hat{g}} = \hat{g}[{}_{\hat{\mathrm{B}}}\hat{V} + \mathrm{Ad}_{\eta} K \varepsilon]^{\wedge}, \tag{5.5}$$

where, apart from the expected body velocity, an additional term depending on the pose error is included. This term drives convergence when measurements are available, parameterized by a constant gain K. It is clear that while no measurements are available (i.e. $\eta = I$), the kinematics reduce to the exact same form of (5.1), which makes it suitable for propagating the state while no measurements are available.

The observer dynamics are defined in the true pose's frame, i. e. the dynamics of ${}_{\mathrm{B}}\hat{V} = \mathrm{Ad}_{\eta^{-1}}{}_{\hat{\mathrm{B}}}\hat{V}$ rather than those of ${}_{\hat{\mathrm{B}}}\hat{V}$ are described. This is reasonable as it results in Λ being constant. Taking the time derivative of this transformed body velocity however generates a term in ${}_{\mathrm{B}}V_{\eta}$, which can not be derived from pure pose measurements. For that reason, the term is disregarded for the observer dynamics by choosing

$$\frac{d}{dt}\Lambda \mathrm{Ad}_{\eta^{-1}}{}_{\hat{\mathrm{B}}}\hat{V} - \mathrm{ad}^{\mathrm{T}}_{\mathrm{Ad}_{\eta^{-1}}{}_{\hat{\mathrm{B}}}\hat{V}} \Lambda \mathrm{Ad}_{\eta^{-1}}{}_{\hat{\mathrm{B}}}\hat{V} = -\mathrm{ad}_{{}_{\mathrm{B}}V_{\eta}} \mathrm{Ad}_{\eta^{-1}}{}_{\hat{\mathrm{B}}}\hat{V} + {}_{\mathrm{B}}f_{\mathrm{obs}} \tag{5.6a}$$

$$\dot{\hat{V}}^{\hat{\mathrm{b}}} = \mathrm{Ad}_{\eta}\Lambda^{-1}(\mathrm{ad}^{\mathrm{T}}_{\mathrm{Ad}_{\eta^{-1}}{}_{\hat{\mathrm{B}}}\hat{V}} \Lambda \mathrm{Ad}_{\eta^{-1}}{}_{\hat{\mathrm{B}}}\hat{V} + {}_{\mathrm{B}}f_{\mathrm{obs}}). \tag{5.6b}$$

It is clear that both the observer and the system to be observed have a very similar structure of their respective dynamics. In addition to that, their respective accelerations are both formulated in the true body frame.

5.1.4 Error dynamics

Plugging (5.1) and (5.5) into the derivative of (5.3), we can compute the pose error's time derivative as

$$\dot{\eta} = \eta({}_{\mathrm{B}}V - \mathrm{Ad}_{\eta^{-1}}\,{}_{\hat{\mathrm{B}}}\hat{V} - K\varepsilon) = \eta V_{\eta}, \tag{5.7}$$

where we define V_{η} as a body velocity-like value for the pose error η.

To help with the stability analysis, in [13], a helpful function $C({}_{\mathrm{B}}V_{\mathrm{e}}, {}_{\mathrm{B}}V)$ with the important skew-symmetric property $\langle {}_{\mathrm{B}}V_{\mathrm{e}}, C({}_{\mathrm{B}}V_{\mathrm{e}}, {}_{\mathrm{B}}V){}_{\mathrm{B}}V_{\mathrm{e}}\rangle = 0$ is defined as

$$\begin{aligned} &C({}_{\mathrm{B}}V_{\mathrm{e}}, {}_{\mathrm{B}}V){}_{\mathrm{B}}V_{\mathrm{e}} \\ &= \mathrm{ad}^{\mathrm{T}}_{{}_{\mathrm{B}}V}\Lambda{}_{\mathrm{B}}V - \mathrm{ad}^{\mathrm{T}}_{({}_{\mathrm{B}}V - {}_{\mathrm{B}}V_{\mathrm{e}})}\Lambda({}_{\mathrm{B}}V - {}_{\mathrm{B}}V_{\mathrm{e}}) - \Lambda\mathrm{ad}_{{}_{\mathrm{B}}V}{}_{\mathrm{B}}V_{\mathrm{e}}. \end{aligned} \tag{5.8}$$

Next, the time derivative of the velocity error can be obtained as

$$\dot{V}^{\mathrm{b}}_{\mathrm{e}} = \dot{V}^{\mathrm{b}} - \mathrm{Ad}_{\eta^{-1}}\dot{\hat{V}}^{\mathrm{b}} + \mathrm{ad}_{{}_{\mathrm{B}}V_{\eta}}\mathrm{Ad}_{\eta^{-1}}\,{}_{\hat{\mathrm{B}}}\hat{V} \tag{5.9a}$$

$$\dot{V}^{\mathrm{b}}_{\mathrm{e}} = \dot{V}^{\mathrm{b}} - \mathrm{Ad}_{\eta^{-1}}\dot{\hat{V}}^{\mathrm{b}} - \mathrm{ad}_{{}_{\mathrm{B}}V}{}_{\mathrm{B}}V_{\mathrm{e}} - \mathrm{ad}_{K\varepsilon}\mathrm{Ad}_{\eta^{-1}}\,{}_{\hat{\mathrm{B}}}\hat{V}. \tag{5.9b}$$

Plugging (5.2b) and (5.6b) into (5.9b), we obtain

$$\begin{aligned} \dot{V}^{\mathrm{b}}_{\mathrm{e}} &= \Lambda^{-1}(\mathrm{ad}^{\mathrm{T}}_{{}_{\mathrm{B}}V}\Lambda{}_{\mathrm{B}}V) - \mathrm{Ad}_{\eta^{-1}}\mathrm{Ad}_{\eta}\Lambda^{-1}({}_{\mathrm{B}}f_{\mathrm{obs}} + \mathrm{ad}^{\mathrm{T}}_{\mathrm{Ad}_{\eta^{-1}}\,{}_{\hat{\mathrm{B}}}\hat{V}}\Lambda\mathrm{Ad}_{\eta^{-1}}\,{}_{\hat{\mathrm{B}}}\hat{V}) \\ &-\mathrm{ad}_{{}_{\mathrm{B}}V}{}_{\mathrm{B}}V_{\mathrm{e}} - \mathrm{ad}_{K\varepsilon}\mathrm{Ad}_{\eta^{-1}}\,{}_{\hat{\mathrm{B}}}\hat{V}. \end{aligned} \tag{5.10}$$

Using (5.8), we can simplify (5.10) to

$$\dot{V}^{\mathrm{b}}_{\mathrm{e}} = \Lambda^{-1}(-{}_{\mathrm{B}}f_{\mathrm{obs}} + C({}_{\mathrm{B}}V_{\mathrm{e}}, {}_{\mathrm{B}}V){}_{\mathrm{B}}V_{\mathrm{e}}) - \mathrm{ad}_{K\varepsilon}\mathrm{Ad}_{\eta^{-1}}\,{}_{\hat{\mathrm{B}}}\hat{V}. \tag{5.11}$$

The observer wrench is chosen to ${}_{\mathrm{B}}f_{\mathrm{obs}} = -\Lambda\mathrm{ad}_{K\varepsilon}\mathrm{Ad}_{\eta^{-1}}\,{}_{\hat{\mathrm{B}}}\hat{V} + f_0$. This results in the compact error dynamics

$$\dot{V}^{\mathrm{b}}_{\mathrm{e}} = \Lambda^{-1}(-f_0 + C({}_{\mathrm{B}}V_{\mathrm{e}}, {}_{\mathrm{B}}V){}_{\mathrm{B}}V_{\mathrm{e}}). \tag{5.12}$$

5.1.5 Stability analysis

For the stability analysis, the dynamics of $e = [\varepsilon^{\mathrm{T}}, (V^{\mathrm{b}}_{\mathrm{e}})^{\mathrm{T}}]^{\mathrm{T}}$ are considered. The analysis can be found in more detail in [13].

As described in (1.33), the time derivative of ε can be determined to

$$\dot{\varepsilon} = \mathrm{B}_{\mathrm{r}}(\varepsilon)V_{\eta} = \mathrm{B}_{\mathrm{r}}(\varepsilon){}_{\mathrm{B}}V_{\mathrm{e}} - K\varepsilon. \tag{5.13}$$

The Lyapunov candidate function is

$$W = \frac{1}{2}e^{\mathrm{T}}Pe, \tag{5.14}$$

with

$$P = \begin{bmatrix} P_1 & 0 \\ 0 & P_2\Lambda \end{bmatrix} = P^{\mathrm{T}}. \tag{5.15}$$

$P_1 = p_1 I$ and $P_2 = \text{blkdiag}[p_{21} I_3, p_{22} I_3]$ are both chosen positive definite, so W is a positive definite function.

Then the derivative of the candidate function is

$$\begin{aligned}\dot{W} &= e^{\mathrm{T}} P \dot{e}\\ &= \varepsilon^{\mathrm{T}} P_1 (\mathrm{B_r}(\varepsilon) {}_{\mathrm{B}}V_{\mathrm{e}} - k\varepsilon) + ({}_{\mathrm{B}}V_{\mathrm{e}})^{\mathrm{T}} P_2 (-f_0 + C({}_{\mathrm{B}}V_{\mathrm{e}}, {}_{\mathrm{B}}V) {}_{\mathrm{B}}V_{\mathrm{e}})\\ &= -kp_1 ||\varepsilon||^2 + \varepsilon^{\mathrm{T}} P_1 \mathrm{B_r}(\varepsilon) V_{\mathrm{e}}^{\mathrm{b}} - ({}_{\mathrm{B}}V_{\mathrm{e}})^{\mathrm{T}} P_2 f_0.\end{aligned} \tag{5.16}$$

By choosing $f_0 = P_2^{-1} \mathrm{B_r^T}(\varepsilon) P_1 \varepsilon$, the derivative becomes

$$\dot{W} = -kp_1 ||\varepsilon||^2 \leq 0. \tag{5.17}$$

LaSalle's invariance principle

The time derivative of the Lyapunov function is negative if and only if $\varepsilon \neq 0$. In order to apply LaSalle's invariance principle, we analyze the trajectories in the subspace where $\varepsilon = 0$ and show that there are no closed trajectories in this subspace outside of the equilibrium ($e = 0$). This subspace can be defined as $\mathcal{I} = \{\varepsilon \in \mathbb{R}^6 \cong \mathfrak{se}(3), V_{\mathrm{e}}^{\mathrm{b}} \in \mathbb{R}^6 | \varepsilon = 0, V_{\mathrm{e}}^{\mathrm{b}} \neq 0\}$.

For any point in $\mathcal{I}$, (5.13) will evaluate to $\dot{\varepsilon} = V_{\mathrm{e}}^{\mathrm{b}} \neq 0$. This in turn will unavoidably lead to $\varepsilon \neq 0$ immediately after which does not correspond to a point in $\mathcal{I}$. This implies that any trajectory passing through a point in $\mathcal{I}$ will leave $\mathcal{I}$ immediately again.

As a result, there are no closed trajectories in $\mathcal{I}$. That means that the only closed trajectory satisfying $\dot{V}$ is $e(t) = 0, \forall t \geq 0$. We can conclude that the equilibrium $e = 0$ is asymptotically stable.

An important remark is that the convergence radius is limited by the representation of the orientations, which is discussed in more detail in [13].

5.2 Extending the observer based on pose measurements

A lot of physical systems can not be described as a free floating body or a collection thereof. Many of them consist of bodies that are constrained or have known wrenches acting on them. Here, the presented observer will be extended to also apply to those, more general, systems.

5.2.1 Adding constraints and known wrenches

In order to add the constraints while preserving the structure of the observer, an approach featuring explicitly computed constraint wrenches f_{c} (as presented in § 2.2.1) will be applied. In addition to that, we consider known wrenches acting on the system f_{in}. The updated system dynamics are

$$\frac{d}{dt} \Lambda {}_{\mathrm{B}}V - \mathrm{ad}^*_{{}_{\mathrm{B}}V} \Lambda {}_{\mathrm{B}}V = f_{\mathrm{c}} + f_{\mathrm{in}} \tag{5.18a}$$

$$\dot{V}^{\mathrm{b}} = \Lambda^{-1} (f_{\mathrm{c}} + f_{\mathrm{in}} + \mathrm{ad}^*_{{}_{\mathrm{B}}V} \Lambda {}_{\mathrm{B}}V), \tag{5.18b}$$

where f_c ensures a constraint of the form $A(g)_\mathrm{B}V = 0$.

We can straightforwardly extend the observer dynamics accordingly to

$$\frac{d}{dt}\Lambda\mathrm{Ad}_{\eta^{-1}}{}_{\hat{\mathrm{B}}}\hat{V} - \mathrm{ad}^\mathrm{T}_{\mathrm{Ad}_{\eta^{-1}}{}_{\hat{\mathrm{B}}}\hat{V}}\Lambda\mathrm{Ad}_{\eta^{-1}}{}_{\hat{\mathrm{B}}}\hat{V} = {}_\mathrm{B}f_\mathrm{obs} + {}_\mathrm{B}\hat{f}_\mathrm{c} - \mathrm{ad}_{\mathrm{B}V_\eta}\mathrm{Ad}_{\eta^{-1}}{}_{\hat{\mathrm{B}}}\hat{V} \tag{5.19a}$$

$$_{\hat{\mathrm{B}}}\dot{\hat{V}} = \mathrm{Ad}_\eta\Lambda^{-1}({}_\mathrm{B}f_\mathrm{obs} + {}_\mathrm{B}\hat{f}_\mathrm{c} + \mathrm{ad}^\mathrm{T}_{\mathrm{Ad}_{\eta^{-1}}{}_{\hat{\mathrm{B}}}\hat{V}}\Lambda\mathrm{Ad}_{\eta^{-1}}{}_{\hat{\mathrm{B}}}\hat{V}). \tag{5.19b}$$

This way, we aim to impose $\hat{A}_{\hat{\mathrm{B}}}\hat{V} = 0$. In order to retain high similarity to the observed system, we choose $\hat{A} = A(\hat{g})$.

The observer dynamics are derived in the true pose's frame B, so we can't directly apply (2.25) to obtain the constraint wrench. In addition to that, we require passivity of the constraint wrench. However, here, ${}_\mathrm{B}\hat{f}_\mathrm{c}$ and ${}_{\hat{\mathrm{B}}}\hat{V}$ are *not* power conjugated, because they belong to different frames. We need to transform either of them into the other's frame, yielding

$$_\mathrm{B}\hat{f}_\mathrm{c}^\mathrm{T}{}_\mathrm{B}\hat{V} = {}_\mathrm{B}\hat{f}_\mathrm{c}^\mathrm{T}\mathrm{Ad}_{\eta^{-1}}{}_{\hat{\mathrm{B}}}\hat{V} = {}_{\hat{\mathrm{B}}}\hat{f}_\mathrm{c}^\mathrm{T}{}_{\hat{\mathrm{B}}}\hat{V} = 0. \tag{5.20}$$

This motivates

$$_\mathrm{B}\hat{f}_\mathrm{c} = \mathrm{Ad}^\mathrm{T}_\eta{}_{\hat{\mathrm{B}}}\hat{f}_\mathrm{c}^\mathrm{T} = \mathrm{Ad}^\mathrm{T}_\eta\hat{A}^\mathrm{T}\hat{\lambda}_\mathrm{c}. \tag{5.21}$$

Next, we apply the same approach described in § 2.2.1: differentiation of the constraint equation and solving for λ_c. With this, we find

$$\frac{d}{dt}\hat{A}_{\hat{\mathrm{B}}}\hat{V} = \dot{\hat{A}}_{\hat{\mathrm{B}}}\hat{V} + \hat{A}\mathrm{Ad}_\eta\Lambda^{-1}({}_\mathrm{B}f_\mathrm{obs} + \mathrm{Ad}^\mathrm{T}_\eta\hat{A}^\mathrm{T}\hat{\lambda}_\mathrm{c} + \mathrm{ad}^*_{\mathrm{Ad}_{\eta^{-1}}{}_{\hat{\mathrm{B}}}\hat{V}}\Lambda\mathrm{Ad}_{\eta^{-1}}{}_{\hat{\mathrm{B}}}\hat{V}) = 0 \tag{5.22a}$$

$$\hat{\lambda}_\mathrm{c} = (\hat{A}\mathrm{Ad}_\eta\Lambda^{-1}\mathrm{Ad}^\mathrm{T}_\eta\hat{A}^\mathrm{T})^{-1}(\hat{A}\mathrm{Ad}_\eta\Lambda^{-1}(-{}_\mathrm{B}f_\mathrm{obs} - \mathrm{ad}^*_{\mathrm{Ad}_{\eta^{-1}}{}_{\hat{\mathrm{B}}}\hat{V}}\Lambda\mathrm{Ad}_{\eta^{-1}}{}_{\hat{\mathrm{B}}}\hat{V}) - \dot{\hat{A}}_{\hat{\mathrm{B}}}\hat{V}). \tag{5.22b}$$

Finally, in order to respect the known input wrenches, we simply consider them in

$$_\mathrm{B}f_\mathrm{obs} = f_\mathrm{in} - \Lambda\mathrm{ad}_{K\varepsilon}\mathrm{Ad}_{\eta^{-1}}{}_{\hat{\mathrm{B}}}\hat{V} + f_0. \tag{5.23}$$

5.2.2 Stability and convergence

The approach shows promising performance in both simulations and experiments (see § 5.5 and § 5.6). However, it is difficult to find a Lyapunov function to prove its convergence and the stability of the origin. For this reason, a numerical validation approach for a wide range of parameters is taken.

Numerical validation

The observer has been shown to converge with 100 uniformly drawn parameter and starting value points from the set described in Table 5.1. In this case, randomly chosen, but constant A have been applied. Regarding the mass moment of inertia, it was derived from the random variables as described in (4.20). The observer initial pose was always I, and its initial body velocity was always 0. The observed system's initial velocities were chosen in compliance with the constraints. All simulation iterations converged, with the development of the error values in 5 s depicted in Fig. 5.1. In addition, that the Lyapunov candidate function described in (5.14) was simulated simultaneously and its time derivative was always negative (with a tolerance of 1e−10). The observer parameters were $p_1 = 100$ and $p_2 = 0.005$.

In another validation step, a double pendulum, consisting of two rigid bodies with a time- and pose-varying constraint matrix, has been observed for another 100 starting values and parameter points. The parameters were again in accordance with Table 5.1, with the major difference that the natural equilibrium of the respective double pendulum were chosen as the observer's initial poses instead of I. Again, all instances converged.

Table 5.1: Numerical validation parameters

Parameter	Value range
masses	$[1, 100)$kg
mass moment of inertia eigenvalues	$[1, 100)$kgm^2
exponential coordinates of mass moment of inertia orientation	$[-\pi, \pi)$
system initial orientation exponential coordinates	$[-\pi, \pi)$
system initial position elements	$[-1, 1)$m
system initial linear velocity elements	$[-1, 1)$m/s
system initial angular velocity elements	$[-1, 1)$rad/s
input wrench	random noise with no frequencies higher than 5 Hz and an amplitude of no more than 1 N m and 1 N, respectively (see Table 5.2 for reference)
Constant Pfaffian constraint matrix	randomly sampled, then orthogonalized matrix $\in \mathbb{R}^{3\times 6}$
pendulum arm lengths	$[0.1, 10)$m

5.3 Extending the observer using velocity measurements

In some cases, the system velocity and pose might be available, but only infrequently or even unreliably. In these cases, it makes sense to employ an observer even though both pose and velocity are being measured.

5.3.1 Measuring constraints

We propose an observer which respects the exact same constraints as the observed system, which is assumed to be of the form given in (5.18). We will ensure

$$\hat{A}_{\hat{\mathrm{B}}}\hat{V} = A\mathrm{Ad}_{\eta^{-1}\hat{\mathrm{B}}}\hat{V} = A(\hat{g}\eta)\mathrm{Ad}_{\eta^{-1}\hat{\mathrm{B}}}\hat{V} = 0. \tag{5.24}$$

The motivation for this choice of $\hat{A}$ is that A is applicable on ${}_{\mathrm{B}}V$, represented in the B frame. In order to apply A on ${}_{\hat{\mathrm{B}}}\hat{V}$, we must first project it into the B frame, which we can do using the transformation adjoint: ${}_{\mathrm{B}}\hat{V} = \mathrm{Ad}_{\eta^{-1}}{}_{\hat{\mathrm{B}}}\hat{V}$.

The time derivative of $\hat{A}$ is

$$\dot{\hat{A}} = \dot{A}\mathrm{Ad}_{\eta^{-1}} - A\mathrm{ad}_{{}_{\mathrm{B}}V_\eta}\mathrm{Ad}_{\eta^{-1}}. \tag{5.25}$$

This means in particular that it can not be computed without knowledge of the observed system's velocity, as it depends on V_η, which in turn depends on V.

The observer dynamics are (5.19). The observer's constraint wrench, using (5.22b), is

$${}_{\hat{\mathrm{B}}}\hat{f}_{\mathrm{c}} = \hat{A}^{\mathrm{T}}(A\Lambda^{-1}A^{\mathrm{T}})^{-1}(A\Lambda^{-1}(-{}_{\mathrm{B}}f_{\mathrm{obs}} - \mathrm{ad}^*_{\mathrm{Ad}_{\eta^{-1}}{}_{\hat{\mathrm{B}}}\hat{V}}\Lambda\mathrm{Ad}_{\eta^{-1}}{}_{\hat{\mathrm{B}}}\hat{V}) - \dot{\hat{A}}V) = \mathrm{Ad}^{\mathrm{T}}_{\eta^{-1}}A^{\mathrm{T}}\hat{\lambda}_{\mathrm{c}}. \tag{5.26}$$

It is clear that ${}_{\hat{\mathrm{B}}}\hat{V}^{\mathrm{T}}{}_{\hat{\mathrm{B}}}\hat{f}_{\mathrm{c}} = {}_{\hat{\mathrm{B}}}\hat{V}^{\mathrm{T}}\hat{A}^{\mathrm{T}}\hat{\lambda}_{\mathrm{c}} = 0$, i. e. the constraint wrench is passive. For the observer dynamics, we use (5.21) to compute

$${}_{\mathrm{B}}\hat{f}_{\mathrm{c}} = \mathrm{Ad}^{\mathrm{T}}_{\eta}{}_{\hat{\mathrm{B}}}\hat{f}_{\mathrm{c}} = A^{\mathrm{T}}\hat{\lambda}_{\mathrm{c}}. \tag{5.27}$$

5.3.2 Stability and convergence

The stability proof is analogous to the one shown in [13]. We define $e = \begin{bmatrix}\varepsilon^{\mathrm{T}} & (V_{\mathrm{e}}^{\mathrm{b}})^{\mathrm{T}}\end{bmatrix}^{\mathrm{T}}$ as an observer error state.

Lyapunov's second (direct) method

An important effect of our choice of $\hat{A}$ is that the constraint forces are passive with respect to the velocity error, i.e.

$$({}_{\mathrm{B}}V_{\mathrm{e}})^{\mathrm{T}}{}_{\mathrm{B}}f_{\mathrm{c}} = ({}_{\mathrm{B}}V - \mathrm{Ad}_{\eta^{-1}}{}_{\hat{\mathrm{B}}}\hat{V})^{\mathrm{T}}A^{\mathrm{T}}\tau = {}_{\mathrm{B}}V^{\mathrm{T}}A^{\mathrm{T}}\tau - {}_{\hat{\mathrm{B}}}\hat{V}^{\mathrm{T}}\hat{A}^{\mathrm{T}}\tau = 0 \tag{5.28a}$$

$$({}_{\mathrm{B}}V_{\mathrm{e}})^{\mathrm{T}}{}_{\mathrm{B}}\hat{f}_{\mathrm{c}} = ({}_{\mathrm{B}}V - \mathrm{Ad}_{\eta^{-1}}{}_{\hat{\mathrm{B}}}\hat{V})^{\mathrm{T}}A^{\mathrm{T}}\hat{\tau} = {}_{\mathrm{B}}V^{\mathrm{T}}A^{\mathrm{T}}\hat{\tau} - {}_{\hat{\mathrm{B}}}\hat{V}^{\mathrm{T}}\hat{A}^{\mathrm{T}}\hat{\tau} = 0 \tag{5.28b}$$

The Lyapunov candidate function is

$$W = \frac{1}{2}e^{\mathrm{T}}Pe. \tag{5.29}$$

with P as

$$P = \begin{bmatrix} P_1 & 0 \\ 0 & P_2\Lambda \end{bmatrix} = P^{\mathrm{T}}. \tag{5.30}$$

$P_1 = p_1 I$ and $P_2 = p_2 I$ are each multiples of the identity matrix, so W is a positive definite function.

Then the derivative of the Lyapunov function is

$$\begin{aligned}\dot{W} &= e^{\mathrm{T}} P \dot{e} \\ &= \varepsilon^{\mathrm{T}} P_1 (\mathrm{B_r}(\varepsilon)\,{}_{\mathrm{B}}V_{\mathrm{e}} - k\varepsilon) + ({}_{\mathrm{B}}V_{\mathrm{e}})^{\mathrm{T}} P_2 (-f_0 + C({}_{\mathrm{B}}V_{\mathrm{e}}, {}_{\mathrm{B}}V)\,{}_{\mathrm{B}}V_{\mathrm{e}} + {}_{\mathrm{B}}f_{\mathrm{c}} - {}_{\mathrm{B}}\hat{f}_{\mathrm{c}}) \\ &= -kp_1 ||\varepsilon||^2 + \varepsilon^{\mathrm{T}} P_1 \mathrm{B_r}(\varepsilon) V_{\mathrm{e}}^{\mathrm{b}} - ({}_{\mathrm{B}}V_{\mathrm{e}})^{\mathrm{T}} P_2 f_0.\end{aligned} \tag{5.31}$$

By choosing $f_0 = P_2^{-1} \mathrm{B_r^T}(\varepsilon) P_1 \varepsilon$, the derivative reduces to

$$\dot{W} = -kp_1 ||\varepsilon||^2 \leq 0. \tag{5.32}$$

This is exactly the same as (5.17). Additionally, § 5.1.5 holds analogously to complete the stability proof.

5.4 Complementing the observer with a position controller

A very important application of system state measurements is feedback control. In this section, a position controller will be proposed which stabilizes a desired constant equilibrium g_{d}.

5.4.1 Error variable

In this approach, we control the observer state to the desired equilibrium. As such, the error variable and its representation in $\mathbb{R}^6$ are

$$\Xi = \hat{g}^{-1} g_{\mathrm{d}} \tag{5.33a}$$

$$\xi = [\log \Xi]^{\wedge}. \tag{5.33b}$$

As we require the desired equilibrium to be constant, we find the error variable's time derivatives as

$$\begin{aligned}\dot{\Xi} = \frac{d\hat{g}^{-1}}{dt} g_{\mathrm{d}} = -\hat{g}^{-1} \dot{\hat{g}} \hat{g}^{-1} g_{\mathrm{d}} = -\left[{}_{\hat{\mathrm{B}}}\hat{V} + \mathrm{Ad}_{\eta} K\varepsilon\right]^{\wedge} \Xi \\ = -\Xi\Xi^{-1}\left[{}_{\hat{\mathrm{B}}}\hat{V} + \mathrm{Ad}_{\eta} K\varepsilon\right]^{\wedge} \Xi = \Xi\left[-\mathrm{Ad}_{\Xi^{-1}}\,{}_{\hat{\mathrm{B}}}\hat{V} - \mathrm{Ad}_{\Xi^{-1}} \mathrm{Ad}_{\eta} K\varepsilon\right]^{\wedge}\end{aligned} \tag{5.34a}$$

$$\dot{\xi} = \mathrm{B_r}(\xi)(-\mathrm{Ad}_{\Xi^{-1}}\,{}_{\hat{\mathrm{B}}}\hat{V} - \mathrm{Ad}_{\Xi^{-1}} \mathrm{Ad}_{\eta} K\varepsilon). \tag{5.34b}$$

5.4.2 Control law

We aim to stabilize Ξ to I. To this end, the proposed control law is

$${}_{\mathrm{B}}f_{\mathrm{obs}} = \mathrm{Ad}_{\eta}^{\mathrm{T}} \mathrm{Ad}_{\Xi^{-1}}^{\mathrm{T}} \mathrm{B_r^T}(\xi) K_{\mathrm{ctrl}} \xi - D(\varepsilon, \xi) \mathrm{Ad}_{\eta^{-1}}\,{}_{\hat{\mathrm{B}}}\hat{V}, \tag{5.35}$$

where K_{ctrl} denotes a constant proportional gain and $D(\varepsilon, \xi)$ is an adaptive damping gain.

In order to realize this control low, we choose f_{in} accordingly, satisfying (5.23), as

$$f_{\mathrm{in}} = {}_{\mathrm{B}}f_{\mathrm{obs}} + \Lambda \mathrm{ad}_{K\varepsilon} \mathrm{Ad}_{\eta^{-1}}\,{}_{\hat{\mathrm{B}}}\hat{V} - f_0. \tag{5.36}$$

It is clear that this is a PD-type controller. However, we use an adaptive dampening gain $D(\varepsilon, \xi)$, which is chosen as

$$D(\varepsilon, \xi) = D_0 - I \begin{cases} \min(\frac{\xi^{\mathrm{T}} K_{\mathrm{ctrl}} \mathrm{B_r}(\xi) \mathrm{Ad}_{\Xi^{-1}} \mathrm{Ad}_\eta K \varepsilon}{\|\mathrm{Ad}_{\eta^{-1}} {}_{\hat{\mathrm{B}}}\hat{V}\|_2}, 0) & \hat{V} \neq 0 \\ 0 & \text{else} \end{cases}, \tag{5.37}$$

where D_0 is a constant positive definite damping gain.

When measuring the system velocity, we choose

$$D(\varepsilon, \xi) = D_0 - I \begin{cases} \min(\frac{\xi^{\mathrm{T}} K_{\mathrm{ctrl}} \mathrm{B_r}(\xi) \mathrm{Ad}_{\Xi^{-1}} \mathrm{Ad}_\eta K \varepsilon + {}_{\hat{\mathrm{B}}}\hat{V}^{\mathrm{T}} \mathrm{Ad}^{\mathrm{T}}_{\eta^{-1}} \Lambda \mathrm{ad}_{V_\eta} \mathrm{Ad}_{\eta^{-1}} {}_{\hat{\mathrm{B}}}\hat{V}}{\|\mathrm{Ad}_{\eta^{-1}} {}_{\hat{\mathrm{B}}}\hat{V}\|_2}, 0) & \hat{V} \neq 0 \\ 0 & \text{else} \end{cases}. \tag{5.38}$$

5.4.3 Stability analysis

Lyapunov's second method

For the stability analysis, we consider $e = \begin{bmatrix} \xi^{\mathrm{T}} & {}_{\hat{\mathrm{B}}}\hat{V}^{\mathrm{T}} \end{bmatrix}^{\mathrm{T}}$. The Lyapunov function candidate is the energy of the observer in the controller's potential field,

$$W = \frac{1}{2} e^{\mathrm{T}} \begin{bmatrix} K_{\mathrm{ctrl}} & 0 \\ 0 & \Lambda \end{bmatrix} e = \frac{1}{2} \xi^{\mathrm{T}} K_{\mathrm{ctrl}} \xi + \frac{1}{2} {}_{\hat{\mathrm{B}}}\hat{V}^{\mathrm{T}} \mathrm{Ad}^{\mathrm{T}}_{\eta^{-1}} \Lambda \mathrm{Ad}_{\eta^{-1}} {}_{\hat{\mathrm{B}}}\hat{V}. \tag{5.39}$$

Its time derivative is

$$\begin{aligned} \dot{W} &= \xi^{\mathrm{T}} K_{\mathrm{ctrl}} \dot{\xi} + {}_{\hat{\mathrm{B}}}\hat{V}^{\mathrm{T}} \mathrm{Ad}^{\mathrm{T}}_{\eta^{-1}} \Lambda \mathrm{Ad}_{\eta^{-1}} {}_{\hat{\mathrm{B}}}\dot{\hat{V}} - {}_{\hat{\mathrm{B}}}\hat{V}^{\mathrm{T}} \mathrm{Ad}^{\mathrm{T}}_{\eta^{-1}} \Lambda \mathrm{ad}_{V_\eta} \mathrm{Ad}_{\eta^{-1}} {}_{\hat{\mathrm{B}}}\hat{V} \\ &= -\xi^{\mathrm{T}} K_{\mathrm{ctrl}} \mathrm{B_r}(\xi) \mathrm{Ad}_{\Xi^{-1}} {}_{\hat{\mathrm{B}}}\hat{V} - \xi^{\mathrm{T}} K_{\mathrm{ctrl}} \mathrm{B_r}(\xi) \mathrm{Ad}_{\Xi^{-1}} \mathrm{Ad}_\eta K \varepsilon \\ &+ {}_{\hat{\mathrm{B}}}\hat{V}^{\mathrm{T}} \mathrm{Ad}^{\mathrm{T}}_{\eta^{-1}} \Lambda \mathrm{Ad}_{\eta^{-1}} \mathrm{Ad}_\eta \Lambda^{-1} ({}_{\mathrm{B}} f_{\mathrm{obs}} + {}_{\mathrm{B}} \hat{f}_{\mathrm{c}} + \mathrm{ad}^*_{\mathrm{Ad}_{\eta^{-1}} {}_{\hat{\mathrm{B}}}\hat{V}} \Lambda \mathrm{Ad}_{\eta^{-1}} {}_{\hat{\mathrm{B}}}\hat{V}) \\ &- {}_{\hat{\mathrm{B}}}\hat{V}^{\mathrm{T}} \mathrm{Ad}^{\mathrm{T}}_{\eta^{-1}} \Lambda \mathrm{ad}_{V_\eta} \mathrm{Ad}_{\eta^{-1}} {}_{\hat{\mathrm{B}}}\hat{V} \qquad \text{‘} \\ &= -\xi^{\mathrm{T}} K_{\mathrm{ctrl}} \mathrm{B_r}(\xi) \mathrm{Ad}_{\Xi^{-1}} {}_{\hat{\mathrm{B}}}\hat{V} + {}_{\hat{\mathrm{B}}}\hat{V}^{\mathrm{T}} \mathrm{Ad}^{\mathrm{T}}_{\Xi^{-1}} \mathrm{B}^{\mathrm{T}}_{\mathrm{r}}(\xi) K_{\mathrm{ctrl}} \xi - \xi^{\mathrm{T}} K_{\mathrm{ctrl}} \mathrm{B_r}(\xi) \mathrm{Ad}_{\Xi^{-1}} \mathrm{Ad}_\eta K \varepsilon \\ &- {}_{\hat{\mathrm{B}}}\hat{V}^{\mathrm{T}} \mathrm{Ad}^{\mathrm{T}}_{\eta^{-1}} D(\varepsilon, \xi) \mathrm{Ad}_{\eta^{-1}} {}_{\hat{\mathrm{B}}}\hat{V} - {}_{\hat{\mathrm{B}}}\hat{V}^{\mathrm{T}} \mathrm{Ad}^{\mathrm{T}}_{\eta^{-1}} \Lambda \mathrm{ad}_{V_\eta} \mathrm{Ad}_{\eta^{-1}} {}_{\hat{\mathrm{B}}}\dot{\hat{V}} \\ &= -\xi^{\mathrm{T}} \mathrm{Ad}_{\Xi^{-1}} \mathrm{Ad}_\eta K \varepsilon - {}_{\hat{\mathrm{B}}}\hat{V}^{\mathrm{T}} \mathrm{Ad}^{\mathrm{T}}_{\eta^{-1}} \Lambda \mathrm{ad}_{V_\eta} \mathrm{Ad}_{\eta^{-1}} {}_{\hat{\mathrm{B}}} - {}_{\hat{\mathrm{B}}}\hat{V}^{\mathrm{T}} \mathrm{Ad}^{\mathrm{T}}_{\eta^{-1}} D(\varepsilon, \xi) \mathrm{Ad}_{\eta^{-1}} {}_{\hat{\mathrm{B}}}\hat{V}\hat{V}. \end{aligned} \tag{5.40}$$

If velocity measurements are available and the adaptive dampening gain has been chosen according to (5.38), we can immediately find $\dot{W} \leq {}_{\hat{\mathrm{B}}}\hat{V}^{\mathrm{T}} \mathrm{Ad}^{\mathrm{T}}_{\eta^{-1}} D_0 \mathrm{Ad}_{\eta^{-1}} {}_{\hat{\mathrm{B}}}\hat{V}$.

When no velocity measurements are available, we find

$$\dot{W} \leq -{}_{\hat{\mathrm{B}}}\hat{V}^{\mathrm{T}} \mathrm{Ad}^{\mathrm{T}}_{\eta^{-1}} (\Lambda \mathrm{ad}_{V_\eta} + D_0) \mathrm{Ad}_{\eta^{-1}} {}_{\hat{\mathrm{B}}}\hat{V}. \tag{5.41}$$

$\Lambda \mathrm{ad}_{V_\eta}$ is generally not definite. However, if we assume the involved observer to eventually converge to $V_\eta = 0$, we can find an upper bound for $\|V_\eta\|_2$, while Λ is constant anyways.

This allows us to select a D_0 that is ensured to dominate $\Lambda \mathrm{ad}_{V_\eta}$, such that $\Lambda \mathrm{ad}_{V_\eta} + D_0$ is positive definite.

If in particular a Lyapunov function that is quadratic in $V_\mathrm{e}, \varepsilon$ and possibly more values can be found, then we can find an upper bound for V_η by first finding a relationship between V_e and the Lyapunov function value as

$$\|V_\eta\|_2^2 = V_\eta^\mathrm{T} V_\eta = V_\mathrm{e}^\mathrm{T} V_\mathrm{e} - 2V_\mathrm{e}^\mathrm{T} K\varepsilon + \varepsilon^\mathrm{T} K^2 \varepsilon =$$

$$\begin{bmatrix} \varepsilon & V_\mathrm{e} & \dots \end{bmatrix} \begin{bmatrix} K^2 & -K & 0 & \dots \\ -K & I & 0 & \dots \\ 0 & 0 & 0 & \dots \\ \vdots & \vdots & \vdots & \ddots \end{bmatrix} \begin{bmatrix} \varepsilon \\ V_\mathrm{e} \\ \vdots \end{bmatrix} = \tag{5.42a}$$

$$e^\mathrm{T} P_\eta e \leq kW = k e^\mathrm{T} P_\mathrm{obs} e$$

$$e^\mathrm{T} (P_\eta - kP_\mathrm{obs}) e \leq 0. \tag{5.42b}$$

We can find a k such that $(P_\eta - kP_\mathrm{obs})$ is negative definite. Then, (5.42b) is satisfied and we have

$$\|V_\eta\|_2 \leq \sqrt{kW}. \tag{5.43}$$

With a known starting value of the Lyapunov function or a sufficiently conservative estimate, a constant upper bound for $\|V_\eta\|_2$ is then found, because the Lyapunov function's value is non-increasing.

To find an upper bound of $-_{\hat{\mathrm{B}}}\hat{V}^\mathrm{T} \mathrm{Ad}_{\eta^{-1}}^\mathrm{T} (\Lambda \mathrm{ad}_{V_\eta}) \mathrm{Ad}_{\eta^{-1}\hat{\mathrm{B}}} \hat{V}$, we analyze the symmetric part of $\Lambda \mathrm{ad}_{V_\eta}$. This is useful because its eigenvalues provide a bound of the quadratic form

$$Q = \frac{1}{2}(\Lambda \mathrm{ad}_{V_\eta} + \mathrm{ad}_{V_\eta}^\mathrm{T} \Lambda) \tag{5.44a}$$

$$X^\mathrm{T} Q X \geq \|X\|_2^2 \lambda_\mathrm{min}(Q). \tag{5.44b}$$

The negative eigenvalue of Q with the largest magnitude is of interest, because it limits. The spectral norm of S is equal to the square root of the largest eigenvalue of SS, which is identical to the absolute value of the eigenvalue with the largest magnitude of S. This makes it a useful lower bound for the eigenvalue of interest,

$$\lambda_\mathrm{min}(Q) \geq -\|Q\|_2. \tag{5.45}$$

While computing the spectral norm or the eigenvalues of S is not easy symbolically, we can find an upper bound for this spectral norm using the Frobenius norm. The Frobenius norm of S can be found using its trace, as

$$\|Q\|_2 \leq \|Q\|_F = \sqrt{\mathrm{trace}(QQ)}. \tag{5.46}$$

As shown in § 6.2, this trace can be expressed in the form

$$\mathrm{trace}(QQ) = V_\eta^\mathrm{T} F(\Lambda) V_\eta. \tag{5.47}$$

Since $F(\Lambda)$ is a constant, and we know upper bounds for $\|V_\eta\|_2$, we can finally conclude an upper bound for the magnitude of the relevant eigenvalue of S,

$$\sqrt{\lambda_{\max}(F(\Lambda))}\|V_\eta\|_2 \geq \sqrt{\operatorname{trace}(QQ)} \geq \|Q\|_2 \geq |\lambda_{\min}|. \tag{5.48}$$

Choosing D_0 with only positive eigenvalues, of which the smallest has a larger magnitude than the bound found in (5.48) (for example $D_0 = 2\lambda_{\max}(F(\Lambda))\|V_\eta\|_2^2$), we can ensure $\dot{W} \leq 0$.

LaSalle's invariance principle

Since there is a set of points with $\dot{W} = 0$ outside of the desired equilibrium, we apply LaSalle's invariance principle.

The time derivative of the Lyapunov function is negative if and only if ${}_{\hat{\mathrm{B}}}\hat{V} \neq 0$. We analyze the trajectories in the subspace where ${}_{\hat{\mathrm{B}}}\hat{V} = 0$ and show that there are no closed trajectories in this subspace outside of the equilibrium ($e = 0$). This subspace can be defined as $\mathcal{I} = \{\xi \in \mathbb{R}^6 \cong \mathfrak{se}(3), {}_{\hat{\mathrm{B}}}\hat{V} \in \mathbb{R}^6 | \xi \neq 0, {}_{\hat{\mathrm{B}}}\hat{V} = 0\}$.

For any point in $\mathcal{I}$, (5.35) will evaluate to ${}_{\mathrm{B}}f_{\mathrm{obs}} = \mathrm{Ad}_\eta^{\mathrm{T}} \mathrm{Ad}_{\Xi^{-1}}^{\mathrm{T}} \mathrm{B}_{\mathrm{r}}^{\mathrm{T}}(\xi) K_{\mathrm{ctrl}} \xi \neq 0$. The observer's dynamics (5.19b) will be

$${}_{\hat{\mathrm{B}}}\dot{\hat{V}} = \mathrm{Ad}_\eta \Lambda^{-1}(I - P_{\mathrm{c}})_{\mathrm{B}}f_{\mathrm{obs}}, \tag{5.49}$$

where we collected some terms definining the constraint direction in P_{c} for legibility. It can be seen that ${}_{\hat{\mathrm{B}}}\dot{\hat{V}}$ is zero if and only if $(I - P_{\mathrm{c}})_{\mathrm{B}}f_{\mathrm{obs}} = 0$, that is, if the control wrench points directly parallel to the constraints. In this case, a nondesired equilibrium is found. This can happen if the desired equilibrium is placed outside the reachable workspace (stable nondesired equilibrium), or if the system is at a singularity with respect to the otherwise reachable desired equilibrium (unstable nondesired equilibrium).

If no nondesired equilibrium is reached however, the trajectory will immediately leave $\mathcal{I}$ again. The only closed trajectory satisfying ${}_{\hat{\mathrm{B}}}\hat{V} = 0$ outside of constraint-caused nondesired equilibria is $e(t) = 0, \forall t \geq 0$. We can conclude that the equilibrium $e = 0$ is asymptotically stable, however not globally. Depending on the constraints and the choice of the desired equilibrium, it can or will not be reached.

This controller works on the observer state. The assumption is that the observer works and thus the observed system will reach the equilibrium. For the presented observers, this is reasonable because their convergence is independent of the input wrench.

5.5 Simulations

The observers and the controller described in this chapter have been developed and verified using simulations.

5.5.1 Observer evaluation

Benefits of the extension

In Fig. 5.2, the results for a simulation of a rigid pendulum with continuous state measurements are shown. The initial configuration and the initial velocity of the system to be observed have been chosen randomly within the limits of the constraints, while the initial state of the observer was resting at the origin. A random, low-frequency actuation wrench along with gravity was applied. The highest frequency appearing in a Fourier series representation of the input wrench was limited to 5 Hz. The input wrench is shown in Table 5.2. The inertia parameters were chosen randomly as well. The simulation parameter values can be found in Table 5.2. The simulation has been run with the input wrench and constraints either disabled or enabled with all possible combinations considered. In addition to that, the constraints based on measured velocities and poses have been compared with those based on the estimated state. As to be expected, the best results are obtained leveraging as much information as possible, that is respecting both the input wrench and the constraints.

Since gravity is considered in the input wrench, not respecting the constraints leads to considerable position errors, in particular in the z-coordinate.

Not respecting the input wrench, as well as respecting neither the input wrench nor the constraints, leads to a phase delay in the observer value, because the forces acting on the real body are only conveyed indirectly through the pose measurements to the observer.

The measurement-based constraints did not show considerable differences to the observation-based constraints.

Here, a very low value for $p1$ has been chosen intentionally to show the differences made by the extensions to the observer more clearly. A higher value would lead to faster convergence and smaller errors in all cases.

A very interesting phenomenon can be observed in all the simulations shown in Fig. 5.2: The observer's pose does not respect the constraints. The observer initial pose is I, which corresponds to a pendulum arm length of 0. If it respected this constraint, the observer could never reach any position other than 0.

The movement violating the constraints is a direct result of the error term in (5.5), as the observer kinematics are not those of a rigid body with respect to the twist $\hat{V}$. That means that even with $\hat{V}$ respecting the constraints, $\dot{\hat{g}}$ might not.

As the results show, this can be very useful as it adds robustness against observer initial poses that don't satisfy the same constraints as the real system. In practice, this robustness is very useful, as errors in this regard are very likely. For instance, when modeling a pendulum, the arm length might be inaccurate. If the pose would respect the constraints as well as the velocity, the observer could never converge to the ground truth, as it's based on a different model. With the presented observer however, there will be pose updates that violate the constraints in a way that's beneficial for convergence.

Low frequency measurements

The observer for a single pendulum as described in Table 5.2 has been run with very low frequency (2 Hz) measurements. This shows how effective the observer's internal

Table 5.2: Simulation parameters

Parameter	Value
mass	$35.75\,\mathrm{kg}$
mass moment of inertia	$\begin{bmatrix} 43.95 & -4.08 & -6.47 \\ -4.08 & 33.02 & 1.93 \\ -6.47 & 1.93 & 29.08 \end{bmatrix} \mathrm{kgm}^2$
system initial pose	$\begin{bmatrix} 0.621 & 0 & -0.784 & 2.351 \\ 0.754 & 0.274 & 0.598 & -1.793 \\ 0.214 & -0.962 & 0.170 & -0.510 \\ 0 & 0 & 0 & 1 \end{bmatrix} (\mathrm{m})$
system initial body velocity	$\begin{bmatrix} -0.127 & -0.096 & 0.9195 & -0.2883 & 0.3821 & 0 \end{bmatrix}^{\mathrm{T}} (\mathrm{rad/s}, \mathrm{m/s})$
observer initial pose	I
observer initial body velocity	0
p1	5
p2	0.1
input wrench	$f_{\mathrm{g}} + f_{\mathrm{act}}$
actuation wrench	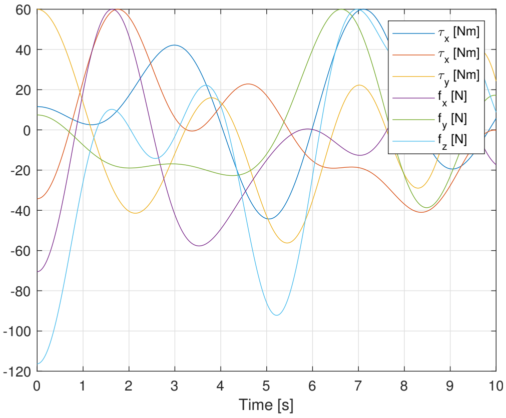
desired pose	$\begin{bmatrix} 0.877 & 0 & -0.481 & 1.442 \\ 0.028 & 0.998 & 0.051 & -0.154 \\ 0.480 & -0.058 & 0.875 & -2.626 \\ 0 & 0 & 0 & 1 \end{bmatrix} (\mathrm{m})$

state propagation is. In addition to that, it gives a good insight into how the observer works. It can be seen that at every new measurement, there is a jump of the observer pose towards the measured pose. In addition to that, there's an impulse wrench acting on the observer to push it towards the true pose, which results in a jump in the body velocity.

It should be noted that in order to achieve convergence at low frequencies, the observer gains had to be tuned very aggressively ($p_1 = 10000, p_2 = 0.02$). This directly compromises its robustness against noisy measurements however.

5.5.2 Controller evaluation

The presented controller has been applied to the single pendulum as described in Table 5.2. In addition to that, a random desired pose has been drawn, also to be found in Table 5.2. Differently to the previous experiments, the input wrench is now given only by the control input, while gravity is disabled. We compare the proposed controller to a simple PD controller using measured values, whose control law is

$$_{\mathrm{B}}f_{\mathrm{in}} = K_{\mathrm{ctrl}} \left[\log g^{-1} g_{\mathrm{d}}\right] - D_{0\mathrm{B}}V. \tag{5.50}$$

With continuous measurements, this controller outperforms the proposed observer at identical constant gains, because it acts directly on the system state, as can be seen in Fig. 5.4.

At lower measurement frequencies however, the control wrench described in (5.50) can be updated only rarely. It is reasonable to completely disable it while no measurements are available, as holding its value could easily drive major instabilities. This could occur when the system velocity changes while the input wrench stays constant until both point in the same direction, which would make the control input *active*, i.e. the system energy would be increased.

As a result, only short bursts of control input can be realized when relying on direct measurements. This, of course, causes a need for very high control gains to achieve convergence in a meaningful time frame.

In Fig. 5.5, simulation results at a measurement rate of 2 Hz with a control input frequency of 1000 Hz are shown. It is clear that the observer estimates provide a meaningful basis for high-frequency control inputs.

5.5.3 Simulation of some example robots

In addition to the rigid pendulum shown in the previous subsections, we tested a few multi-body systems to show the wide applicability of this modeling approach along with the observer and the controller:

- A spherical double pendulum, which can represent the SAM when mounted to a hook. This model is used to show the robustness against modeling parameter inaccuracies.
- A manipulator consisting of three translational joints followed by three rotational joints. This model demonstrates the applicability of the presented controller.

- The SAM including a rigid pendulum base and a 7-DoF manipulator. This model shows the applicability of the presented framework as a whole to complex systems subject to modeling inaccuracies.

Double pendulum

A rigid double pendulum as described in § 3.2 was used to demonstrate the effects of model parameter inaccuracies. To this end, the observer was provided with a different inertia matrix $\tilde{\Lambda}$ than the observed system (Λ). The parameters are listed in Table 5.3. The difference within the individual parameter values was within 10 %, but still considerable.

In Fig. 5.6, it is clear that although the observer based on the inaccurate parameters seems to converge and the error values very quickly become bounded, using accurate parameters greatly improves the performance. However, it is shown that even with inaccurate parameters, the observer stays within a vicinity of the true system state. It can be concluded that the observer's stability is relatively robust against parameter inaccuracies, although they limit its performance.

Table 5.3: Simulation parameters to evaluate robustness against parameter inaccuracies

Parameter	True Value	Inaccurate value
mass of body 1	34.07 kg	40.78 kg
mass moment of inertia of body 1	$\begin{bmatrix} 90.35 & 3.84 & -8.36 \\ 3.84 & 41.52 & -0.78 \\ -8.36 & -0.78 & 43.26 \end{bmatrix} \mathrm{kgm}^2$	$\begin{bmatrix} 97.84 & 11.94 & -12.90 \\ 11.94 & 44.71 & -2.89 \\ -12.90 & -2.89 & 47.13 \end{bmatrix} \mathrm{kgm}^2$
mass of body 2	87.62 kg	94.86 kg
mass moment of inertia of body 2	$\begin{bmatrix} 168.53 & -0.25 & -12.35 \\ -0.25 & 145.79 & 11.70 \\ -12.35 & 11.70 & 94.05 \end{bmatrix} \mathrm{kgm}^2$	$\begin{bmatrix} 148.55 & 5.71 & 0.39 \\ 5.71 & 155.69 & -18.15 \\ 0.39 & -18.15 & 97.91 \end{bmatrix} \mathrm{kgm}^2$

Manipulator

Using the method described in § 3.6, a model of a relatively simple manipulator was obtained. The system contains 6 moving rigid bodies and 6 joints, which equates to $6 \cdot 5 = 30$ constraints and $6 \cdot 6 - 6 \cdot 5 = 6$ remaining DoF.

In this instance, the joint wrenches are not computed explicitly. However, the general control wrenches obtained from the controller will be projected such that only parts orthogonal to the constraints remain, using

$$
{}_{\mathrm{B}}f_{\text{in, filtered}} = (I - \mathrm{Ad}_\eta^{\mathrm{T}}\hat{A}^{\mathrm{T}}(\hat{A}\mathrm{Ad}_\eta\Lambda^{-1}\mathrm{Ad}_\eta^{\mathrm{T}}\hat{A}^{\mathrm{T}})^{-1}\hat{A}\mathrm{Ad}_\eta\Lambda^{-1})\,{}_{\mathrm{B}}f_{\text{in}}. \tag{5.51}
$$

The filtering takes place with respect to the observer constraints, because it is assumed that no high frequency measurements of the true system state are available.

This does in theory not make any difference in the performance as the exact same filtering takes place in the observer dynamics, but especially in real applications it removes a noise source and reduces strain on the system.

The manipulator was controlled to a random desired equilibrium for its end effector that changes midway through the simulation. This allows to analyze the step response of the system twice. Because all 6 DoF of the robot are defined for a given equilibrium of the end effector, the proportional gain was set to zero for all other bodies.

It is important to note that for different compositions of joints, it might be very likely for the controller as described here to converge to a local minimum. This is due to the control wrench acting purely on the end effector body, where it might be fully counteracted by the constraint forces. In these cases, a transposed Jacobian can be used to find corresponding joint torques and forces corresponding to the control force. Alternatively, an inverse kinematics evaluation can give desired poses for all bodies involved which can be fed into the controller to obtain control wrenches for all bodies.

The cable-suspended aerial manipulator

Similarly to the manipulator used in § 5.5.3, the SAM was modeled according to § 3.6, with the first rigid body being constrained by (2.63) and the subsequent bodies being attached to it through in total 7 rotational joints. The number of constraints on the system sums to $5 \cdot 7 + 3 = 38$, which means $8 \cdot 6 - 38 = 10$ DoF remain.

As in § 5.5.3, the inertia matrices the model runs on are randomly drawn. In addition to that, the values that are fed to the observer are slightly modified from the true values with the intent to inspect the effects of system parameter inaccuracies in combination with the controller operating. Overall, this should make for an overall close representation of a real application. The parameter choice is shown in Table 5.4

Table 5.4: Simulation parameters for the SAM model

Parameter	True Value	Inaccurate value
mass of the platform	55 kg	59.31 kg
mass moment of inertia of the platform	$\begin{bmatrix} 80.19 & -0.10 & 2.74 \\ -0.10 & 80.05 & -1.40 \\ 2.74 & -1.40 & 119.76 \end{bmatrix} \text{kgm}^2$	$\begin{bmatrix} 77.70 & 0.53 & 3.16 \\ 0.53 & 67.12 & -1.96 \\ 3.16 & -1.96 & 124.45 \end{bmatrix} \text{kgm}^2$
mass of an exemplary robot link	2 kg	1.97 kg
mass moment of an exemplary robot link	$\begin{bmatrix} 2 & 0 & 0 \\ 0 & 2 & 0 \\ 0 & 0 & 2 \end{bmatrix} \text{kgm}^2$	$\begin{bmatrix} 1.72 & -0.01 & 0.02 \\ -0.01 & 1.82 & 0 \\ 0.02 & 0 & 1.95 \end{bmatrix} \text{kgm}^2$

As in § 5.5.3, the desired equilibrium was defined only for the end effector, leaving 4 degrees of freedom unused. In future work, this could be leveraged for secondary tasks using whole-body control, such as shown in [4]. In this simulation however, they are not being used.

Halfway through the simulation, the desired equilibrium changes as it did in the manipulator scenario.

The parameters for this simulation are only roughly based on the SAM's structure, but not an exact representation. Still, the results prove the concept. The simulation results are shown in Fig. 5.8.

It is clear that the combination of observer and controller presented here is capable of controlling the SAM model's end effector to a desired equilibrium.

5.6 Experiments

In order to evaluate the performance of the presented observers on real data, we applied them on the data collected in the experiments. The controller was not evaluated experimentally.

We used the rigid pendulum model as described in § 3.1 for the observer because no intermediary mass was involved and even the rigid model could be shown to successfully reproduce most reasonable experimental results.

5.6.1 Used sensors

The SAM currently features two exteroceptive sensors that provide meaningful measurements regarding its pose: An IMU and a camera whose data is fed into a visual Simultaneous Localization and Mapping (SLAM) algorithm. In this case, we are only interested in its visual odometry results.

Inertial measurement units

The SAM is equipped with an IMU that provides regular measurements of its orientation. Using the rigid pendulum assumption, we can reconstruct its full pose from this. The position of the inertial frame in the body frame is constant and known, so we can easily transform it into the inertial frame once we know the body orientation, which completes the full pose to

$$
{}_{\mathrm{I}}p_{\mathrm{IB}} = -{}_{\mathrm{I}}R_{\mathrm{B}}{}_{\mathrm{B}}p_{\mathrm{BI}} \tag{5.52a}
$$

$$
{}_{\mathrm{I}}g_{\mathrm{B}} = \begin{bmatrix} {}_{\mathrm{I}}R_{\mathrm{B}} & {}_{\mathrm{I}}p_{\mathrm{IB}} \\ 0 & 1 \end{bmatrix} \tag{5.52b}
$$

The IMU's data can contain a noticeable drift ${}_{\mathrm{m}}\omega_{\mathrm{d}} = \mathit{const.}$. In addition to that, the reported orientation is offset from the true orientation of the SAM (R_{P}), which might be due to its mounting or its calibration. Yet another constant rotation R_{eI} can appear between the inertial frame respected in the IMU and the inertial frame of interest. In total, the measured orientation R_{m} satisfies

$$
R_{\mathrm{m}} = R_{\mathrm{eI}} R_{\mathrm{P}} R_{\mathrm{e}} \tag{5.53a}
$$

$$
\dot{R}_{\mathrm{m}} = R_{\mathrm{m}} ({}_{\mathrm{m}}\omega_{\mathrm{P}} + {}_{\mathrm{m}}\omega_{\mathrm{d}})_{\times} \tag{5.53b}
$$

$$
\dot{R}_{\mathrm{P}} = R_{\mathrm{P}} ({}_{\mathrm{P}}\omega_{\mathrm{P}})_{\times}. \tag{5.53c}
$$

From this, we can find the time derivative of the orientation error as

$$\begin{aligned}\dot{R}_{\mathrm{e}} &= R_{\mathrm{P}}^{\mathrm{T}} R_{\mathrm{eI}}^{\mathrm{T}} R_{\mathrm{m}} ({}_{\mathrm{m}}\omega_{\mathrm{P}} + {}_{\mathrm{m}}\omega_{\mathrm{d}})_\times - ({}_{\mathrm{P}}\omega_{\mathrm{P}})_\times R_{\mathrm{P}}^{\mathrm{T}} R_{\mathrm{eI}}^{\mathrm{T}} R_{\mathrm{m}} \\ &= R_{\mathrm{e}}({}_{\mathrm{m}}\omega_{\mathrm{d}})_\times + R_{\mathrm{e}}(R_{\mathrm{e}}^{\mathrm{T}}\, {}_{\mathrm{P}}\omega_{\mathrm{P}})_\times - ({}_{\mathrm{P}}\omega_{\mathrm{P}})_\times R_{\mathrm{e}} \\ &= R_{\mathrm{e}}({}_{\mathrm{m}}\omega_{\mathrm{d}})_\times + ({}_{\mathrm{P}}\omega_{\mathrm{P}})_\times R_{\mathrm{e}} - ({}_{\mathrm{P}}\omega_{\mathrm{P}})_\times R_{\mathrm{e}} = R_{\mathrm{e}}({}_{\mathrm{m}}\omega_{\mathrm{d}})_\times .\end{aligned} \tag{5.54}$$

The orientation error can be compensated only once the true orientation and its derivative have been measured at least once. Assuming that the angular drift velocity is constant, we can integratethe drift from there according to (5.52), although that integration itself is prone to drift as a result of inaccuracies in the determination of ${}_{\mathrm{m}}\omega_{\mathrm{d}}$.

In practice, it is possible to initialize the drift compensation while the SAM is hanging at rest. The true angular velocity is 0 (at least on average over some time), and the true orientation has its z-axis exactly parallel to the inertial frame's. This leaves a degree of freedom, which can be set whenever the SAM leaves the equilibrium and its rotation axis is known. If there is a time period when the true orientation is known, it is also possible to run an optimization on the cost function

$$C_{\mathrm{d}} = \frac{1}{n} \sum_{k=0}^{n} \| [\log(R_{\mathrm{e0}} (\exp {}_{\mathrm{m}}\omega_{\mathrm{d}} \Delta t)^k R_{\mathrm{m}}^{\mathrm{T}}[k] R_{\mathrm{P}}[k])]^\vee \|_2^2, \tag{5.55}$$

where R_{e0} is the starting value of R_{e} and we discretized (5.54) with a sample time of Δt.

Camera

The visual odometry system provides a full pose measurement with respect to a starting pose. Inherently, it lacks knowledge of scale: a camera can not discriminate between an absolutely small environment that is close to the camera and the same environment in a larger scale that is further away.

However, the orientation is independent of the scale. If the orientation is known, we can apply (5.52) to reconstruct the full pose which we can then use to find the correct scale of the full pose.

Still, it is required to correctly initialize the camera pose. Again, this can be done similarly to the IMU setup, using data taken from a time period when the system was known to be at rest or optimizing for a temporarily known pose.

5.6.2 Sensor faults

Apart from inherent problems such as drift and scale ambiguity, the sensors might fail altogether. This could be caused for example by occlusion of the camera's field of view. It is important to identify and to deal with faulty measurements.

The proposed observers are inherently robust against missing measurements, but not as much against inaccurate measurements. This means that it is preferable to misclassify accurate measurements as faulty over misclassifying faulty measurements as accurate. This means that we aim for a high *specificity*, that is, we try to minimize the portion of false positives. Of course, this comes at the cost of lower *sensitivity*, increasing the rate of false negatives, but those should have a smaller impact on the observer's performance.

We identify faulty measurements primarily by discontinuities. Although those might not appear in the primary data, we can often find them in the respective derivatives. When a fault is detected, the corresponding data will not be fed into the observer, and the observer will continue integrating without new pose measurements.

Visual odometry fault

The visual odometry system can fail, for example in the case of occlusion of previously tracked points or when the environment in the field of view lacks texture. In these cases, the system will automatically integrate its pose based on the last available velocity measurement. Since this is done in particular to continue providing as meaningful data as possible, it is usually hard to identify. In this application however, the pendulum constraints always accelerate the platform towards the suspension point while it is moving, which is not considered in the visual odometry's integration method. This means that once a fault occurs, soon the provided pose will considerably violate the pendulum constraints and the fault can be identified. In particular, we compute

$$\begin{aligned} v_{\|} &= \|AV_{\mathrm{VO}}\|_2^2 \\ e_{\mathrm{l}} &= |\|r_{\mathrm{VO}}\|_2^2 - l|, \end{aligned} \tag{5.56}$$

where V_{VO} and r_{VO} are the velocity and the position measurements from the visual odometry system and l is the cable length. These two values can indicate a faulty measurement if they exceed a certain threshold.

5.6.3 Performance

The observer was run on datasets obtained throughout the experiments. The model parameters used are the results of the system identification.

In the experiments, gravity as an external wrench was acting on the system. While this is not an explicitly known force, the observer reconstructs it based on the estimated pose.

The data collected by the IMU and the camera contained inaccuracies with respect to the Vicon system. As such, even when the observer converged to the measurements, it did not necessarily converge to the ground truth.

In Fig. 5.9 and Fig. 5.10, the observer's performance when fed the pose measurements from the camera is shown.

In Fig. 5.11, the observer performance when fed the reconstructed (according to (5.52)) pose measurements from the IMU is shown.

In Fig. 5.12, a case is considered where the IMU provides measurements only at 2 Hz. However, (inaccurate) camera data at 20 Hz is available. For optimal performance, the observer uses all available measurements at their respective frequencies, considering them with different gains depending on their trustworthiness and frequency.

Overall, the observer is capable of estimating the measurements accurately and converges to those. If the measurements coincide with the ground truth, the observer successfully estimates the absolute pose of the SAM.

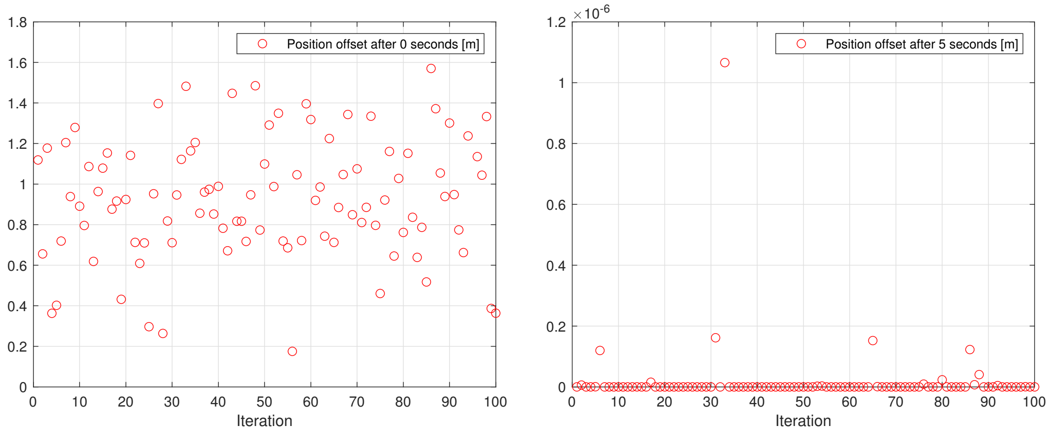

(a) Starting position difference

(b) Position difference after 5 s

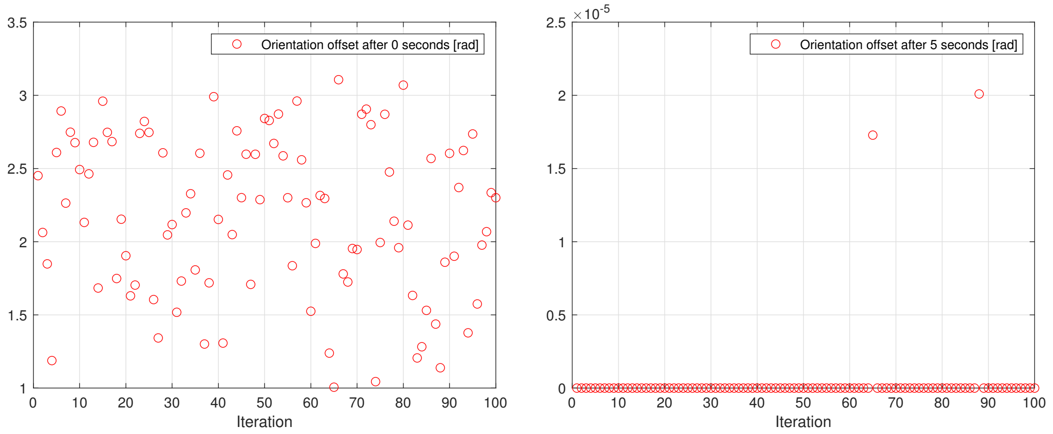

(c) Starting orientation difference

(d) Orientation difference after 5 s

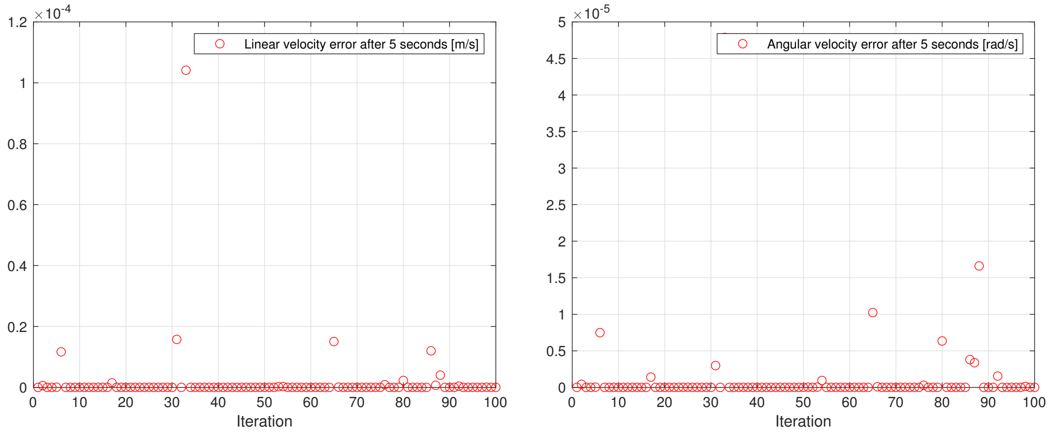

(e) Linear velocity difference after 5 s

(f) Angular velocity difference after 5 s

Figure 5.1: The results of the numerical validation. After 5 s, the remaining error has reduced to a fraction of the original. For the position offset, the distance between the origins is displayed. For the orientation, the euclidean norm of the exponential coordinates of the rotation between the frames is displayed. For the velocities, the euclidean norm of the respective velocity difference is displayed.

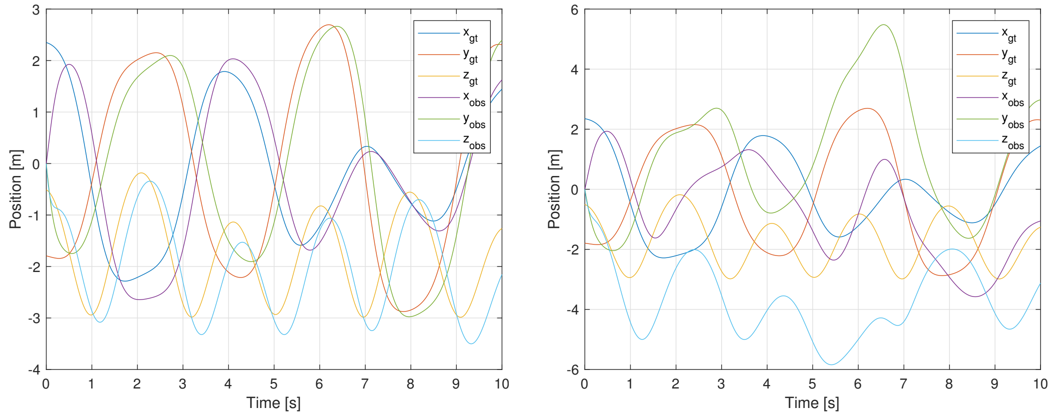

(a) Respecting neither constraints nor input wrench

(b) Not respecting constraints, but input wrench (y-axis is scaled differently)

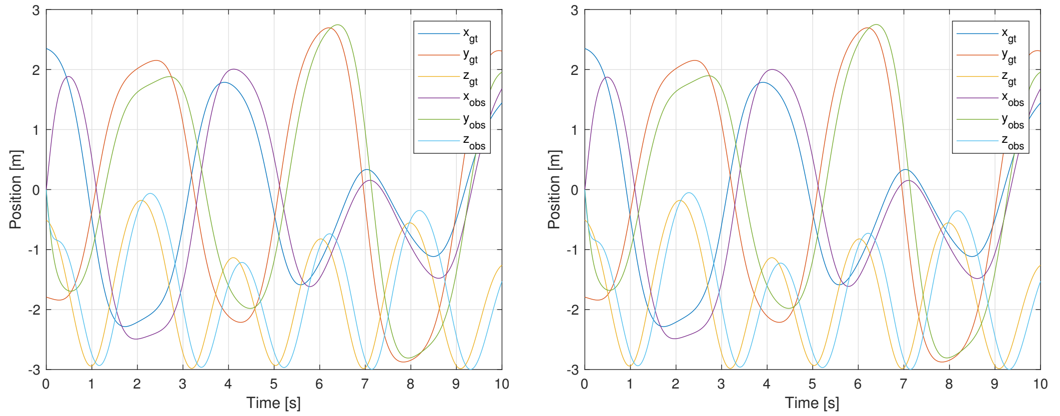

(c) Respecting estimated constraints, but not input wrench

(d) Respecting measured constraints, but not input wrench

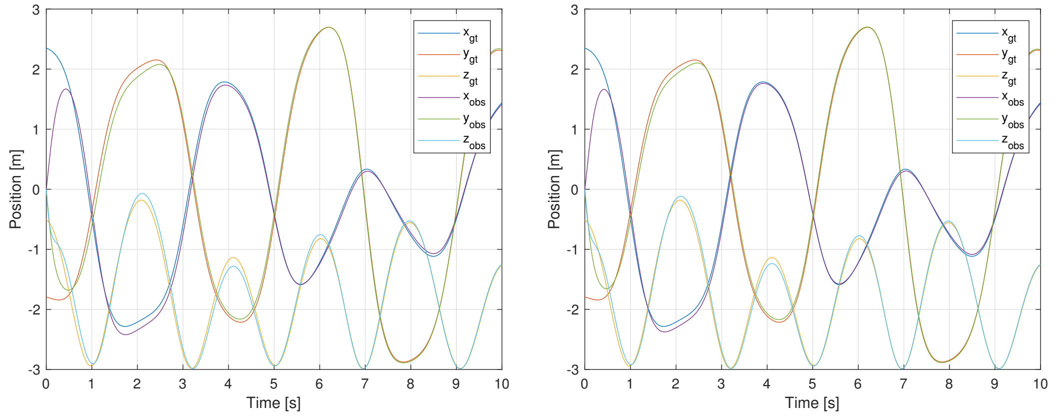

(e) Respecting estimated constraints and input wrench

(f) Respecting measured constraints and input wrench

Figure 5.2: Observing a rigid pendulum at different levels of model consideration. It is clear that both the constraints and input wrench need to be considered in order to achieve convergence. It can also be seen that using the measured constraints of the observed system is almost identical to using the estimated constraints.

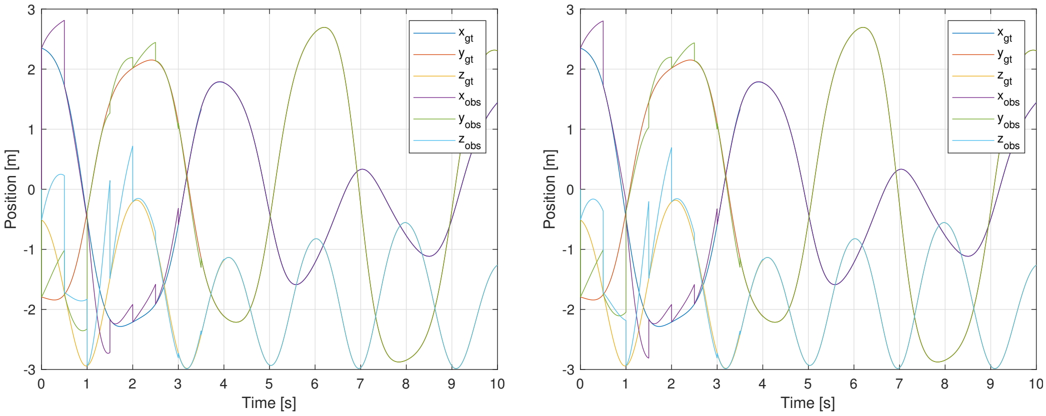

(a) Measured constraints (b) Estimated constraints

Figure 5.3: Observing a pendulum at very low frequency. Convergence can be achieved, but comes at the cost of robustness. Again, there is only marginal differences between using the measured state or the estimated one to compute the observer constraints.

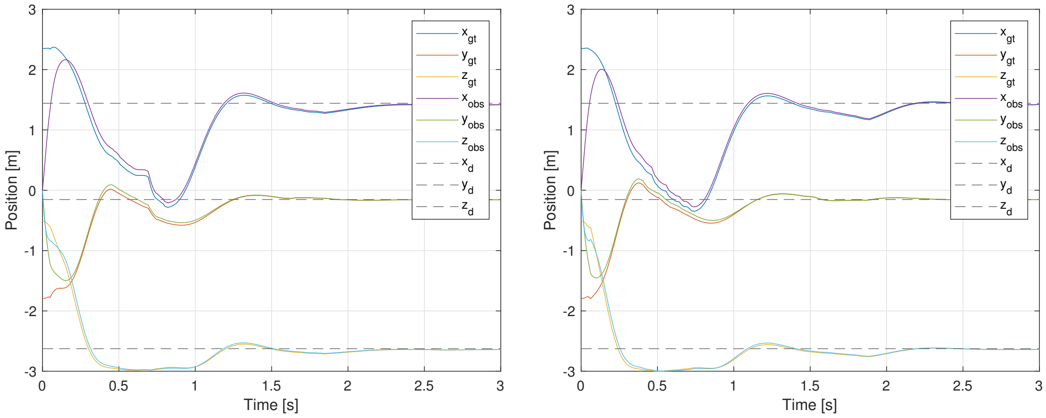

(a) Proposed controller without velocity measurements

(b) Proposed controller using velocity measurements

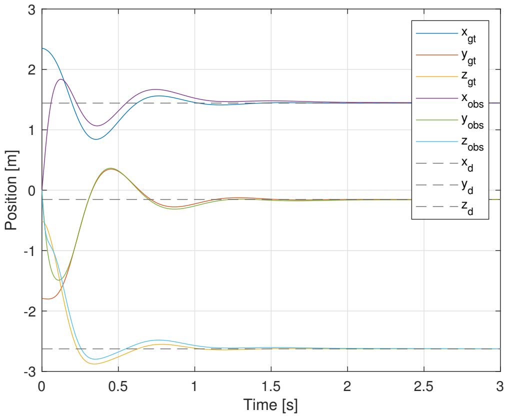

(c) PD controller using measurements

Figure 5.4: Comparing the proposed controller to a direct measurement-based controller in the continuous case. The control gains were set to $K_{\mathrm{ctrl}} = 2500$ and $D_0 = 250$. The observer gains were chosen intentionally conservative to $p_1 = 20$, $p_2 = 0.02$, to show that both the observer and the controller converge simultaneously and independently.

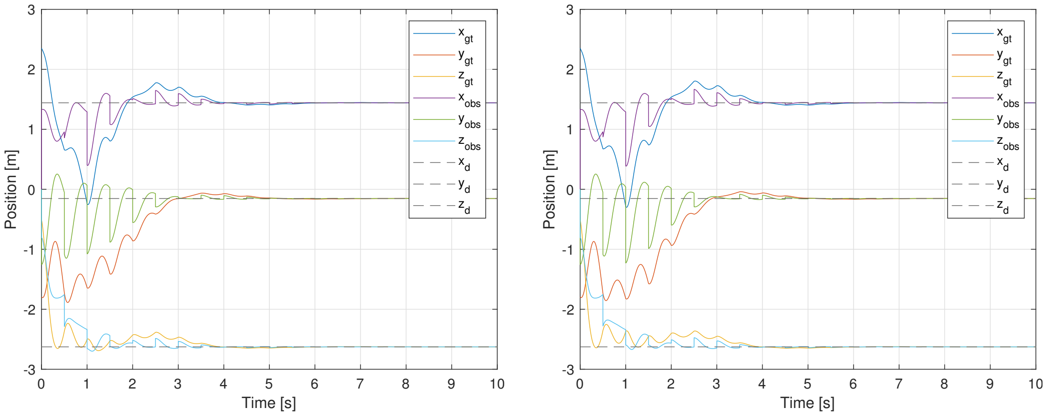

(a) Proposed controller without velocity measurements

(b) Proposed controller using velocity measurements

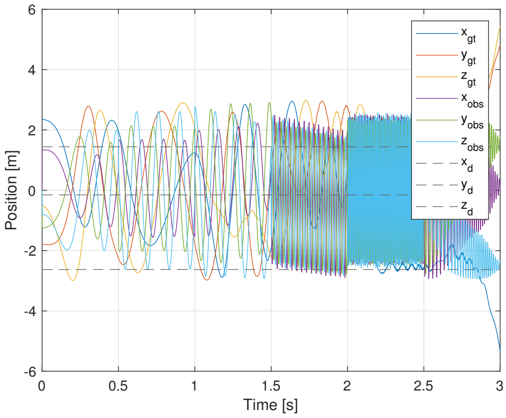

(c) PD controller using measurements

Figure 5.5: Comparing the proposed controller to a direct measurement-based at low frequency (2 Hz) measurements. The control gains were set again to $K_{\text{ctrl}} = 2500$ and $D_0 = 250$. The observer gains were chosen to $p_1 = 1000$, $p_2 = 0.02$. With the measurement-based controller, the simulation diverges after 3 seconds, whereas the estimation-based controller continuously reduces the error.

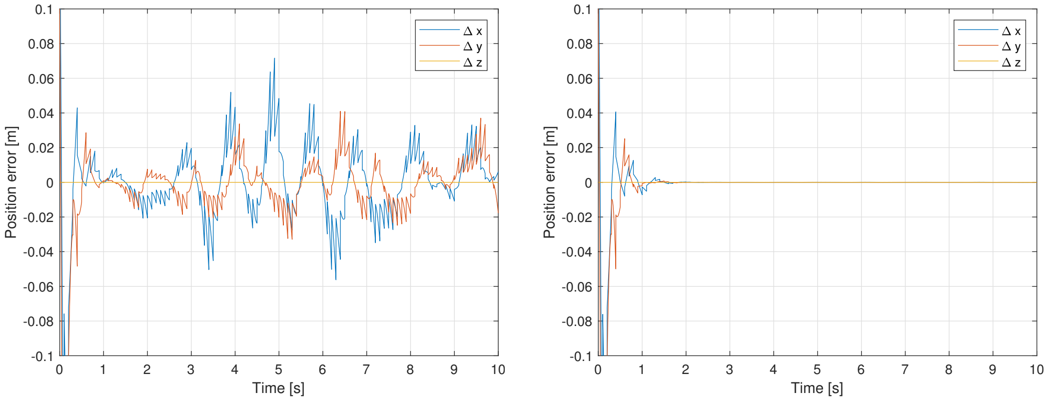

(a) Position error with inaccurate parameters

(b) Position error with accurate parameters

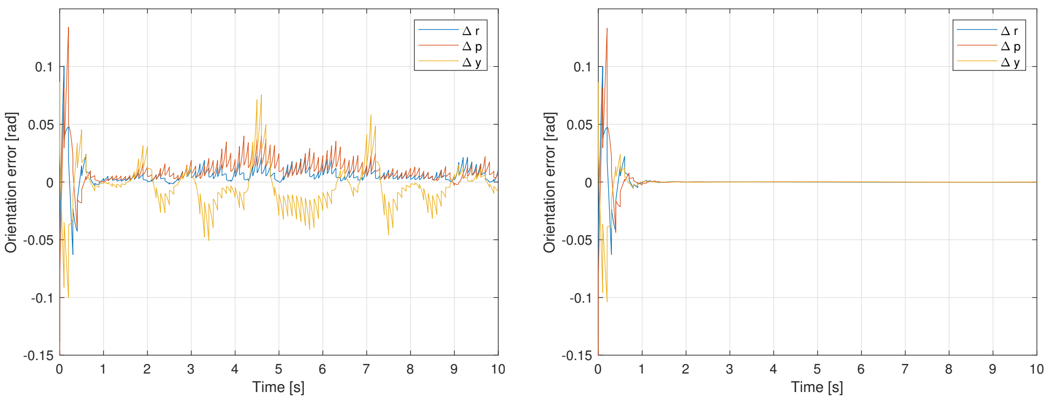

(c) Orientation error with inaccurate parameters

(d) Orientation error with accurate parameters

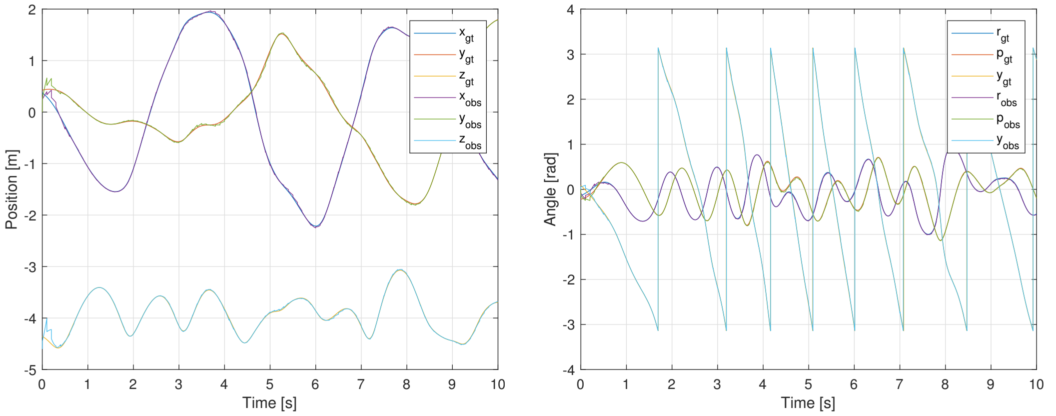

(e) Position tracking with inaccurate parameters

(f) Orientation tracking with inaccurate parameters

Figure 5.6: The effects of inaccurate system parameters at 10 Hz measurement rate. The observer gains were chosen to $p_1 = 1000$ and $p_2 = 0.001$. The orientation is presented in roll(α)-pitch(β)-yaw(γ) formulation, which is why a few jumps from close to 0 to close to 2π occur. The second body's behaviour is shown exemplarily, but represents the first body's results. The purely pose-based observer was employed for the presented data, but using velocity measurements produces nearly identical results.

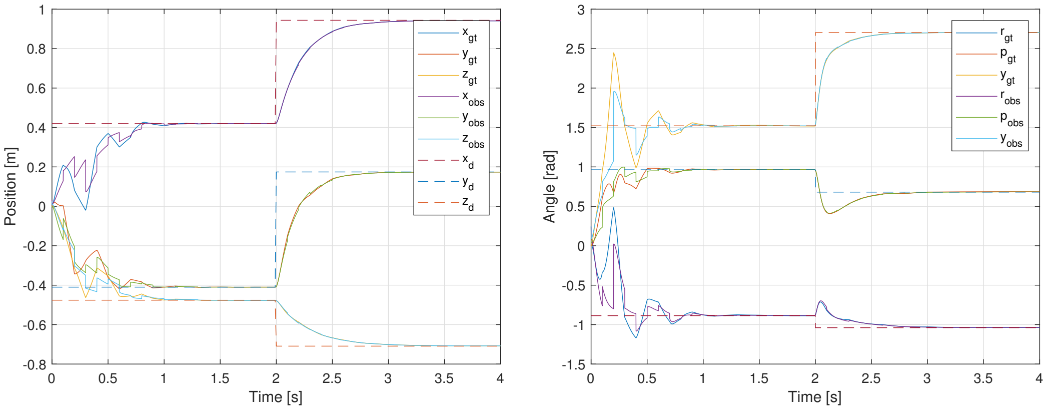

(a) End effector position (b) End effector orientation

Figure 5.7: The performance of the proposed controller and observer combination on a 6-DoF manipulator. The observer gains were chosen to $p_1 = 100$, $p_2 = 0.02$. The controller gains were set to $k_{\text{ctrl}} = 1000$ and $D_0 = 100$. The end effector is shown exemplarily, but all bodies' pose estimates converged to the ground truth. The purely pose-based combination was employed for the presented data, but using velocity measurements produces nearly identical results.

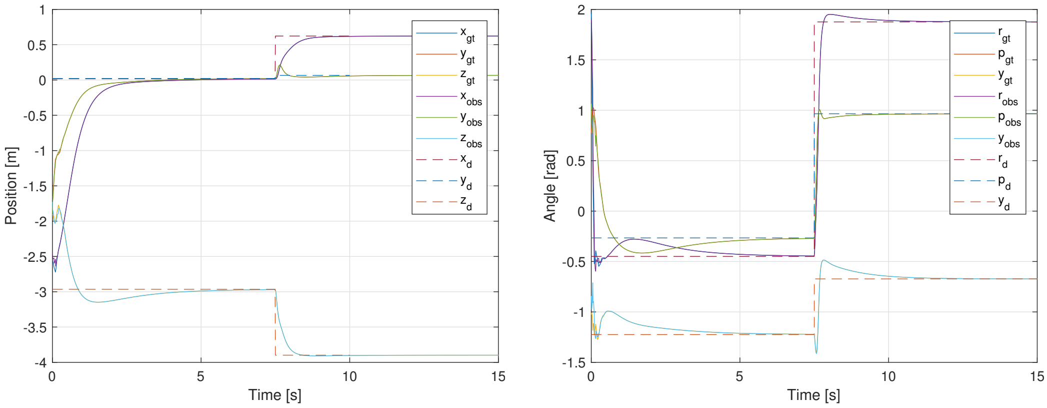

(a) End effector position

(b) End effector orientation

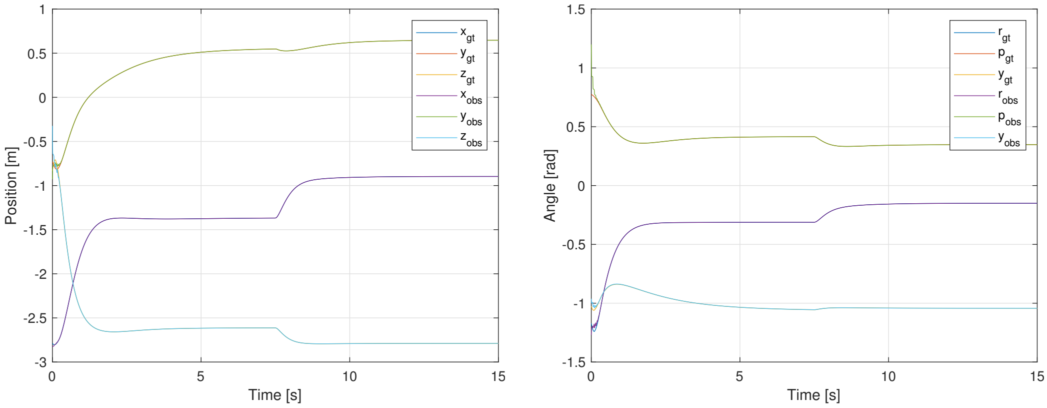

(c) Platform position

(d) Platform orientation

Figure 5.8: The performance of the proposed controller and observer combination on the SAM under parameter inaccuracies. The observer gains were chosen to $p_1 = 100$, $p_2 = 0.001$. The controller gains were set to $k_{\text{ctrl}} = 1000$ and $D_0 = 100$. The end effector and the base platform are shown exemplarily, but all bodies' pose estimates converged to the ground truth. The purely pose-based combination was employed for the presented data, but using velocity measurements produces nearly identical results.

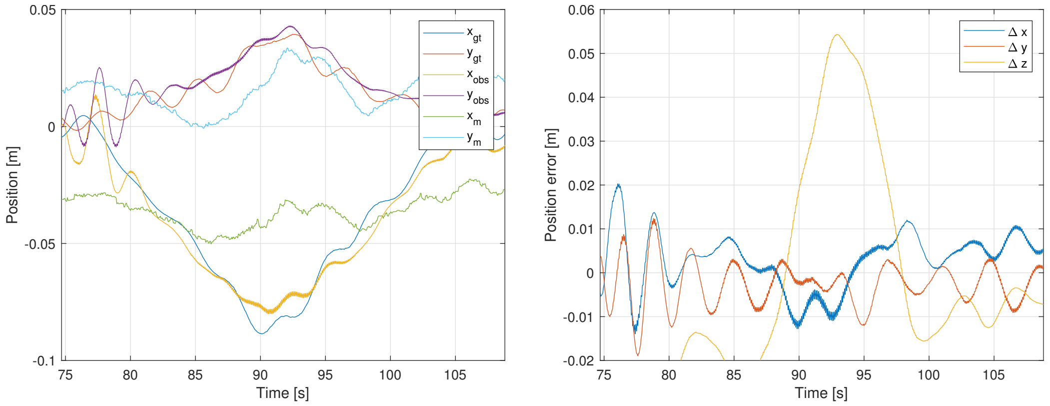

(a) Position tracking (b) Position error

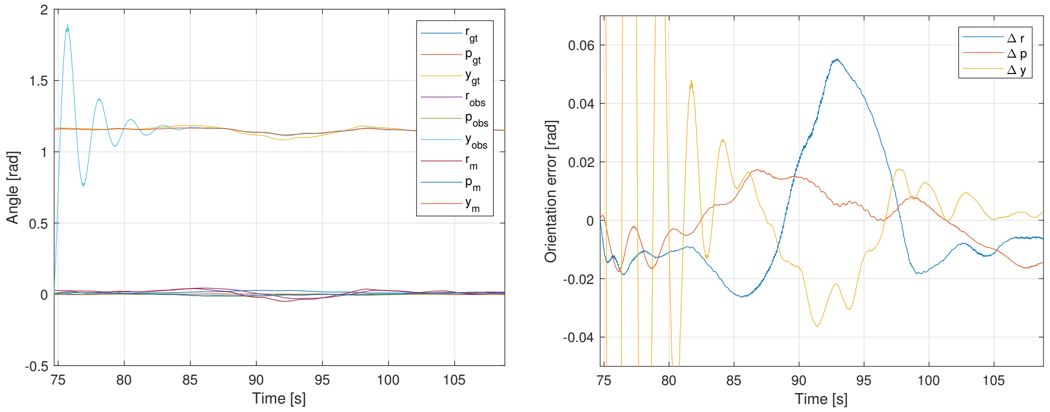

(c) Orientation tracking (d) Orientation error

Figure 5.9: In the position tracking for x and y, the observer gets closer to the ground truth data than to the measurements. This happens because the ground truth data better fits the underlying model and its constraints. However, there is no asymptotic convergence because there is an inconsistency between the measured data and the ground truth. The observer gains in this instance were $p_1 = 100$, $p_2 = 0.01$.

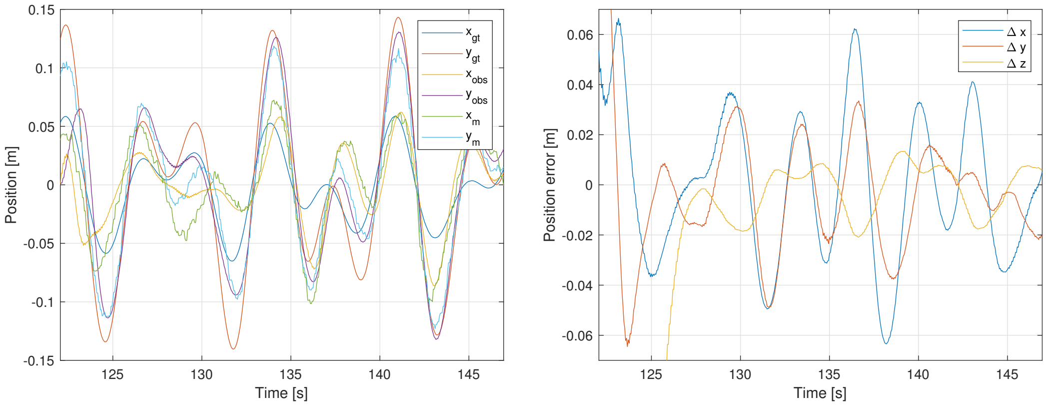

(a) Position tracking (b) Position error

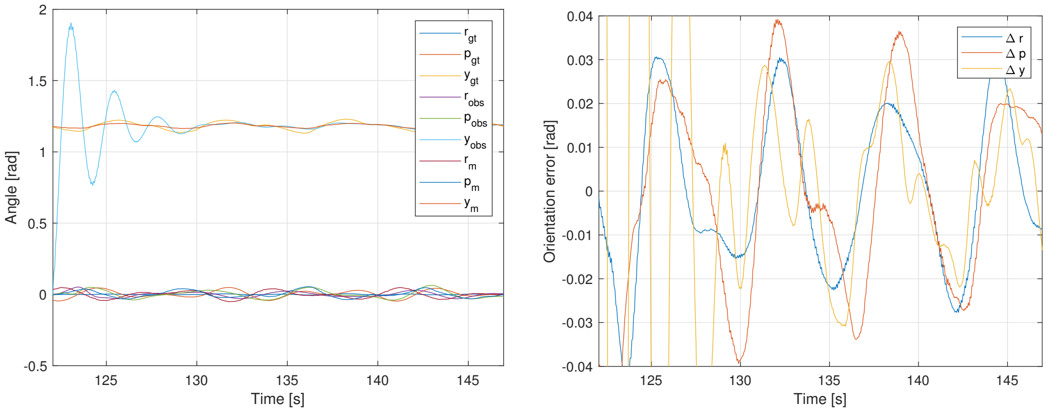

(c) Orientation tracking (d) Orientation error

Figure 5.10: In this instance, the observer converges closer to the measurements. Even though the error between the measurements and the observer decrease over time, there is still an error between the observer and the ground truth. The observer gains in this instance were $p_1 = 100$, $p_2 = 0.01$.

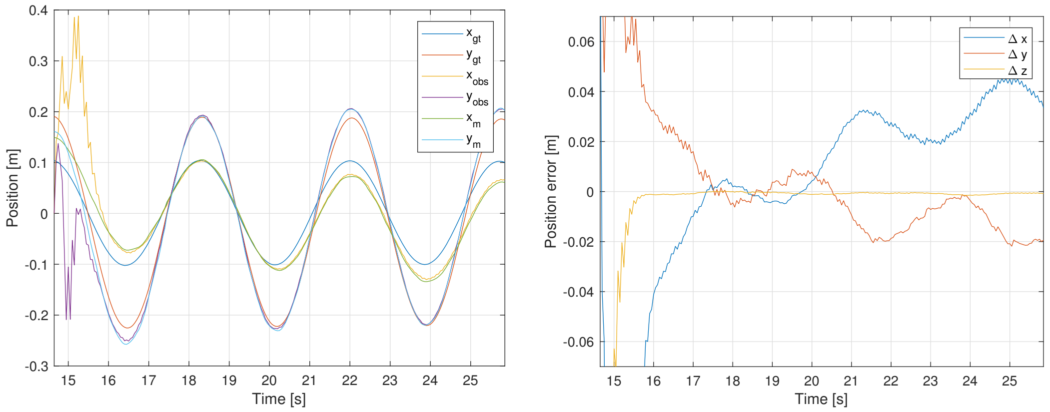

(a) Position tracking

(b) Position error

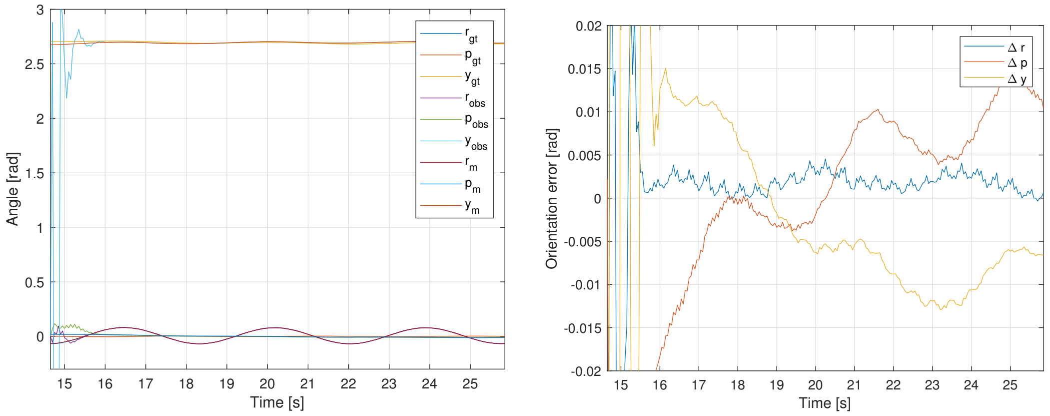

(c) Orientation tracking

(d) Orientation error

Figure 5.11: The IMU's measurements for the passive swings experiments is comparatively accurate. The observer could be tuned aggressively to $p_1 = 1000$, $p_2 = 0.005$ to aid convergence to the measurements, which also lead to a remaining error with respect to the ground truth of less than 5 cm in position.

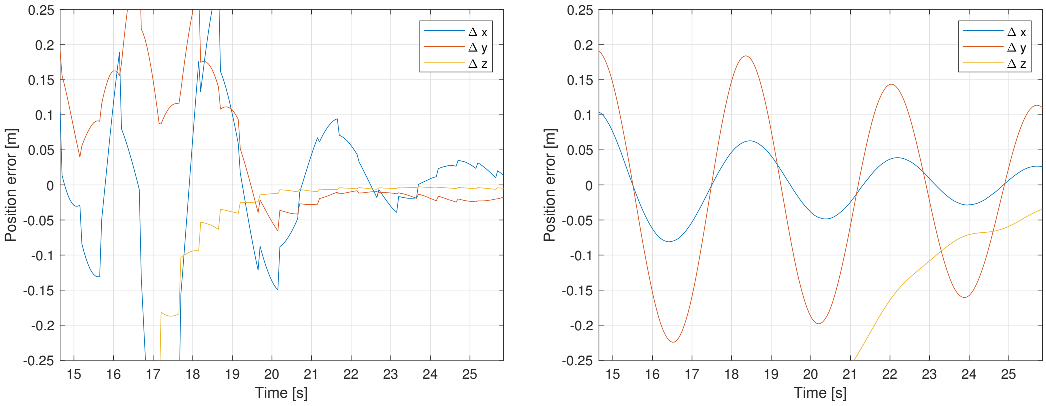

(a) Position error: Using IMU (b) Position error: Using camera

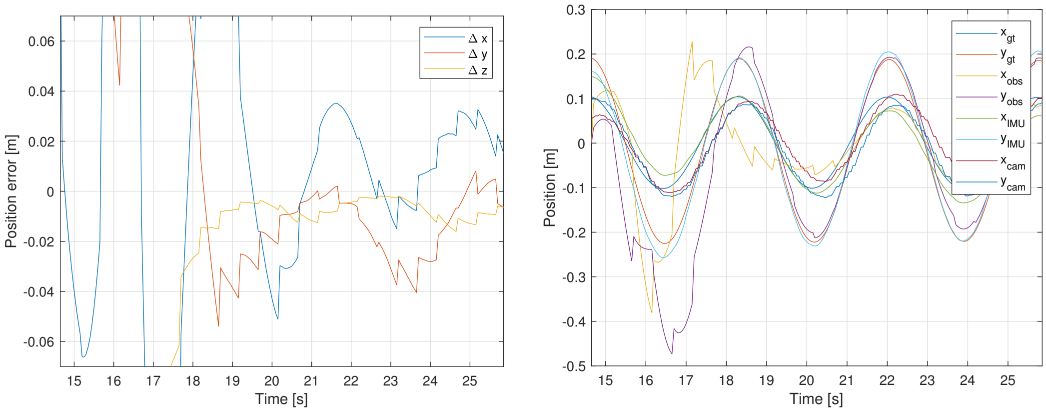

(c) Position error: Using both (d) Position tracking: Using both

Figure 5.12: The observer running on either only IMU or only on camera data does not converge as quickly as both combined. The observer gains for the camera input were $p_1 = 20$ and $p_2 = 5$, whereas the gains for the (more reliable) IMU input were $p_1 = 500$ and $p_2 = 0.01$.

Chapter 6

Conclusion

6.1 Main findings

This thesis presented an optimization-based approach to identify the dynamic and kinematic parameters of the SAM. Values for the mass, cable length, and spring stiffness and damping gain, both rotational and translational, have been obtained. Moreover, it could be shown that the rigid pendulum is an adequate model to represent SAM by recreating previously recorded trajectories.

An approach to model general multi-body systems obeying Pfaffian constraints has been described. It has been compared to multiple other methods of modeling those systems, and the equivalence of all approaches has been shown.

For Pfaffian constraint-based representation, two observer designs have been developed which are capable of estimating the full state of the system based on very low frequency measurements. The system equations for multiple different robots have been obtained based on their constraints using the described approach, and the observer has been shown to provide valid estimates for all of these instances. In addition to that, the observer has been applied to experimentally generated data to further validate it.

Furthermore, a position controller to be used with the framework has been proposed. A lower bound for its constant damping gain has been explained to define its region of stability. Again, the controller has been applied in combination with the observer on different simulated robots, and its performance was presented. In particular with regards to the SAM, the proposed controller might enable a variety of new maneuvers involving active propulsion away from the natural equilibrium. Examples of this include increasing the reachable workspace, but also swing-up maneuvers to reach poses that could not be constantly maintained by the propulsion system.

6.2 Future work

Regarding the system identification, experiments that are more specifically engineered to emphasize the inertia parameters or generally different approaches could provide results complementing those found in this work, to overall improve the observer's performance.

While the observer approach based solely on pose measurements showed promising results in simulations and experiments, no analytical proof could be provided to support its convergence. It would be desirable to find a formal proof to justify its application to a wider range of systems.

The proposed controller only covers *position* control, but it would be desirable to also apply it for nonconstant target trajectories. This could widely improve its applicability and performance.

Furthermore, the presented observers have been designed to work with multi-body systems in general, but they have only been applied to one single-body system in reality. In the future, the simulation results for multi-body systems could be validated with experiments on different real systems. Additionally, experiments showing the performance of the presented controller in combination with the observer could validate its applicability and performance.

Appendix

Invariance of the cross product to rotations

Rotations are length and angle preserving. The cross product returns a vector which is perpendicular to the two operand vectors with its length equaling the area of the parallelogram spanned by them. If the operand vectors are expressed in a particular frame, the result will be represented in that same frame.

We propose

$$R(a \times b) = (Ra \times Rb). \tag{1}$$

On the right-hand side (rhs) of (1), the cross product is taken first and then its result is rotated. On the left-hand side (lhs), the operand vectors are both rotated into a specific frame prior to taking the cross product, and the resulting vector will be expressed in that same frame.

We can interpret the rhs as the cross product of a and b, as if they were observed from a frame rotated by R^{T}. If we rotate the frame of observance only after taking the cross product, as on the lhs, we still end up with the same final result.

We can reorder (1) to $Ra_\times b = (Ra)_\times Rb$. Since it holds for any b, we can conclude

$$Ra_\times R^{\mathrm{T}} = (Ra)_\times. \tag{2}$$

The trace of the square the symmetric part of an inertia matrix times a differential adjoint

For an inertia matrix $\Lambda = \mathrm{blkdiag}(\Theta, mI)$ as defined in (1.49) and a twist V, we have

$$Q = \frac{1}{2}(\Lambda \mathrm{ad}_V + \mathrm{ad}_V^{\mathrm{T}} \Lambda) = \frac{1}{2} \begin{bmatrix} \Theta\omega_\times - \omega_\times\Theta & -mv_\times \\ mv_\times & 0 \end{bmatrix} \tag{3a}$$

$$\begin{aligned} \mathrm{trace}(QQ) &= \frac{1}{4}\mathrm{trace}\left(\begin{bmatrix} (\Theta\omega_\times - \omega_\times\Theta)^2 - m^2 v_\times^2 & -m(\Theta\omega_\times - \omega_\times\Theta)v_\times \\ mv_\times(\Theta\omega_\times - \omega_\times\Theta) & -m^2 v_\times^2 \end{bmatrix} \right) \\ &= \frac{1}{4}\mathrm{trace}\left((\Theta\omega_\times - \omega_\times\Theta)^2 - m^2 v_\times^2 \right) + \mathrm{trace}\left(-m^2 v_\times^2 \right) \\ &= \frac{1}{4}\mathrm{trace}\left((\Theta\omega_\times - \omega_\times\Theta)^2 \right) - \frac{1}{2}\mathrm{trace}\left(m^2 v_\times^2 \right) \\ &= \omega^{\mathrm{T}} f(\Theta)\omega + m^2 v^{\mathrm{T}} v = V^{\mathrm{T}} F(\Lambda) V, \end{aligned} \tag{3b}$$

where

$$f_{11}(\Theta) = 8\Theta_{23}^2 + 2((\Theta_{22} - \Theta_{33})^2 + \Theta_{12}^2 + \Theta_{13}^2) \tag{4a}$$

$$f_{22}(\Theta) = 8\Theta_{13}^2 + 2((\Theta_{11} - \Theta_{33})^2 + \Theta_{12}^2 + \Theta_{23}^2) \tag{4b}$$

$$f_{33}(\Theta) = 8\Theta_{12}^2 + 2((\Theta_{11} - \Theta_{22})^2 + \Theta_{23}^2 + \Theta_{13}^2) \tag{4c}$$

$$f_{12}(\Theta) = -6\Theta_{23}\Theta_{13} - 2(\Theta_{22} - \Theta_{33})\Theta_{12} - 2(\Theta_{11} - \Theta_{33})\Theta_{12} \tag{4d}$$

$$f_{13}(\Theta) = -6\Theta_{23}\Theta_{12} + 2(\Theta_{22} - \Theta_{33})\Theta_{13} - 2(\Theta_{11} - \Theta_{22})\Theta_{13} \tag{4e}$$

$$f_{23}(\Theta) = -6\Theta_{13}\Theta_{12} + 2(\Theta_{11} - \Theta_{33})\Theta_{23} + 2(\Theta_{11} - \Theta_{22})\Theta_{23} \tag{4f}$$

$$f(\Theta) = \frac{1}{4}\begin{bmatrix} f_{11}(\Theta) & f_{12}(\Theta) & f_{13}(\Theta) \\ f_{12}(\Theta) & f_{22}(\Theta) & f_{23}(\Theta) \\ f_{13}(\Theta) & f_{23}(\Theta) & f_{33}(\Theta) \end{bmatrix} \tag{4g}$$

$$F(\Lambda) = \begin{bmatrix} f(\Theta) & 0 \\ 0 & m^2 I \end{bmatrix}, \tag{4h}$$

where the bottom right indices denote rows and columns of an element of a matrix.

List of Algorithms

List of Figures

List of Tables

References

[1] David H. Ackley. *A Connectionist Machine for Genetic Hillclimbing.* Springer US, 1987. doi: 10.1007/978-1-4613-1997-9.

[2] F. Bullo and R. M. Murray. Proportional derivative (pd) control on the euclidean group. Technical report, California Institute of Technology, August 1995. URL `https://authors.library.caltech.edu/28018/1/95-010.pdf`.

[3] F. Bullo and R. M. Murray. Proportional derivative (pd) control on the euclidean group. In *In European Control Conference*, pages 1091–1097, 1995.

[4] Andre Coelho, Yuri Sarkisov, Xuwei Wu, Hrishik Mishra, Harsimran Singh, Alexander Dietrich, Antonio Franchi, Konstantin Kondak, and Christian Ott. Whole-body teleoperation and shared control of redundant robots with applications to aerial manipulation. *Journal of Intelligent & Robotic Systems*, 102(1), apr 2021. doi: 10.1007/s10846-021-01365-7.

[5] Chiara Gabellieri, Yuri S Sarkisov, Andre Coelho, Lucia Pallottino, Konstantin Kondak, and Min Jun Kim. Compliance control of a cable-suspended aerial manipulator using hierarchical control framework. In *2020 IEEE/RSJ International Conference on Intelligent Robots and Systems (IROS)*, pages 7196–7202. IEEE, oct 2020. ISBN 978-1-7281-6213-3. doi: 10.1109/IROS45743.2020.9340703.

[6] G. Heredia, A.E. Jimenez-Cano, I. Sanchez, D. Llorente, V. Vega, J. Braga, J.A. Acosta, and A. Ollero. Control of a multirotor outdoor aerial manipulator. In *2014 IEEE/RSJ International Conference on Intelligent Robots and Systems.* IEEE, sep 2014. doi: 10.1109/iros.2014.6943038.

[7] Felix Huber, Konstantin Kondak, Kai Krieger, Dominik Sommer, Marc Schwarzbach, Maximilian Laiacker, Ingo Kossyk, Sven Parusel, Sami Haddadin, and Alin Albu-Schäffer. First analysis and experiments in aerial manipulation using fully actuated redundant robot arm. In *2013 IEEE/RSJ International Conference on Intelligent Robots and Systems*, pages 3452–3457. IEEE, nov 2013. ISBN 978-1-4673-6357-0. doi: 10.1109/IROS.2013.6696848.

[8] Min Jun Kim, Konstantin Kondak, and Christian Ott. A stabilizing controller for regulation of uav with manipulator. *IEEE Robotics and Automation Letters*, 3(3): 1719–1726, jul 2018. ISSN 2377-3774. doi: 10.1109/LRA.2018.2803205.

[9] Diederik P. Kingma and Jimmy Lei Ba. Adam: A method for stochastic optimization. In *3rd International Conference for Learning Representations (ICLR)*, 2015.

[10] Christopher Korpela, Matko Orsag, and Paul Oh. Towards valve turning using a dual-arm aerial manipulator. In *2014 IEEE/RSJ International Conference on Intelligent Robots and Systems*. IEEE, sep 2014. doi: 10.1109/iros.2014.6943037.

[11] Jongseok Lee, Ribin Balachandran, Yuri S. Sarkisov, Marco De Stefano, Andre Coelho, Kashmira Shinde, Min Jun Kim, Rudolph Triebel, and Konstantin Kondak. Visual-inertial telepresence for aerial manipulation. In *2020 IEEE International Conference on Robotics and Automation (ICRA)*, pages 1222–1229. IEEE, may 2020. ISBN 978-1-7281-7396-2. doi: 10.1109/ICRA40945.2020.9197394.

[12] Pierre Merriaux, Yohan Dupuis, Rémi Boutteau, Pascal Vasseur, and Xavier Savatier. A study of vicon system positioning performance. *Sensors*, 17(7):1591, jul 2017. doi: 10.3390/s17071591.

[13] Hrishik Mishra, Marco De Stefano, Alessandro Massimo Giordano, and Christian Ott. A nonlinear observer for free-floating target motion using only pose measurements. In *2019 American Control Conference (ACC)*, pages 1114–1121. IEEE, jul 2019. ISBN 978-1-5386-7901-2. doi: 10.23919/ACC.2019.8814815.

[14] Yuri S. Sarkisov, Min Jun Kim, Davide Bicego, Dzmitry Tsetserukou, Christian Ott, Antonio Franchi, and Konstantin Kondak. Development of sam: cable-suspended aerial manipulator. In *2019 International Conference on Robotics and Automation (ICRA)*, pages 5323–5329. IEEE, may 2019. ISBN 978-1-5386-8176-3. doi: 10.1109/ICRA.2019.8793592.

[15] Yuri S. Sarkisov, Min Jun Kim, Andre Coelho, Dzmitry Tsetserukou, Christian Ott, and Konstantin Kondak. Optimal oscillation damping control of cable-suspended aerial manipulator with a single imu sensor. In *2020 IEEE International Conference on Robotics and Automation (ICRA)*, pages 5349–5355. IEEE, may 2020. ISBN 978-1-7281-7396-2. doi: 10.1109/ICRA40945.2020.9197055.

[16] J. M. Selig. Lie groups and lie algebras in robotics. In Jim Byrnes, editor, *Computational Noncommutative Algebra and Applications*, pages 101–125, Dordrecht, 2004. Springer Netherlands. ISBN 978-1-4020-2307-1.

[17] Alejandro Suarez, Antonio Enrique Jimenez-Cano, Victor Manuel Vega, Guillermo Heredia, Angel Rodriguez-Castaño, and Anibal Ollero. Design of a lightweight dual arm system for aerial manipulation. *Mechatronics*, 50:30–44, apr 2018. doi: 10.1016/j.mechatronics.2018.01.005.

[18] Wenyu Sun and Ya-Xiang Yuan. *Optimization theory and methods: nonlinear programming*, volume 1. Springer Science & Business Media, 2006.

[19] Arda Yigit, Miguel Arpa Perozo, Loic Cuvillon, Sylvain Durand, and Jacques Gangloff. Novel omnidirectional aerial manipulator with elastic suspension: Dynamic control and experimental performance assessment. *IEEE Robotics and Automation Letters*, 6(2):612–619, apr 2021. doi: 10.1109/lra.2020.3048880.

[20] Shiyu Zhao. Time derivative of rotation matrices: A tutorial. Technical report, University of Sheffield, UK, 2016. URL `arXiv:1609.06088`.